SON-dependent nuclear speckle rejuvenation alleviates proteinopathies.

William Dion[1, #], Yuren Tao[2, #], Maci Chambers[1], Shanshan Zhao[2], Riley K. Arbuckle[3,4], Michelle Sun[1], Syeda Kubra[1], Imran Jamal [1], Yuhang Nie[2], Megan Ye[1], Mads B. Larsen[1], Daniel Camarco[1], Eleanor Ickes[1], Claire DuPont[1], Haokun Wang[1], Bingjie Wang[3], Silvia Liu[5,6], Shaohua Pi[3], Bill B Chen[1,7], Yuanyuan Chen [3,8] *, Xu Chen[2] *, and Bokai Zhu[1,5,9] *

[1] Aging Institute of UPMC, University of Pittsburgh School of Medicine, Pittsburgh, PA, U.S.A.

[2] Department of Neuroscience, School of Medicine, University of California, San Diego, CA, U.S.A.

[3] Department of Ophthalmology, University of Pittsburgh School of Medicine, PA, U.S.A.

[4] Department of Human Genetics, University of Pittsburgh Graduate School of Public Health, Pittsburgh, PA, USA.

[5] Pittsburgh Liver Research Center, University of Pittsburgh, Pittsburgh, PA, U.S.A.

[6] Department of Pathology, University of Pittsburgh School of Medicine, Pittsburgh, PA, U.S.A.

[7] Division of Pulmonary, Allergy and Critical Care Medicine, Department of Medicine, University of Pittsburgh School of Medicine, Pittsburgh, PA, U.S.A.

[8] Department of Pharmacology and Chemical Biology, University of Pittsburgh School of Medicine, PA, U.S.A.

[9] Division of Endocrinology and Metabolism, Department of Medicine, University of Pittsburgh School of Medicine, Pittsburgh, PA, U.S.A.

# These authors contribute equally.

Corresponding authors*:

Yuanyuan Chen: cheny1@pitt.edu

Xu Chen: x1chen@health.ucsd.edu

Bokai Zhu: bzhu@pitt.edu

Abstract

Current treatments targeting individual protein quality control have limited efficacy in alleviating proteinopathies, highlighting the prerequisite for a common upstream druggable target capable of global proteostasis modulation. Building on our prior research establishing nuclear speckles as a pivotal membrane-less organelle responsible for global proteostasis transcriptional control, we aim to alleviate proteinopathies through nuclear speckle rejuvenation. We identified pyrvinium pamoate as a small-molecule nuclear speckle rejuvenator that enhances protein quality control while suppressing YAP1 signaling via decreasing the surface/interfacial tension of nuclear speckle condensates through interaction with the intrinsically disordered region of nuclear speckle scaffold protein SON. In pre-clinical models, nanomolar pyrvinium pamoate alleviated retina degeneration and reduced tauopathy by promoting autophagy and ubiquitin-proteasome system in a SON-dependent manner without causing cellular stress. Aberrant nuclear speckle morphology, reduced protein quality control and increased YAP1 activity were also observed in human tauopathies. Our study uncovers novel therapeutic targets for tackling protein misfolding disorders within an expanded proteostasis framework encompassing nuclear speckles and YAP1.

Introduction:

Proteinopathies are diseases associated with the accumulation of misfolded proteins, which often arise from a decline in proteostasis pathways, including the ubiquitin-proteasome system (UPS), the ER-Golgi protein secretory pathways, and autophagy lysosomal pathway (ALP) [1, 2]. However, therapies targeting singular pathways have limited efficacy, indicating an incomplete understanding of disease mechanisms.

We recently discovered that under physiological conditions, the network of proteostasis pathways manifests as cell-autonomous 12-hour (12h) ultradian rhythms, regulated by a dedicated 12h oscillator, independent from the 24h circadian clock and the cell cycle [3, 4, 5, 6, 7, 8, 9, 10, 11, 12, 13]. By studying this 12h oscillator, we uncovered an unexpected role of nuclear speckles in global proteostasis control [9]. Nuclear speckles are membrane-less organelles important for mRNA processing and gene regulation[14, 15, 16, 17, 18], and their liquid-liquid phase separation (LLPS) dynamics dictate the global transcriptional capacity of proteostasis genes [9]. Moderate overexpression of the nuclear speckle scaffolding protein SON is sufficient to decrease nuclear speckle sphericity, increase the recruitment of nuclear speckles to chromatin, amplify proteostasis gene expression, and reduce protein aggregation [9]. Conversely, reducing SON level leads to much more spherical and stagnant speckles, sequesters nuclear speckles away from chromatin, blunts proteostasis gene expression and subsequently elevates intracellular protein aggregates [19]. More importantly, SON expression decreases with age in various tissues in mice, concomitant with more spherical and smaller nuclear speckles (**Supplementary Fig. 1a-f**). In addition, reduced SON expression was also observed in aging human lungs, and in brain tissues of human subjects with Alzheimer's disease (**Supplementary Fig. 1g-i**) [9, 20]. Based upon these results, we herein propose that enhancing SON expression or function, either genetically or pharmacologically, under aging and disease conditions, could potentially restore nuclear speckle morphology and function. This, in turn, would bolster the entire protein quality control system, thereby delaying or even reversing the progression of both aging-related and inherited proteinopathies. We introduce this concept as SON-dependent ‘nuclear speckle rejuvenation’ (**Fig. 1a**).

In this study, we initially characterized the comprehensive transcriptome changes resulting from SON-mediated nuclear speckle rejuvenation and unexpectedly discovered a broader proteostasis framework that incorporates SON-mediated nuclear speckles condensation, unfolded protein response (UPR) transcription factors (TF)-mediated proteostasis gene activation and repression of YAP1 transcriptional activity. Via a high-throughput drug screen, we identified pyrvinium pamoate (PP) as a small molecule nuclear speckle rejuvenator that recapitulates the entire transcriptome changes elicited by SON overexpression. Mechanistically, via a cell-free nuclear speckle reconstitution system, we demonstrated that PP exerts transcriptional reprogramming via reducing the surface/interfacial tension of nuclear speckle condensates and promoting their wetting of genomic DNA via targeting the intrinsically disordered region (IDR) of SON. In preclinical models, PP exhibited strong efficacy in protecting against both tauopathy and retinal degeneration at nanomolar concentration without inducing cellular stress. Lastly, we showed that both the reduction of protein quality control gene expression and increase of YAP1 transcriptional activity is associated with retinal degeneration in mice and tauopathy in humans.

Result:

Genetic rejuvenation of nuclear speckles transcriptionally reprograms global proteostasis and YAP1 activity in an opposing manner.

To determine the extent by which SON transcriptionally reprograms gene expression under both basal and proteotoxic stress conditions, we performed bulk mRNA-Seq on immortalized mouse embryonic fibroblasts (MEFs) with either SON knockdown (KD) by siRNA or overexpression (OE) via CRISPRa[21], in the absence or presence of the ER stress inducer tunicamycin (Tu) as previously described (**Supplementary Table1**) [9]. Principal component analysis (PCA) on total mRNA level indicated that while SON manipulation has little effects on global gene expression under basal condition, SON OE and KD significantly amplified and dampened the global transcriptional response to ER stress, respectively (**Fig. 1b**). These include 461 genes that are normally induced, and 901 genes repressed by Tu under normal SON expression condition (**Fig. 1c-e, Supplementary Fig. 2a**). For both groups of genes, we further observed a strong correlation between the relative fold induction or repression for each gene under SON OE and KD conditions (**Supplementary Fig. 2b**), further demonstrating the robustness of bidirectional control on proteostasis gene expression by SON.

As expected, gene ontology (GO) analysis revealed that those ER stress-induced 461 genes are strongly enriched in protein quality control pathways, including protein folding (such as *Pdia3*, *Dnajb11* and *Manf*), ER/Golgi quality control (such as *Sec23b*, *Hyou1* and *Hspa5*), tRNA aminoacylation (such as *Gars*, *Iars* and *Eprs*), ER-associated protein degradation (ERAD) (such as *Edem1*, *Syvn1*, *Sel1l* and *Ube2g2*), and autophagy (such as *Sqstm1* and *Atg13*) (**Fig. 1f, Supplementary Fig. 2a**). To shed light on the mechanisms by which SON transcriptionally amplifies gene activation in response to ER stress, we performed both Landscape In Silico deletion Analysis (LISA) [22] and motif analysis to infer the transcriptional regulators that may mediate nuclear speckles interactions with chromatin. Both analyses revealed basic leucine zipper (bZIP) transcription factors (TFs), including ATF6, XBP1, ATF4 and CREB1 as the top candidates (**Fig. 1g and Supplementary Fig. 2c**). ChIP-qPCR further showed increased recruitment of nuclear speckles to the 3' regions of selective proteostasis genes in response to SON OE under both basal and ER stress conditions, concomitant with increased recruitment of XBP1s to the promoter regions of the same genes (**Supplementary Fig. 2d, e**). To corroborate our *in vitro* findings, we further examined a recently published murine *in vivo* hepatic XBP1s interactome dataset [10], and found proteins involved in mRNA splicing and processing are very strongly enriched in the XBP1s interactome at CT8, a time when hepatic SON expression peaks [9], with PRPF8, SNRNP200 and DHX9 being the top three most abundant proteins detected in the entire XBP1s interactome at CT8 (**Fig. 1h, i**). By contrast, at CT0 when SON expression is the lowest, the amount of splicing proteins that interact with XBP1s is markedly reduced (**Fig. 1i**). The observed decreased recruitment of splicing proteins to XBP1s at CT0 is not due to reduced XBP1s level itself, as the hepatic XBP1s expression at CT0 is in fact higher compared to CT8 [3, 23]. These results thus reinforce the notion that nuclear speckles rejuvenation by SON OE is sufficient to amplify the global proteostasis transcriptional activation, likely via facilitating physical interactions between nuclear speckles and UPR TF like XBP1s.

Compared to induced genes, much less is known about the gene programs that are repressed under ER stress. GO analysis indicate that those 901 ER stress-repressed genes are strongly enriched in Hippo-YAP1 signaling that regulates the diverse biological processes of angiogenesis, axon guidance, epithelial to mesenchymal transition (EMT), wound healing, cell adhesion, cell migration, and extra cellular matrix organization, with examples of canonical YAP1 target genes *Bmp4*, *Tuba1a*, *Fzd2*, *Tgfb3* and *Yap1* itself and its transcriptional partner *Tead2* [24, 25, 26] (**Fig. 1c-f and Supplementary Fig. 2a**). YAP1 and TEAD2 were further predicted to be transcriptional regulators of these 901 ER stress-repressed genes via both LISA and motif analysis (**Fig. 1j and Supplementary Fig. 2c**) and the nuclear YAP1 level was significantly reduced in response to either Tu or SON OE and further decreased upon the combination of the two (**Fig. 1k, l**). We further performed TEAD luciferase reporter assay and found that both SON OE and Tu significantly reduced the TEAD response element-driven luciferase activity in MEFs, with the lowest observed in SON OE cells under ER stress (**Supplementary Fig. 3a**). Scratch assays further confirmed that both SON OE and Tu significantly reduced cell migration in MEFs, with the lowest observed in SON OE cells under ER stress (**Fig. 1m, n**). To rule out the possibility that the global repression of YAP1 transcriptional output during ER stress is specific to MEFs or Tu, we further analyzed a recent transcriptome dataset in the human astrocytoma-derived LN-308 cell line in response to both Tu and thapsigargin (Thap) (another ER stress inducer) treatments [27], and observed a strong downregulation of genes involved in YAP1 signaling under both treatments that progressed with time (**Supplementary Fig. 3b-d**). Together, our data indicates that the downregulation of YAP1 transcriptional output is an integral component of the global transcriptional response to proteotoxic stress, and it is also under nuclear speckles control.

Given the established roles of nuclear speckles in mRNA processing [28, 29, 30], we next investigated whether SON also regulates mRNA splicing dynamics. While SON manipulation has no effects on the overall transcriptional state of mature mRNA under basal DMSO condition (**Supplementary Fig. 4a bottom**) (consistent with total mRNA shown in **Fig. 1a**), it exerted profound effects on the pre-mRNA level (**Supplementary Fig. 4a top**), indicating a change in splicing dynamics. By either estimating the relative splicing rates among different groups under basal condition using a simple first-order kinetic model of transcription (see Materials and Methods) or quantifying global intron retention events using the iRead algorithm [31], we found that SON increases the splicing rates and improves the splicing fidelity of genes involved in proteostasis and RNA metabolism, and negatively regulates those involved in YAP1-related processes of cell migration, axon guidance, cell adhesion and EMT (**Supplementary Figs. 4b-e, 5a-d and 6a-d**). The significant enrichment in mRNA processing genes themselves under SON control is consistent with known potent autoregulation of splicing factors [32, 33]. Furthermore, we also found that SON can activate and repress the mature mRNA expression of a select set of proteostasis (albeit very modestly) and YAP1 target genes, respectively, under basal DMSO conditions (**Supplementary Fig. 7a-c**). Finally, we observed that SON can also activate an anti-viral response gene signature under basal DMSO condition (**Supplementary Fig. 7b**), suggesting a potential broader implication of nuclear speckle rejuvenation in boosting innate immunity. Collectively, our results demonstrated that genetically rejuvenating nuclear speckles reprograms global proteostasis and YAP1 transcriptional output in an opposing manner, under both basal and proteotoxic stress conditions.

Our results thus far demonstrated a tripartite network where nuclear speckle rejuvenation by SON boosts proteostasis and suppresses YAP1. Two possible topologies of the network exist. In model one, nuclear speckles can signal both proteostasis and YAP1 signaling directly (**Supplementary Fig. 8a, model 1**), while in model 2, nuclear speckles repress YAP1 downstream of increased proteostasis gene program (**Supplementary Fig. 8a, model 2**). To distinguish between the two models, we examined a recently published RNA-seq dataset in HEK293T cells treated with DMSO, Thap or a very specific XBP1s small molecule activator IXA4 [34, 35, 36]. While IXA4 can induce a robust proteostasis gene signature similar to that of Thap, it failed to repress YAP1 transcriptional output genes as Thap did (**Supplementary Fig. 8b-d**). Collectively these results support the first model where nuclear speckles can program proteostasis gene expression and YAP1 transcriptional output in parallel, likely via promoting physical interaction between nuclear speckles and XBP1s for the former, and triggering YAP1 nuclear exclusion for the latter (**Supplementary Fig. 8e**). We speculate the opposing changes in proteostasis and YAP1 signaling may reflect an energetic trade-off between proteostasis and the control of cell dynamics under proteotoxic stress (**Supplementary Fig. 8f**).

High-throughput screen (HTS) identified pyrvinium pamoate (PP) as a small-molecule rejuvenator of the nuclear speckle.

Having established the proof-of-principle of nuclear rejuvenation via SON OE, we next explore the feasibility of rejuvenating nuclear speckles pharmacologically, for two reasons. First, compared to the challenging implementation of SON-based gene therapy, which faces obstacles due to the considerable size (~7kb) of SON's open reading frame, using small molecules to boost nuclear speckle activity may offer superior therapeutic potential. Secondly, we wanted to utilize an orthogonal approach to further demonstrate the opposing transcriptional changes of proteostasis and YAP1 signaling following nuclear speckle rejuvenation. Since SON OE and KD reduced and increased the sphericity of nuclear speckles [19], respectively, putative nuclear speckle rejuvenators are expected to reduce the sphericity (and increase the diffuseness or irregularity) of speckles.

We started with a library of over 2500 FDA-approved drugs and ran a primary HTS on our previously described EGFP::SC35 (SRSF2) MEFs (EGFP was knocked in to the N-terminus of endogenous *Srsf2* locus, which is a well-established marker for nuclear speckles [9]) to identify compounds that could alter nuclear speckles sphericity (**Fig. 2a**). As a quality control, our primary screen successfully identified four histone deacetylase inhibitors that produced much more spherical nuclear speckles approaching and/or exceeding r=0.9 (**Supplementary Fig. 9a, b**), in alignment with a previous study [37]. In the end, we identified five compounds - the tyrosine kinase inhibitors nintedanib (NB) and ponatinib (PB), the anti-microbial proflavine hemisulfate (PH) and proflavine, and the anthelmintic pyrvinium pamoate (PP) – having the ability to both decrease nuclear speckles sphericity and amplify *Perk*-promoter driven dGFP expression (*Perk* is a UPR target and exhibits 12h rhythms of expression [3]) in a dose-dependent manner (**Fig. 2b, and**

Supplementary Fig. 9c-e). For PP, a clear dose response in reducing the nuclear speckle sphericity was observed between 0 and 0.3μM, and further increasing its concentration failed to further decrease the sphericity (**Fig. 2b and Supplementary Fig. 9c**). PP also increased the perimeter of nuclear speckles (**Fig. 2c**), indicating that PP can increase the surface area of nuclear speckles in the three-dimensional space of the nucleus.

To determine which of these drugs are *bona fide* nuclear rejuvenators, we performed mRNA-Seq on MEFs treated with NB, PB, PH or PP for 24 hours and compared the transcriptome signature of each drug (**Supplementary Fig. 10a,** and **Supplementary Table2**) with those of SON OE and KD under both DMSO and Tu conditions. Gene set enrichment analysis (GSEA) [38] using either those 461 Tu-induced or 901 Tu-repressed genes (depicted in **Fig. 1e**) revealed PP as the only drug triggering a transcriptional response with strong resemblance to SON OE cells in response to ER stress (**Fig. 2d, e and Supplementary Fig. 10b**). These included both upregulated genes implicated in protein quality control and downregulated genes involved in the regulation of cell dynamics (**Fig. 2f, g and Supplementary Fig. 10c, d**). LISA analysis on differentially expressed genes by PP revealed bZIP TFs ATF4 and YAP1 among top transcriptional regulators of upregulated and downregulated genes, respectively (**Supplementary Fig. 10e**). 1μm PP increased the expression of UPR and integrated stress response (ISR) TFs – XBP1s and ATF4 - at both the mRNA and protein level (**Supplementary Fig. 10f, g)** and induced nuclear exclusion of YAP1 (**Supplementary Fig. 10h)**, while not affecting SON level (**Supplementary Fig. 10i**).

Our analysis so far suggested the PP induced a transcriptional signature that resembles a mixture of responding to SON OE and Tu treatment. We performed additional comparative transcriptome analysis to further validate this conclusion. First, when comparing the fold induction or repression of gene expression by PP and Tu, the signature of PP is more similar to that of Tu under SON OE compared to under SON KD condition ($p = 0.00195$ by Chow tests) (**Supplementary Fig. 11a**). Secondly, similar to SON OE (**Supplementary Fig. 7b**), PP also induced expression of genes involved in anti-viral response (**Supplementary Fig. 11b-f**), distinct from those induced under ER stress. Thirdly, GSEA indicated a strong resemblance of gene signatures repressed by PP and SON OE that are enriched in the control of cell dynamics, under basal conditions in the absence of ER stress (**Supplementary Fig. 12a-e**). Lastly, like SON (**Supplementary Figs. 5d and 6d**), PP also improves the splicing fidelity of splicing genes themselves (**Supplementary Fig 13a-f**), again reflecting autoregulation of splicing factors. Taken together, these results indicate that PP is a bona fide nuclear speckle rejuvenator that at 1μM induces a transcriptional signature in MEFs highly similar to that of SON OE cells under both basal and proteotoxic stress conditions.

PP reduces the surface tension of nuclear speckle condensates via targeting SON IDR.

To confirm that PP rejuvenates nuclear speckles in a SON-dependent manner, we knocked down *Son* via siRNA in MEFs. Son knockdown leads to smaller and more spherical speckles, consistent with our previous study [19] (**Fig. 2h**). Importantly, PP's ability to reduce nuclear speckle sphericity is abolished in *Son* knockdown MEFs (**Fig. 2h).** Subsequently, *Son* knockdown impaired PP's ability to both activate protein quality control gene expression and repress YAP1 transcriptional output (**Fig. 2i**). To determine whether PP can physically interact with SON in MEFs, we performed cellular thermal shift assay (CETSA), which is based on ligand-induced thermal stabilization of target proteins, whereas unbound proteins denature, aggregate and precipitate at elevated temperatures, ligand-bound proteins remain soluble due to increased stability [39, 40]. Using a SON-specific antibody (**Supplementary Fig. 14a**), we found that PP induced a thermal shift of SON with a direction consistent with stabilization (**Fig. 3a**). As negative controls, we found that PP does not stabilize SRSF2 (SC35), another nuclear speckle protein, or the ISR/UPR TF ATF4, whose expression is nonetheless significantly increased by PP (**Fig. 3b and Supplementary Fig. 14b**).

SON is the central scaffold protein of nuclear speckles [41, 42, 43], and its ~12h rhythmic concentration fluctuation drives ~12h rhythmic nuclear speckles LLPS dynamics and chromatin binding alternating between either a diffuse and chromatin-associated state or a punctate and chromatin-dissociated state [9]. By contrast, SRSF2(SC35) is one of the critical subunits of the spliceosomes, which have a broader spatial distribution also occupying the periphery of nuclear speckles, particularly at the interface between nuclear speckles and the nucleoplasm or chromatin and is not essential for speckle formation [44, 45]. In MEFs, PP generated a more diffuse and irregular (less spherical) nuclear speckles with larger surface area (**Fig. 2b, c**), suggesting that PP could influence nuclear speckle condensates material properties, likely via reducing the surface tension of speckles (surface tension is the tendency of liquid droplets to minimize the total surface area, therefore an increased surface area is suggestive of reduced surface tension[46]). Given the CETSA data indicating PP can bind to SON directly, we next tested whether PP can directly impact the condensates formation of two nuclear speckle protein, SRSF2 and SON, using an *in vitro* droplet formation assay [47]. Using different computational algorithms to search for intrinsically disordered region (IDR) [48, 49, 50], we identified two IDRs at the N and C terminals of mouse SON, and long stretches of IDRs spanning two-thirds of mouse SRSF2 (**Fig. 3c and Supplementary Fig. 14c**). We separately cloned the regions encoding both SON IDRs and the full-length SRSF2 into the C-terminal of mCherry and purified recombinant proteins from *E. coli* (**Supplementary Fig. 14d**). Purified recombinant proteins were added to buffers containing 10% crowding reagents PEG-8000 as previously described [47]. Confocal fluorescence microscopy of the different protein solutions revealed mCherry positive, micron-sized spherical droplets freely moving in solution and wetting the surface of the glass coverslip (**Supplementary Movies 1-3**). All proteins droplets were highly spherical, exhibited fusion/coalescence behaviors (**Supplementary Movies 1-3**), and scaled in size and number positively with increasing concentration of proteins and negatively with increasing salt concentration (**Supplementary Fig. 14e, f**), all properties expected for liquid-like droplets [47].

Due to surface tension, small droplets will eventually morph into a fewer number of large droplets, resulting in a net decrease of surface area, either via coalescence or Ostwald ripening [51] (**Fig. 3d**), which was seen for all protein droplets after 20 minutes of time lapse imaging (**Fig. 3e, f, and Supplementary Fig. 14g**). Addition of PP to SON IDR2, but not SON IDR1 and SRSF2 protein solutions, significantly reduced the kinetics of this process in a dose-dependent manner, resulting in a negligible decrease of relative surface area after 20 minutes (**Fig. 3d-f, and Supplementary Fig. 14g, h**). The significance of SON IDR2 is reinforced by the substantial evolutionary conservation of its sequences across seven distinct species spanning wide phylogenetic distances from zebra fish to humans (**Supplementary Fig. 14i**).

To better recapitulate the complex compositions of nuclear speckles in the cell-free system, we further supplemented recombinant mCherry-SON IDR2 with nuclear extract (NE) from Hela cells that include all active components of transcription and splicing factors (**Supplementary Fig. 15a**) [47]. Mass spectrometry confirmed that Hela NE-supplemented mCherry-SON IDR2 condensates preferentially compartmentalized splicing factors (including SRSF2), with twelve of the top fifteen enriched proteins previously identified in nuclear speckles [52, 53] (**Supplementary Fig. 15b, c**). By contrast, other nuclear proteins like proteasome subunits, DNA repair factors or general transcription factors were not enriched in the reconstituted condensates (**Supplementary Fig. 15b, c**). These condensates further exhibited less spherical morphology, had increased number and total size (**Supplementary Fig. 15d, e**), features expected from nuclear speckle-like condensates with heterogeneous viscoelastic properties [54]. Importantly, the addition of PP reduced both the sphericity and surface tension of Hela NE-supplemented SON IDR2 condensates in a dose-dependent manner (**Fig. 3g-i**), consistent with the observed effects of PP on nuclear speckle morphology in cells. Together, these data suggest that PP can reduce the surface tension to stabilize both homotypic and heterotypical NE-supplemented SON condensates in a cell-free system, via interacting with SON C-terminal IDR2.

To investigate whether PP may affect the relative spatial distribution of SON and SRSF2 within nuclear speckles, we further supplemented recombinant mCherry-SON IDR2 with NE from GFP::SRSF2-expressing MEFs (**Fig. 3j**). The resulting nuclear speckle-like condensates recapitulated the anticipated spatial distribution of SON and SRSF2 proteins, with the former located at the center, and the latter exhibiting a broader distribution with its highest concentration often observed at 350nm away from the SON IDR2 center (**Supplementary Fig. 15f and Supplementary Movie 4**). While PP does not alter the relative spatial distribution of SON IDR2 and SRSF2, it reduced their sphericity, and markedly increased SRSF2 content at the periphery of nuclear speckle-like condensates (**Fig. 3k-m**). To determine whether PP may also influence the wetting of genomic DNA by nuclear speckles [55], we further added mouse genomic DNA into the droplet solution. In accordance with observations in intact cells, nuclear speckle condensates largely don't mix with but can wet the DNA (**Supplementary Fig. 15g**). Interestingly, the addition of PP more than doubled the wetting of genomic DNA by the reconstituted nuclear speckles (**Fig. 3n, o**).

To validate that PP can alter the nuclear speckle LLPS properties *in vitro* in the context of intact cells, we further performed 1,6 hexanediol sensitivity assay [56] using the same EGFP::SRSF2 MEFs [9]. A short term 1,6 hexanediol treatment preferentially dissolves liquid but not solid condensates, thus a change in the sensitivity to 1,6 hexanediol reflects an alteration in the LLPS property of a given condensates [56]. As demonstrated in **Supplementary Fig. 16a, b**, PP desensitized SRSF2 to the increasing concentrations of 1,6 hexanediol. This effect was not observed on two other biomolecular condensates, the nuclear MED1 [47] and cytosolic GW182 present in P-bodies [57] (**Supplementary Fig. 16c, d**). Taken together, these results suggest a mechanism where PP can reduce the surface/interfacial tension of nuclear speckles via targeting SON IDR, leading to larger surface areas with increased SRSF2 content at the periphery, increased wetting of genomic DNA and subsequently a higher portion of spliceosomes stably engaging in active RNA processing and transcription elongation of proteostasis genes. Since no active transcription occurs in the *in vitro* droplet formation assay, these results demonstrate that PP-mediated nuclear speckle LLPS change is a cause, rather than a consequence of or response to, global transcriptional reprogramming.

PP reduces both pathological Tau and rhodopsin levels by boosting ALP and UPS, at the expense of YAP1 signaling.

Since PP treatment leads to a global increase of protein quality control gene expression, we went on to determine the effects of PP on global protein synthesis, and degradation via UPS and ALP in MEFs under two different concentrations: 0.1 and 1μM. Using puromycin incorporation assay

[58], we found that 0.1 μM of PP did not alter global protein synthesis (**Fig. 4a, b**). The lack of effects of 0.1 μM of PP on global translation was further confirmed by the lack of changes of p-eIF2α and ATF4 level (**Supplementary Fig. 17a, b**). To quantify the UPS activity, we treated MEFs with PP alone or in combination with the proteasome inhibitor MG132 and blotted for high molecular weight poly-ubiquitinated proteins. 0.1 μM PP led to a significant reduction of poly-ubiquitinated protein levels (**Fig. 4c, d**), and co-treatment with MG132 restored the level of poly-ubiquitinated proteins to a level similar to that of MG132 treatment alone (**Fig. 4c, d**). We further directly measured the activity of 20S proteasome core and found 0.1 μM PP significantly increased the 20S proteasome activity in a SON-dependent manner (**Supplementary Fig. 17c**). These data collectively indicated that 0.1 μM PP increases UPS-mediated degradation of poly-ubiquitinated protein. To quantify the autophagic flux, we utilized a tandem LC3 reporter mCherry-GFP-LC3 where an increase in the number of red-fluorescent cytosolic puncta indicates increased autolysosome formation and autophagic flux (**Fig. 4e**) [59]. 0.1 μM PP markedly increased the formation of autolysosomes (**Fig. 4f**). To verify this result, we further blocked autophagy at the late stage autophagosome-lysosome fusion step using Bafilomycin A1 (BafA) [60], and quantified the level of LC3I and LC3II with or without PP. 0.1 μM PP treatment resulted in an increased ratio of LC3II/I and reduced level of LC3II, both of which were significantly increased by BafA co-treatment to a level similar or higher than what was observed under DMSO condition (**Supplementary Fig. 17d,e**). These results collectively indicate that 0.1 μM PP also augments autophagic flux. Compared to 0.1μM PP, 1μM PP leads to a global translation repression (**Supplementary Fig. 18a, b**) concomitant with ATF4 induction (**Supplementary Fig. 10g**), but is still able to promote both UPS and ALP (**Supplementary Fig. 18c-f)**. In sum, these findings demonstrate that nanomolar concentrations of PP effectively rejuvenate nuclear speckles, enhancing both the UPS and ALP without inducing cellular stress. However, at higher micromolar concentrations, PP not only acts as a nuclear speckle rejuvenator but also induces cellular stress, likely due to its known inhibitory effects on mitochondrial activity[61, 62].

Decline of both ALP and UPS are associated with proteinopathies such as Alzheimer's disease (AD), frontotemporal dementia (FTD), Parkinson’s disease (PD) and a subtype of Retinitis pigmentosa (RP) with *RHODOPSIN* (*RHO*) mutations [63]. To determine whether PP can protect against proteinopathies via boosting UPS and ALP, we focused on two different diseases, a genetic form of RP with a mutant RHO, and tauopathy common in both AD and FTD. RP causes blindness via the primary loss of rod cells and secondary loss of cone cells. Proline to histidine at codon 23 (P23H) is the most common mutation in RHO protein, resulting in autosomal dominant RP in humans [64]. The heterozygous $Rho^{P23H/+}$ knock-in mouse develops progressive retinal degeneration that resembles the RP phenotype in patients [65, 66]. Recently, several studies suggested that boosting ERAD can protect against mouse models of RP by increasing elimination of the mutant RHO^{P23H} protein [65, 67, 68, 69]. To determine if PP can also reduce RHO^{P23H} level, we used a NIH3T3 cell line ectopically expressing RHO^{P23H} protein [70]. Treating this cell line with 0.1 μM of PP for 24 hours led to a reduction of both monomer and dimer forms of RHO^{P23H} protein in a SON-dependent manner (**Fig. 4g, h, and Supplementary Fig. 19a, b**). Blocking autophagy with ULK1/2 inhibitor SBI-0206965 or BafA, and UPS with MG132, respectively, abolished the effect of PP on reducing RHO^{P23H} protein level (**Fig. 4i, j, and Supplementary Fig. 19c-f**), suggesting that both increased ALP and UPS are responsible for the increased elimination of RHO^{P23H} by PP.

Both UPS and ALP are also involved in the degradation of tau protein in tauopathies [71, 72, 73, 74]. To test the effect of PP on tau proteostasis in mouse primary neuronal cultures, we overexpressed human Tau carrying P301S mutation - an FTD-causing mutation in the human *MAPT* gene (Tau) [75]. After treatment with increasing concentrations of PP for 24 hours, a decline in both total and phosphorylated Tau (Ser396/404) was observed in a dose-dependent manner, with approximately 50% and 65% reduction in total and p-Tau, respectively, detected at 100nM PP (**Fig. 4k**). It is noteworthy that these reductions in Tau level occurred without any observable signs of cellular toxicity (**Supplementary Fig. 19g**). PP also promoted autophagic flux in neurons, as demonstrated by an increase of LC3 II/I ratio, decreased level of p62/SQSTM1 and increased autolysosome formation (**Fig. 4k and Supplementary Fig. 19h, i**) [76]. Blocking autophagic flux with BafA dampened the effects of PP on reducing cellular Tau level (**Fig. 4l, m**). As observed in fibroblasts, PP also promoted UPS activity in neurons; however, inhibiting proteasome activity with MG132 has minimal effects on PP's ability to reduce Tau level (**Supplementary Fig. 19j, k**). Consistent with PP's ability to boost UPS and ALP, PP increased the expression of genes involved in both pathways in P301S hTau-expressing neurons (**Fig. 4n**). Collectively, these results indicate that increased autophagy flux largely underlies PP's effect in reducing Tau burden in mouse primary neurons.

Nuclear speckle rejuvenation by SON OE or PP increases global protein quality control at the cost of reduced YAP1 signaling in both MEFs (**Fig. 2i**) and neurons (**Fig. 4n**), raising an interesting question of whether the downregulation of YAP1 signaling also contributed to PP's efficacy in alleviating proteinopathy. To address this question, we restored YAP1 signaling with previously published YAP1 activators XMU-MP-1 and/or TRULI [77, 78,79]. We found that while XMU-MP-1 antagonized the downregulation of YAP1 target genes by PP as expected, it also potently dampened the upregulation of proteostasis genes (**Fig. 4o**). In addition, both XMU-MP-1 and TRULI negated PP's effect on reducing RHO^{P23H} level in NIH3T3 cells (**Supplementary Fig. 20a-d**). In addition, knocking down MST1, a kinase that inhibits YAP1 activity [80], similarly blocked the ability of PP to reduce RHO^{P23H} level (**Supplementary Fig. 20e, f**). Similarly, TRULI also blocked PP's effect on reducing Tau level in primary neurons (**Supplementary Fig. 20g, h**). These results suggest that for nuclear speckle rejuvenation to achieve the maximum effectiveness in alleviating proteinopathy, it is essential to simultaneously uphold heightened protein quality control and reduced YAP1 activity.

PP protects against mouse retina degeneration *ex vivo* and alleviates tauopathy in *Drosophila*.

Next, we assessed the effectiveness of PP in ameliorating proteinopathies by utilizing animal models of RP and tauopathy. To determine whether PP has the potential to restore gene expression changes in the retina of *Rho*$^{P23H/+}$ mice, we performed RNA-seq in the retina of one and three months old wild-type and *Rho*$^{P23H/+}$ mice and compared the gene signatures of *Rho*$^{P23H/+}$ retina with that of PP (**Fig. 5a-e**). In the retina of one month-old *Rho*$^{P23H/+}$ mice, we observed a significant downregulation of protein transport and autophagy gene expression that showed large convergence with those upregulated by PP (**Fig. 5a, b**). This includes *Reep6* gene, which regulates protein trafficking in the ER and its loss-of-function mutation causes autosomal-recessive RP in both humans and mice (**Fig. 5e**) [81]. By three months, the downregulation of proteostasis gene expression persists in *Rho*$^{P23H/+}$ mice retina, concomitant with a significant increase of YAP1-mediated cell dynamics gene expression that also overlaps with PP-downregulated genes (**Fig. 5c-e**). To directly test the efficacy of PP in protecting against RP, we treated retina explants isolated from *Rho*$^{P23H/+}$ mice with nanomolar range of PP for 10 days, and visible light optical coherence tomography (vis-OCT) imaging [82] revealed a remarkable efficacy of PP in safeguarding the mouse *Rho*$^{P23H/+}$ retina explants from degeneration. Notably, the cell counts in the outer nuclear layer closely resembled that of the WT retina explant control (**Fig. 5f-j**), indicating the protective potential of PP against degenerative processes. Moreover, no noticeable indications of toxicity were observed throughout the entire duration of the experiment, further highlighting the safety of PP as a promising therapeutic candidate.

Pan-neuronal expression of wildtype human *MAPT* gene in *Drosophila* recapitulates essential features of tauopathies, including hyperphosphorylated and misfolded tau, age-dependent neuron loss, and reduced life span [83], and SON IDR2 sequence is also conserved in flies (**Supplementary Fig 14i**). Thus, we next tested the efficacy of PP in ameliorating tauopathy in male flies that express 2N4R isoform of human Tau (*MAPT*) pan-neuronally [*elav*^{c155}-Gal4: UAS-hTau1.13 (C155>UAS-hTau1.13)] as well as in control *elav* ^{c155}-Gal4 (C155) flies [84]. Both C155>UAS-hTau1.13 and C155 flies were fed with either standard diet or diet supplemented with 25µM PP, which did not affect the normal development and growth of flies despite its effect in attenuating WNT and YAP1 signaling [85]. We quantified disease progression at different stages of fly development with both larval crawling and adult fly climbing assay at 14 and 21 days of age. PP feeding preserved motor function in C155>UAS-hTau1.13 third instar larvae and adult flies, with their locomotor performance restored to a level similar to or even slightly higher than control C155 flies fed with a standard diet (**Fig. 5k, l**). Notably, PP also enhanced the motor function of adult wild-type control (C155) flies at 21 days of age (**Fig. 5l**). This improvement is likely linked to PP's ability to promote overall proteostasis, particularly protein turnover rates, a process known to prolong health and lifespan in flies [86]. PP further extended the median lifespan of C155>UAS-hTau1.13 flies by 16% from 51 to 59 days (**Fig. 5m**). Consistent with the overall phenotypes, PP significantly reduced the level of p-Tau and to a lesser extent total Tau in the brains of 21 days-old C155>UAS-hTau1.13 flies (**Fig. 5n**). Since p-Tau are prone to misfolding and aggregation, it supports the notion that PP is increasing the overall capacity of protein quality control to remove misfolded and aggregated proteins, while having negligible effects on normal protein functions.

PP has the potential for treating tauopathy in humans.

To determine the potential of PP for treating tauopathy in humans, we studied whether gene expression signatures that are opposite of PP can be observed in brain regions of human subjects with AD. We initially performed a post-hoc analysis of a total of nineteen bulk RNA-seq datasets encompassing hippocampus, entorhinal cortex, temporal cortex and frontal cortex regions in control and AD human subjects [87], and found that genes repressed by PP have increased expression in all four brain regions of human subjects with AD (such as *YAP1, TEAD1 and AMOT*) (**Supplementary Figs. 21 and 22a**). By contrast, genes that were upregulated by PP displayed significantly decreased expression in temporal cortex (such as genes involved in ERAD: *EDEM1, SEL1L*, autophagy: *ATG13*, protein folding: *HYOU1*, and tRNA aminoacylation: *GARS*, *IARS*) (**Supplementary Figs. 21 and 22a**). To validate these findings, we further analyzed an independent single-nucleus RNA-seq (snRNA-Seq) dataset in the prefrontal cortex regions of human individuals with varying degrees of AD pathology (**Supplementary Fig. 22b**) [88]. We found that proteostasis genes upregulated by PP are consistently downregulated in all cell types with strong prominence in neurons and oligodendrocytes in both early and late-stage human AD subjects (**Supplementary Fig. 22c, d**). Genes that are downregulated by PP (those enriched in regulation of cell dynamics by YAP1) are initially downregulated in all cell types in the early stage but significantly upregulated during the late stage of AD in all cell types but inhibitory neurons (**Supplementary Fig. 22e, f**). This early to late AD progression is concomitant with strong increase of tauopathy, but not the amyloid burden in these individuals (**Supplementary Fig. 22b**). Consistent with *in vivo* data, we also observed a significant decrease of proteostasis gene expression as well as an increase of YAP1-TEAD2 target gene expression in human induced pluripotent stem cells (iPSC)-derived neurons that express the P301S 4R-Tau when compared to wild-type 4R-Tau control cells (**Fig. 6a-c**) [74]. These upregulated YAP1-TEAD2 target genes also overlap with those repressed by PP (**Fig. 6b**).

Finally, to directly test the efficacy of PP in reducing tauopathy in human, we utilized human iPSC-neurons harboring homozygous FTD-causing MAPT V337M mutation (herein referred to as V337M) and isogenic wild-type control cells [89] and treated both cell lines with nanomolar range of PP for 12~24 hours. After 24 hours of treatment with 500 nM PP, iPSC neurons exhibited no signs of toxicity, as confirmed by the LDH release assay (**Supplementary Fig. 23a, b**). Moreover, the nanomolar PP treatment did not trigger cellular stress, as indicated by the unchanged p-eIF2α levels (**Supplementary Fig. 23c**). Immunofluorescence against nuclear speckles marker SRRM2 revealed that compared to controls, V337M iPSC-neurons exhibited aberrant nuclear speckle morphology characterized by smaller size and more spherical shape, and 12 hours of 100nM PP treatment fully restored nuclear speckle morphology to normal size and diffuseness (**Fig. 6d, e**). Consequently, PP markedly reduced the level of V337M p-Tau, concomitant with increased autophagic flux (**Fig. 6d-h**). To confirm that PP rejuvenates nuclear speckles and reduces V337M p-Tau in a SON-dependent manner, we knocked down SON using lentiviral shRNA and repeated the experiment. As demonstrated in **Fig. 6i-k and Supplementary Fig. 23d**, PP failed to rejuvenate nuclear speckles or reduce p-Tau level in the presence of SON knockdown in either wild-type or V337M Tau-expressing iPSC neurons. Together, these findings indicate that PP treatment has great potential to normalize gene expression patterns and reduce Tau burden in AD/ADRD-affected humans with severe tauopathy. Further, these results provide strong support for the decline of nuclear speckles LLPS dynamics (becoming smaller and more spherical) as a driver of tauopathy.

Discussion

Several recent studies indicate that both the decline of nuclear speckle functions and dysregulated mRNA splicing are associated with proteinopathies in humans, including tauopathy, RP and amyotrophic lateral sclerosis (ALS) [90, 91, 92, 93]. For example, two studies showed that elevated Tau aggregates have the capability to relocate to the nucleus, thereby directly modifying the characteristics of nuclear speckles [92, 94]. In agreement with this study, a recently published Tau interactome in human iPSC neurons [95] also revealed strong enrichment of Tau-interacting proteins involved in regulating RNA splicing and RNA stability. Additionally, it was previously shown that cryptic splicing errors are associated with neurofibrillary tangle burden in human AD subjects [96]. In humans, among the 12 autosomal dominant RP genes identified, four encode ubiquitously expressed proteins involved in pre-mRNA splicing (including *PRPF31*, *PRPF8*, *PRPF3* and *RP9*), demonstrating the important roles of RNA processing in the pathogenesis of retinal degeneration [93]. These studies thus provide the rationale for nuclear speckle rejuvenation as a strategy for counteracting various proteinopathies.

Exploring the therapeutic potential of targeting biomolecule condensates represents an exciting avenue for research and drug development [97, 98]. Our study is proof of principle demonstrating that nuclear speckle LLPS can also be therapeutically targeted. Manipulating nuclear speckle LLPS through SON overexpression is a conceptually viable approach. However, the practical implementation of this strategy presents significant challenges due to the large size of the human SON open reading frame, making it technically difficult to design gene therapy targeting SON. That said, we cannot rule out the possibility that overexpression of specific truncated SON domains, such as SON IDR2, may be sufficient to rejuvenate nuclear speckles, and future efforts will be directed toward exploring such possibilities.

Through a high-throughput drug screen, we identified PP as a small nuclear speckle rejuvenator by directly interacting with SON and modulating nuclear speckle LLPS dynamics. Interestingly, pyrvinium is enriched with cationic amines and aromatic motifs, chemical features that were predicted to partition into various nuclear condensates [99]. PP was originally developed as an anthelmintic drug effective for treating pinworm infections [100]. Moreover, it has gained strong recent interest as an anti-cancer reagent due to its ability to inhibit WNT signaling [100]. Our current study further expands its therapeutic values to proteinopathies, including both reducing tauopathy in neurons and flies and protecting against retina degeneration in an *ex vivo* mouse RP model. Future efforts should be directed toward testing the toxicity and efficacy of this drug in mouse models of neurodegenerative diseases.

While we don't yet know the full detailed mechanisms by which PP modulates nuclear speckles dynamics and boosts proteostasis gene transcription, several lines of evidence suggest that it does so in part by reducing the surface tension and consequently increasing the surface areas of nuclear speckles via an SON-dependent manner. Our in vitro reconstitution system further showed that reduced nuclear speckles surface tension by PP further facilitates nuclear speckles wetting of chromatin [46]. Thus, since spliceosomes reside at the interfacial boundary between nuclear speckles and nucleoplasm/chromatin[44], larger surface areas also entails a higher probability of spliceosome stably engaging in mRNA processing and transcription elongation. The mechanism by which PP reduces the surface tension of nuclear speckles is not yet fully understood. While the straightforward explanation would be that PP acts as a surfactant, this seems unlikely due to its lack of hydrophilic moieties. Alternatively, it is plausible that by interacting with SON, PP weakens the intermolecular attractive interactions among different SON proteins, and/or SON and IDRs of other nuclear speckle proteins due to screening effects, leading to an overall reduction of surface tension of nuclear speckles, similar to what is previously described for the effect of increasing salt concentration on reducing surface tension for protein condensates [101, 102]. The positive charge carried by pyrvinium adds to the allure of this hypothesis. Further research is needed to elucidate the precise mechanisms by which PP influences the surface tension of nuclear speckles.

Genetic and pharmacological rejuvenation of nuclear speckles by SON and pyrvinium share similar transcriptome signatures, including upregulation of extensive protein quality control gene expression, and intriguingly, downregulation of YAP1-regulated genes involved in cell migration, cell proliferation, would healing, and extracellular matrix organization. The contrasting changes in proteostasis and YAP1-mediated cell dynamics gene expression are observed in various cell lines under proteostatic stress. Consequently, both SON overexpression and ER stress inhibits YAP/TEAD transcriptional activity and impedes cell migration. These findings demonstrate that YAP1 signaling is an inherent component of global transcriptional control of proteostasis. One possible explanation for this phenomenon is that cells need to allocate their energy towards enhancing overall proteostasis, which may come at the cost of cell proliferation, migration, and extracellular matrix organization. Therefore, an energetic trade-off between proteostasis and cell dynamics control could be crucial for maintaining cellular functions when faced with fluctuating environments, such as proteotoxic stress.

Nuclear speckles play a vital role in coordinating the opposing changes observed in proteostasis and cell dynamics regulation. Elevated SON expression facilitates increased physical interactions between nuclear speckles and XBP1s, leading to augmented transcription of proteostasis genes. Since the number of proteostasis genes under the control of SON surpasses those directly regulated by XBP1s, we postulate that nuclear speckles can be recruited to additional proteostasis bZIP TFs upon rejuvenation, possibly via increased wetting between nuclear speckle and TF-mediated condensates [46]. Future work with unbiased profiling of nuclear speckle composition (via proximity labeling for example) can unveil the detailed molecular mechanisms through which nuclear speckle rejuvenation globally activates the proteostasis gene program. On the other hand, much less is clear on how nuclear speckle rejuvenation represses YAP1 transcription activity. Upon SON overexpression and pyrvinium treatment, we found a significantly reduced level of nuclear YAP1 protein and a lower nucleus/cytosol ratio, indicating an active nuclear exclusion of YAP1 protein. Like nuclear speckles, YAP1 can also form biomolecular condensates, and a recent study reported that YAP1 nuclear condensates and the nuclear speckles showed limited nuclear co-localization [103], suggesting a low level of wetting of these two condensates under normal physiological conditions. Pending further investigation, we speculate herein that nuclear speckles rejuvenation may further reduce the wetting of these two condensates, resulting in the alteration of YAP condensate composition, and ultimately its nuclear exclusion.

While both proteostasis and YAP1 signaling are downstream of nuclear speckles, direct antagonistic reciprocal interactions between these two are likely to be present as well. A recent study reported that in *Drosophila*, the proteostasis output gene Bip can sequester the fly YAP1 ortholog Yorkie, in the cytoplasm to restrict Yorkie transcription output [104]. Conversely, in undifferentiated pleomorphic sarcoma, YAP1 can suppress PERK and ATF6-mediated UPR target expression, and treatment with the YAP1 inhibitor Verteporfin upregulated the UPR and autophagy [105]. The latter is further consistent with our findings showing that restoring YAP1 activity dampened the efficacy of PP on activating protein quality control gene expression and reducing proteinopathies. These findings indicate that in order to maximize the effectiveness of nuclear speckle rejuvenation, it is crucial to maintain elevated levels of protein quality control while simultaneously reducing YAP1 activity. Thus, a delicate balance between protein quality control and YAP1 activity appears essential for effective nuclear speckle rejuvenation. This observation may also explain why therapies merely aimed at activating protein quality control pathways often have limited efficacies. Supporting this notion, while reduced expression of genes involved in ERAD and autophagy are observed in the brains of individuals with AD, these subjects also exhibit elevated gene expression of *YAP1*, *TEAD1,* and other YAP1 target genes, consistent with previous studies [87, 106]. Increased YAP1 target gene expression was further observed in human iPSC tauopathy model as well as in the retina of Rho $^{P23H/+}$ mice. These results collectively highlight the importance of suppressing YAP1 signaling as a potential strategy for managing both AD and RP.

In conclusion, our study makes substantial conceptual contributions to the broader proteostasis framework by incorporating nuclear speckle LLPS and YAP1 signaling as critical components. From a translational perspective, our research unveils the promising therapeutic potential of nuclear speckle rejuvenation in tackling proteinopathies, achieved by simultaneous activation of protein quality control and inhibition of YAP1 activity. Additionally, our findings underscore the significance of harnessing the 12-hour oscillator to unveil hidden principles of proteostasis control.

Materials and methods

Mice

For retinal explant studies, wildtype C57BL/6J and $Rho^{P23H/+}$ knock-in mice (Jackson Laboratory Strain #017628) were euthanized by CO2 and retinae were isolated for culture. The animal studies were carried out in accordance with the National Institutes of Health guidelines and were granted formal approval by the University of Pittsburgh's Institutional Animal Care and Use Committee (approval numbers IS00013119 and IS00023112).

Larva crawling assay

PP solubilized in DMSO were diluted directly into the fly medium at the final concentration of 25 µM and vortexed extensively to obtain homogeneous culture. Crawling assays were performed on 1.5% agarose plates made with a 2.3:1 combination of grape juice and water. A sample size of 10 to 15 larvae were selected for each genotype and assays were done using larvae in the third instar state. The larvae were first removed from vials and gently placed into a petri dish containing deionized water to allow for residual food to be washed off the body. After 15 seconds, the larvae were transferred to a petri dish containing the 1.5% agarose mixture and were given one minute to rest. They were then transferred to a second dish filled with the 1.5% agarose mixture and timed immediately for one minute, during which their crawling performance was measured. A transparent plastic lid was placed on top of the plates and the crawling path of the larvae were traced. Observations of the crawling activity were done under a light microscope. The brightness and distance of the light source above the plates were kept constant across all trials and genotypes. The crawling paths of the larvae were measured using FIJI ImageJ and the average distance traveled was taken for each genotype.

Adult fly climbing assay

Male adult Drosophila melanogaster flies at 14 and 21 days of age fed with a normal diet or diet supplemented with 25 µM PP were used for assessing climbing ability. Flies were grouped into cohorts of the same sex, pre-mated, and age-matched, with a maximum of 20 individuals per vial (usually 5-15). All flies used in each trial were hatched within a 3-day window. The evening prior to each assay, flies were gently transferred to fresh tubes to allow for grooming and access to food. To ensure consistent conditions, assays were conducted at approximately the same time of day with a consistent ambient light setting. A custom climbing vial was employed, divided into six compartments, each labeled with a number (1 to 6) to denote climbing speed. The vial was positioned against a white background to enhance visibility during photography. Flies were transferred from their housing vial to the climbing vial, which was covered with a plastic plate on top. To initiate the assay, the flies were gently tapped to the bottom of the vial and allowed 10 seconds to climb. A cell phone camera was used to capture a photograph of the vial. Care was taken to ensure the camera was level with the vial, all flies were visible, and the background was free from stains or spots. The number of flies in each compartment of the climbing vial was counted at each time point and recorded on a dedicated worksheet. Each cohort of flies underwent five consecutive trials, with approximately 1 minute of rest between each trial. The average score of each cohort was determined by dividing the total score by the total number of flies.

Fibroblast cell culture and drug treatment

MEFs and NIH 3T3 cells were cultured at 37°C and 5% CO_2 in Dulbecco's Modified Eagle's Medium (DMEM, glucose 4.5 g/L with phenol red) and supplemented with 10% fetal bovine serum (FBS), 1 mM sodium pyruvate (Gibco), and penicillin (100 U/mL)-streptomycin (100 μg/mL) (Gibco). Methods for the manipulation of *Son* (transient knockdown or constitutive overexpression) and validation of changes to protein (SON) levels with regards to the mRNA-Seq data are previously described in [9]. For Tu treatment, 100 ng/mL Tu (in DMSO) for six hours was used unless otherwise noted. NB (HY-50904), PB (HY-12047), PH (HY-B0883), PP (HY-A0293), MG-132 (HY-13259), SBI-0206965 (HY-16966) and XMU-MP-1 (HY-100526) were purchased through MedChemExpress and BafA (1334) were purchased from Tocris. All drugs were handled per manufacturer instruction.

siRNA Transient Transfections

MEFs were transfected with 10μM of different siRNAs for 24~48 hours with Lipofectamine RNAiMAX reagents (Life technologies) per the manufacturer's instructions. Sources of siRNA are as follows: siGENOME non-targeting siRNA pool (Dharmacon, D-001206-1305), siGENOME SMARTpool son siRNA (Dharmacon, L-059591-01-0005), siGENOME SMARTpool Stk3/Mst1 siRNA (Dharmacon, L-040440-00-0005), and siGENOME SMARTpool Stk4/Mst2 siRNA (Dharmacon, L-059385-00-0005).

Primary neuron cell culture and P301S-Tau virus infection

The cerebral cortices of 3-4 neonate mice (P0) were dissected on ice, the meninges were removed and placed in the cold dissection medium (DM), consisting of 6 mM MgCl2 (Sigma M1028-100 ml), 0.25 mM $CaCl_2$ (Sigma C7902), 10 mM HEPEs (100X), 0.9% Glucose, 20 μM D-AP5 (Cayman, NC1368401), and 5 μM NBQX (Tocris Bioscience, 10-441-0). After dissection, the brain tissues were washed with DM 1~2 times and incubated with 13mL of DM containing papain (Worthington, LK003176) in 37°C water bath for 20 min. The suspension was shaken every 5 min. 10mL media containing 18 ml DM + 2 ml low OVO + 133 ul DNase I (dilute 10X low OVO and 150x DNase I to DM) were added into the suspension to stop the digestion in 37°C water bath for 5 min. The solution was taken off and 10 ml fresh solution was added in. Then the tissues were triturated until there were no visible chunks, and the solution was filtered through the 70 μm cell strainer. The cell solution was then centrifuged at 1000 rpm for 10 min and the supernatant was discarded. The cell pellet was gently resuspended in 20 ml B27/NBM/High glucose media, and the suspension was centrifuged at 850 rpm for 5 min. After that, the supernatant was taken off and B27/NBM (1 ml/mouse brain) was added to resuspend the cells until single cell solution. The cells were counted and plated onto the coverslips at 250k in 24-well plates for imaging or 800k in 12-well plates for qRT-PCR or Western blots. AAV-P301S hTau (Viro-vek) were infected at DIV1 at 100 MOI.

Human iPSC-derived neurons culture

Human iPSC-derived neurons were pre-differentiated and differentiated as described [89]. Briefly, iPSCs were pre-differentiated in Matrigel-coated plates or dishes in N2 Pre-Differentiation Medium containing the following: KnockOut DMEM/F12 as the base, 1× MEM non-essential amino acids, 1× N2 Supplement (Gibco/Thermo Fisher Scientific, cat. no. 17502-048), 10 ng/ml of NT-3 (PeproTech, cat. no. 450-03), 10 ng/ml of BDNF (PeproTech, cat. no. 450-02), 1 μg/ml of mouse laminin (Thermo Fisher Scientific, cat. no. 23017-015), 10 nM ROCK inhibitor and 2 μg /mlof doxycycline to induce expression of mNGN2. After 3 d, on the day referred to hereafter as Day 0, pre-differentiated cells were re-plated into BioCoat poly-D-lysine-coated plates or dishes

(Corning, assorted cat. no.) in regular neuronal medium, which we refer to as +AO neuronal medium, containing the following: half DMEM/F12 (Gibco/Thermo Fisher Scientific, cat. no. 11320-033) and half neurobasal-A (Gibco/Thermo Fisher Scientific, cat. no. 10888-022) as the base, 1× MEM non-essential amino acids, 0.5× GlutaMAX Supplement (Gibco/Thermo Fisher Scientific, cat. no. 35050-061), 0.5× N2 Supplement, 0.5× B27 Supplement (Gibco/Thermo Fisher Scientific, cat. no. 17504-044), 10 ng/ml of NT-3, 10 ng/ml of BDNF and 1 μg/ml of mouse laminin. Neuronal medium was half-replaced every week.

Efficacy test of PP in Retina explant culture

Wild type and *Rho*$^{P23H/+}$ mice were euthanized at P15, and retina explants were isolated and cultured as previously described[107, 108]. Briefly, eyeballs were enucleated and incubated in Ames solution containing 0.22 mM L-cysteine (Sigma-Aldrich) and 20 U papain (Worthington, Freehold NJ, USA) at 37 °C for 30 min. The digestion was stopped by transferring the eyes to Dulbecco's modified Eagle's medium (DMEM; Gibco) containing 10% fetal calf serum (FCS; Gibco) and penicillin &streptomycin antibiotics (1x, GenClone) at 4 °C for 5 min. The eye cup was made by gently removing the cornea, iris and lens. Each eye cup was flattened by four radio cuts and the sclera was then carefully peeled off from the retina:RPE complex. The retina:RPE explant was transferred to a trans well insert with 0.4-micron pore polycarbonate membrane (ThermoFisher) sitting on the surface of 1.5 mL of neurobasal-A plus medium (Gibco) containing 2% B27 supplement (Gibco) in a 6-well cell culture plate, and the RPE layer was facing down the transwell membrane. The retinal explants were cultured at 37 °C with 5% CO_2.The medium was replaced with fresh medium containing 0.5 μM PP after 24 h, which was replaced again every 2 days until 10 days in culture (DIV). A visible light optical coherence tomography (vis-OCT) prototype [109] was utilized to monitor the explants noninvasively at day 0 and day 10. Retinal layers were segmented automatically using a deep learning method and then manually corrected by a customized software to calculate the retinal thickness. Retina explants were collected at 10 DIV and processed for fixation, dehydration, paraffin embedding, cross-sections, dewaxing, rehydration and hematoxylin and eosin (H&E) staining[110]. H&E-stained slides were imaged by regular light microscopy with a color camera, and the number of nuclei in the outer nuclear layer (ONL) was calculated manually.

Autophagy reporter assay

To express the LC3 reporter in the neurons, the primary mouse neuronal cultures were infected with the homemade lentivirus-mCherry-GFP-LC3 for 7 days. The florescent signal from the vacuoles at different stages were acquired by confocal imaging. The mCherry-GFP-LC3 fluorescence images were acquired with a Leica TCS SP8 confocal system using 63x oil-immersion objective. 488 nm and 568 nm laser were used to excite the GFP and mCherry, respectively. Images were taken with the same confocal settings. Minor image adjustment (brightness and/or contrast) was performed in ImageJ. The GFP and mCherry signal collected were merged into one image to quantify the red, green, and yellow vacuoles for quantification of different types of vacuoles. The different colored fluorescent signal was manually counted in each cell, and each point represents the average number of the specific vacuole for one cultured cell. For autophagy reporter assay in MEFs, pCDH-EF1a-mCherry-EGFP-LC3B was a gift from Sang-Hun Lee (Addgene plasmid # 170446 ; http://n2t.net/addgene:170446 ; RRID:Addgene_170446) [111] and purchased from addgene. Lentivirus was packaged from HEK293T cells as previously described [19] and was used to infect MEFs with a MOI of 3 three times. The quantification was performed essentially the same way as in neurons.

TEAD luciferase reporter assay

MEFs with the CRISPRa system either overexpressing *Son* or serving as controls used in this assay were previously described in [112]. Briefly, cells were seeded at a density of 7000 cells per well in a 96-well plate with a clear bottom and white walls. Cells were then transfected using the Lipofectamine 3000 transfection kit (ThermoFisher #L3000015) for 22 hours with the 8xGTIIC-luciferase plasmid, a gift from Stefano Piccolo (Addgene plasmid # 34615 ; http://n2t.net/addgene:34615 ; RRID:Addgene_34615) [113]. The Dual-Glo Luciferase Assay System (Promega #E2920) was used with a SpectraMax i3x plate reader (Molecular Devices) to measure firefly luciferase signal (500ms integration time, 1mm from the plate read height).

Proteasome 20S activity assay

The proteasome 20S activity assay was performed per manufacturer's instruction (Sigma Aldrich, MAK172). Briefly, MEFs transfected with scrambled control or *Son* siRNA were treated with DMSO or 100nM PP for 24 hours. After treatment, cells were washed with PBS and cultured in phenol-free DMEM. Assay reagents were added directly to the cells, and fluorescent signals were measured by a fluorescent plate reader 2 hours later at λex = 490 nm and and λem = 525 nm. The final signal was corrected by subtracting the fluorescence of the background blank (medium without cells) from the fluorescence of all test wells.

Scratch assay

Cells were grown until they were 100% confluent, ER stress was induced as previously described, and then a single scratch was performed with a pipette tip per well. Cells were imaged immediately after scratching (0hr) and then after 23hr. The Cell Profiler [114] "Wound Healing" pipeline (https://cellprofiler.org/examples) was used to measure the "Percentage of Gap Filled".

Immunoblot

Different cells were harvested and fractionated to produce cytosolic and nuclear lysates using the NE-PER kit (Thermo Fisher Scientific). For whole cell lysates, cells were lysed in RIPA buffer. Both protease and phosphatase inhibitors were included in the respective lysis buffer. ~47 µg of protein was separated on a 4%-15% gradient SDS-polyacrylamide gel (Bio-Rad) which were transferred to nitrocellulose membranes, stained with Ponceau S stain, washed, blocked with 5% non-fat milk, and incubated overnight at 4°C with the following primary antibodies: anti-α-Tubulin (Cell Signaling Technology (C.S.T.) #2144), anti-Lamin A/C (C.S.T. #4777), anti-SON (Abcam #121033 and LSBio LS-C803664), anti-YAP1 (C.S.T. #12395), anti-GFP (C.S.T. #2956), anti-Tau (Sigma-Aldrich, #A0024), anti-p-Tau (a gift from Dr. Peters Davies), anti-β-actin (C.S.T. #4970), anti-puromycin (BioLegend 381502), anti-ubiquitin (C.S.T. #58395), anti-LC3-I/II (C.S.T. #2775), anti-p62 (C.S.T. #23214), anti-ATF4 (C.S.T. #11815), anti-ATF6 (Novus 70B1413.1), anti-MST1 (C.S.T. #3682), anti-MST2 (C.S.T. #3952), anti-eIF2α (C.S.T. #5324), anti-p-eIF2α (Ser51) (C.S.T. #3597) and anti-XBP1s (BioLegend 658802). The 1D4 anti-rhodopsin antibody[115] was obtained as a gift from Dr. Krzysztof Palczewski's laboratory. Membranes were treated with the appropriate secondary antibody conjugated to horseradish peroxidase the following day and then ECL Prime Western Blotting Detection Reagent (Cytiva) was applied. A Bio-Rad ChemiDoc MP Imaging System was used to visualize the signal, and signal intensities were determined with ImageJ [116]. For anti-Rhodopsin western blot, the protein samples were not boiled before loading.

Cellular thermal shift assay (CETSA)

EGFP::SC35 MEFs with EGFP knocked into the N-terminal of mouse *Srsf2* locus (previously described in [9]) were treated with either DMSO or 3μM PP for 50 minutes at 37°C. Cells were then trypsinized and resuspended in PBS with either DMSO or 3μM PP and 100 μL of the suspensions were distributed to PCR tubes for the thermal shift assay (three minutes at a range of temperatures). The temperatures used were: 42.0°C, 42.5°C, 43.9°C, 46.2°C, 49.3°C, 53.3°C, 57.9°C, 62.1°C, 65.2°C, 67.8°C, 69.2°C, and 70.0°C. After the samples were heated, they sat at 20°C for three minutes, were snap frozen in liquid nitrogen and thawed for three cycles to lyse the cells, and then spun at 20,000 x g for 20 minutes at 4°C. The supernatant was then removed, and immunoblotting was performed using anti-GFP (C.S.T. 2956), anti-ATF4 (C.S.T. #11815), and anti-SON (Lifespan Biosciences #LS-C803664-100), followed by appropriate secondary antibody. Band intensity on the blots were relative to the intensity of the 42°C band and were normalized so that this band's (42°C) intensity was set equal to 1.

Protein purification and *in vitro* droplet formation assay

Regions of SON and the entire SRSF2 protein were fused to mCherry. cDNA encoding the SON-IDR N terminal (region 1), SON-IDR C-terminal (region 2), and SRSF2 were each cloned into the expression vector pET21a (+)-Histag-mCherry (Addgene plasmid # 70719) (Niederholtmeyer et al., 2015). The plasmids obtained were transformed into C3013 *E. Coli* (NEB C3013I). Fresh bacterial colonies were inoculated into LB media containing ampicillin and grown overnight at 37°C. Overnight cultures were diluted in 500mL of LB broth with ampicillin and grown at 37°C until reaching OD 0.6. IPTG was then added to 2mM, and growth continued for 3h at 37°C. The cells were pelleted and stored frozen at -80°C. Bacterial pellets were resuspended in 15mL of Buffer A (50 mM Tris-HCl, 500 mM NaCl) containing protease inhibitors (Pierce, A32965) and 10mM imidazole. The suspension was sonicated on ice for 15 cycles of 30 sec on, 30 sec off. The lysate was centrifuged for 40 minutes at 15,000 RPM at 4°C to clear debris, then added to 2mL of preequilibrated Ni-NTA agarose beads (Qiagen cat no. 30210). The agarose lysate slurry incubated for 1.5hrs at 4°C while rocking, then allowed to flow through the column. The packed agarose was washed with 15mL of Buffer A with 10mM imidazole. Protein was eluted with 5mL of Buffer A containing 15mM imidazole, 10mL Buffer A containing 100mM imidazole, then 10mL Buffer A containing 200mM imidazole. All elutions were collected in 1mL fractions. Aliquots of the collected fractions were run on an SDS-PAGE gel and stained with Imperial Protein Stain to verify the amount and purity of the protein. Fractions containing protein were combined and dialyzed against Dialysis Buffer (50mM Tris-HCl, 500mM NaCl, 10% glycerol, 1mM DTT). Recombinant mCherry fusion proteins were concentrated and desalted to 200uM protein concentration and 125mM NaCl using Amicon Ultra centrifugal filters (MilliporeSigma cat no. UFC801024) following manufacturer's instructions. 20uM of recombinant protein was added to Droplet Buffer (50mM Tris-HCl, 10% glycerol. 1mM DTT, 10% PEG) containing indicated final salt and pyrvinium concentrations. For droplet formation assay with Hela nuclear extract supplementation, NE was added to different concentration of SON IDR2 at the final concentration of 1.5mg/ml in Droplet buffer (20mM HEPES, pH 7.9, 20% glycerol, 125mM KCl, 0.2mM EDTA, 0.5mM DTT, 10% DEG). For droplet formation assay with GFP::SRSF2 MEF nuclear extract supplementation, NE was added to 10uM SON IDR2 at the final concentration of 0.6mg/ml in Droplet buffer. A custom imaging chamber was created by placing strips of tape on a glass coverslip, forming a square. The protein solution was immediately loaded onto the center of the square and covered with a second glass coverslip. Slides were then imaged with a Leica confocal microscope with a 63x oil objective. The image series were taken over a 20-minute time span with 1 image every 30 seconds.

Mass spectrometry to profile condensates composition

Hela nuclear extract samples were thawed at room temperature, vortexed for 10 minutes, bath sonicated for 5 minutes and centrifuged at 13000g for 10 minutes at room temperature prior to quantification of total protein by a Pierce 660 Protein Assay (Thermo Scientific #22660). Condensates were obtained by centrifuging at 10,000xg for 10 minutes and resuspended in 5%SDS in 50 mM TEAB prior to total protein quantification. Protein digestion was carried out on 10 µg of protein from each sample on S-trap micro columns (Protifi) according to the manufacturer's protocol. Following digestion, peptide samples were then dried in a speedvac and resuspended in a solution of 3% acetonitrile and 0.1% TFA and desalted using Pierce Peptide Desalting Spin Columns (Thermo Scientific # 89851). Eluants were dried in a speedvac and resusupended in a solution of 3% acetonitrile and 0.1% formic acid to a final concentration of 0.5 µg/µL. Mass spectrometry analysis was conducted on a Thermo Fisher QE-HFX coupled to a Vanquish Neo UHPLC. Approximately 1 µg of each sample was loaded onto an EASY-Spray PepMap RSLC C18 column (2 µm, 100A, 75µm x 50 cm) and eluted at 300 nl/min over a 120-minute gradient. MS1 spectra were collected at 120,000 resolution with a full scan range of 350 – 1400 m/z, a maximum injection time of 50ms and the automatic gain control (AGC) set to 3e6. The precursor selection window was 1.4 m/z and fragmentation were carried out with HCD at 28% NCE. MS2 were collected with a resolution of 30,000, a maximum injection time of 50ms and the AGC set to 1e5 and the dynamic exclusion time set to 90s. The collected MS data were analyzed using MSFragger V4.0[1] and searched against the human SwissProt database. The search parameters were set as follows: strict trypsin digestion, missing cleavage up to 2, carbamidomethylation of cysteine as static modification, oxidization of methionine and protein N-terminal acetylation as variable modification, a maximal mass tolerance of 20 ppm for the precursor ions and 20ppm for the fragment ions, and false detection rate (FDR) was set to be 1%.

1,6-hexanediol treatment to examine effects of PP on LLPS

A 10% (w/v) 1,6-hexanediol (1,6-HD, MilliporeSigma) solution was prepared in Dulbecco's Modified Eagle's Medium (DMEM, glucose 4.5 g/L with phenol red) supplemented with 10% fetal bovine serum (FBS), 1 mM sodium pyruvate (Gibco), and penicillin (100 U/mL)-streptomycin (100 µg/mL) (Gibco). To examine NS LLPS dynamics, EGFP::SC35 MEFs (previously described in [9]) were treated with DMSO or 1 µM PP for 30 minutes and then treated with 0, 1, 2, or 10% 1,6-HD for 20 minutes. Cells were fixed in 2% paraformaldehyde, stained with bisBenzimide H 33258 (Hoechst), and then imaged. Image analysis was completed in Cell Profiler; briefly, the process was to image the cells in the 405 (Hoescht), 488 (GFP), and 555 (high intensity to image whole cells) and then use the 405 channel to determine the nuclei boundaries, 488 to determine EGFP::SC35, and 555 to determine the area of the whole cells. We differentiated nuclear and cytosolic areas by subtracting the 405 signals from the 555 signals. 488 signal was then quantified in the aforementioned nuclear area and cytosolic area and compared. 20+ cells were measured for each condition. The average Manders coefficient was determine with ImageJ [116] by averaging the tM1 and tM2 values.

This same process was used to examine the effects of PP on GW182 and MED1 except in wildtype MEFs. The signal was identified by immunofluorescence (IF). Briefly, IF was performed by fixing cells with 4% paraformaldehyde in PBS, permeabilizing with 0.2% Triton X-100 in PBS, blocked with 2% bovine serum albumin in PBS, and then incubated with primary antibody (GW182 (ab156173, Abcam) or MED1 (ab60950, Abcam)) diluted per manufacturer's recommendation overnight at 4°C. Cells were then treated with the appropriate 1:1000 secondary antibody overnight at 4°C, stained with Hoechst the following day, and then mounted with ProLong Gold Antifade (Invitrogen). Signal (either IF or endogenous GFP) sphericity was determined as previously described in [9]. 20+ cells were measured for each condition.

Reverse transcription quantitative polymerase chain reaction (RT-qPCR)

For Reverse transcription-quantitative polymerase chain reaction (RT-qPCR), cDNA was produced using the Superscript III (Thermo Fisher) kit and qPCR was completed using the SYBR Green system (Thermo Fisher) in a CFX384 Real-Time System (Bio-Rad). Endogenous *β-actin* levels were used as controls. The qPCR primer sequences were as follows:

β-actin forward: AAGGCCAACCGTGAAAAGAT
β-actin reverse: GTGGTACGACCAGAGGCATAC
Amot forward: CTGGAAGCAGATATGACCAAGT
Amot reverse: GGTGTTAGGAGAGTGGCTAATG
Atf4 forward: CCACTCCAGAGCATTCCTTTAG
Atf4 reverse: CTCCTTTACACATGGAGGGATTAG
Atg4c forward: GTGCGGAATGAGGCTTATCA
Atg4c reverse: CCAGACTTCTTCCCAAACTCTATC
Bmp4 forward: AACGTAGTCCCAAGCATCAC
Bmp4 reverse: CGTCACTGAAGTCCACGTATAG
Ern1 forward: TCCTAACAACCTGCCCAAAC
Ern1 reverse: TCTCCTCCACATCCTGAGATAC
Fdz1 forward: GAGATCCACCTTCCAGCTTTAT
Fzd1 reverse: CACTCCCTCTGAACAACTTAGG
Hyou1 forward: GAGGCGAAACCCATTTTAGA
Hyou1 reverse: GCTCTTCCTGTTCAGGTCCA
Manf forward: GACAGCCAGATCTGTGAACTAAAA
Manf reverse: TTTCACCCGGAGCTTCTTC
Rnf166 forward: GAAGACACACTCCCGCTTTA
Rnf166 reverse: CTGAGACCAACTCTCCTTGTG
Sirt2 forward: CATAGCCTCTAACCACCATAGC
Sirt2 reverse: GTAGCCTGTTGTCTGGGAATAA
Sqstm1 forward: AACAGATGGAGTCGGGAAAC
Sqstm1 reverse: AGACTGGAGTTCACCTGTAGA
Tgfb3 forward: CCACGAACCTAAGGGTTACTATG
Tgfb3 reverse: CTGGGTTCAGGGTGTTGTATAG
Ube2q2 forward: TTCCTAAGCACCTGGATGTTG
Ube2q2 reverse: CTCCTCCTCTTCCTCTTCTTCT
Xbp1 forward: GGGTCTGCTGAGTCC
Xbp1 reverse: CAGACTCAGAATCTGAAGAGG
Cul5 forward: GAACACAGGCACCCTCATATT
Cul5 reverse: AGTTACACTCTCGTCGTGTTTC
Psmg1 forward: CCAGTGGTTGGAGAAGGTTT
Psgm1 reverse: GGGTCTTGTAGTCTGTGATGTG
Atg14 forward: CATTCCCTGGATGGGCTAAA
Atg14 reverse: CCTCAGGAACAAGAAGGAAGAG
Yap1 forward: CCAATAGTTCCGATCCCTTTCT

Yap1 reverse: TGGTGTCTCCTGTATCCATTTC

Chromatin Immunoprecipitation (ChIP)

ChIP for SC35 was performed using anti-SC35 antibody (ab11826, Abcam) as previously described [117]. Briefly, mouse liver samples were submerged in PBS + 1% formaldehyde, cut into small (~1 mm3) pieces with a razor blade and incubated at room temperature for 15 minutes. Fixation was stopped by the addition of 0.125 M glycine (final concentration). The tissue pieces were then treated with a TissueTearer and finally spun down and washed twice in PBS. Chromatin was isolated by the addition of lysis buffer, followed by disruption with a Dounce homogenizer. The chromatin was enzymatically digested with MNase. Genomic DNA (Input) was prepared by treating aliquots of chromatin with RNase, Proteinase K and heated for reverse-crosslinking, followed by ethanol precipitation. Pellets were resuspended and the resulting DNA was quantified on a NanoDrop spectrophotometer. An aliquot of chromatin (10 µg) was precleared with protein A agarose beads (Invitrogen). Genomic DNA regions of interest were isolated using 4 µg of antibody. Complexes were washed, eluted from the beads with SDS buffer, and subjected to RNase and proteinase K treatment. Crosslinking was reversed by incubation overnight at 65 °C, and ChIP DNA was purified by phenol-chloroform extraction and ethanol precipitation. ChIP-qPCR for MEFs were essentially performed the same way as previously described with anti-SC35 (ab11826, Abcam) and anti-XBP1s antibody (Biolegend 658802), except that the MEFs were directly fixed with 1% formaldehyde before subject to nuclei isolation and chromatin immunoprecipitation. The primers used for ChIP-qPCR are as follows:

Gene desert forward primer: GCAACAACAACAGCAACAATAAC
Gene desert reverse primer: CATGGCACCTAGAGTTGGATAA
Xbp1 promoter region forward primer: GGCCACGACCCTAGAAAG
Xbp1 promoter region reverse primer: GGCTGGCCAGATAAGAGTAG
Xbp1 gene body region forward primer: CTTTCTCCACTCTCTGCTTCC
Xbp1 gene body region reverse primer: ACACTAGCAAGAAGATCCATCAA
Manf promoter region forward primer: ACAGCAGCAGCCAATGA
Manf promoter region reverse primer: CAGAAACCTGAGCTTCCCAT
Manf gene body region forward primer: CAACCTGCCACTAGATTGAAGA
Manf gene body region reverse primer: AGGCATCCTTGTGTGTCTATTT
Hyou1 promoter region forward primer: GACTTCGCAATCCACGAGAG
Hyou1 promoter region reverse primer: GACTTCTGCCAGCATCGG
Hyou1 gene body region forward primer: TGGAAGAGAAAGGTGGCTAAAG
Hyou1 gene body region reverse primer: TCCCAAGTGCTGGGATTAAAG

HTS of FDA-approved drugs and quantitative imaging analysis

EGFP::SC35 MEFs were seeded in black 384 well plate with glass bottom (Cellvis). The FDA-approved compound library (100nL per drug) was stamped to 384-well tissue culture plates using CyBio Well vario (Analytik Jena). Compound solutions were then added to the cell plate at the final concentrations of 10 µM using a BRAVO liquid handler. After 18 hours of treatment, culture media was removed, and cells were fixed with 4% PFA followed by DAPI staining. Cells were imaged using a GE INCELL 2200 with 60x lens. Maximum intensity projection images were captured, and nuclear speckles sphericity was quantified with CellProfiler as previously described in [9]. Briefly, for speckle i the sphericity is defined as equation 1:

$$\text{Sphericity } i = 2\sqrt{\pi} * \sqrt{\text{area } i} \div \text{circumference } i \tag{1}$$

So that a perfect circle will have a sphericity of 1, and a line will have a sphericity of 0. To calculate the average sphericity of a given image that has k total speckles, we calculated the area-weighted average as described in equation 2.

$$Average\ sphericity/image = \sum_1^k Sphericity\ i \times area\ i \,/\, \sum_1^k area\ i \tag{2}$$

For the secondary screening to determine if compounds affected nuclear speckles morphology in a dose-dependent manner, specific compounds were selected using a TTP Mosquito X1 followed by serial dilutions of compounds that were prepared using a Bravo automated liquid handling platform (Agilent). Cells were treated, imaged, and analyzed according to the same protocol described above. For the tertiary screen we used MEFs with a *Perk* promoter-driven dGFP as previously described [118]. Cells were treated with drugs of interest and either DMSO or Tu at the same time as described above and both GFP/cell and cell number were determined with CellProfiler as previously described [3]. For both dose-response and *Perk* promoter-driven dGFP experiments, eight biological replicates were performed per drug per dose.

Immunofluorescence

Immunofluorescence was performed as previously described [119]. Briefly, liver OCT sections or cells cultured in chamber slide were fixed in cold acetone for 10 mins at -20 ºC. The sections were then air dried, rehydrated with PBS and permeabilized with PBS+ 0.1% Triton X-100. The sections were then blocked with 10% goat serum at room temperature for 1 hour. For mouse liver tissues, primary antibodies against SC35/SRRM2 (ab11826, Abcam) were conjugated to Alexa-488, respectively per manufacture's protocol and added to the OCT section at 1:1000 dilution overnight at 4 ºC. Next day, sections were washed five times with PBS and counterstained with DAPI before mounting (with ProlongGold Glass) and imaging using Leica SP8 lightening confocal microscope (Leica Microsystems). For cell culture experiment, after incubation with anti-SRRM2 primary antibody, Alex488-conjugated secondary antibodies were added and the rest was performed as essentially the same way.

mRNA-seq and transcriptome analysis

For all mRNA-seq or RT-qPCR, total mRNA was isolated and purified from MEFs using the PureLink RNA Mini Kit (Thermo Fisher). For mRNA-seq, samples were submitted to the UPMC Genome Center for quality control, mRNA library preparation (Truseq Stranded mRNA (poly-A pulldown), and sequencing (paired-end 101 bp reads and ~40 million reads per sample). The sequencing was performed on a NextSeq 2000 sequencer.

For the *son* overexpression or knockdown (OE/KD) sequencing data, the raw RNA-seq FASTQ files were analyzed by FastQC for quality control. Adaptors and low-quality reads were filtered by Trimmomatic [120]. Then the processed reads were aligned by HISAT2 [121] against mouse reference mm10. For gene-level intron/exon quantification, bedtools software [122] was used to collect and count reads that aligned to any intron/exon of the given gene. If one read spans across multiple exons of the same gene, it will only be counted once. If one read spans intron/exon junction, it will only be counted as intron. The intron/exon count was normalized by gene length and total reads for FPKM normalization.

The analysis of drug-treated samples was done using Galaxy [123]: Trim Galore was used for quality control [124] and Salmon [125] was used to normalize the paired-end reads (TPM method). The online

3D RNA-Seq [126] pipeline was used to determine upregulated and downregulated genes, in addition to generating the PCA plot.

For RNA-seq of *Rho*$^{P23H/+}$ and wild-type mice, total RNA was isolated from retinae isolated from mice at 1, 3, and 6 months of age using TRIzol organic extraction. RNA-seq was performed by QuickBiology Inc. RNA integrity was checked by Agilent Bioanalyzer. Libraries for RNA-seq were prepared with KAPA Stranded mRNA-Seq poly(A) selected kit (KAPA Biosystems, Wilmington, MA) using 250 ng toal RNAs for each sample. Paired end sequencing was performed on Illumina HighSeq 4000 (Illumina Inc., San Diego, CA).

The reads were first mapped to the latest UCSC transcript set using Bowtie2 version 2.1.0[127] and the gene expression level was estimated using RSEM v1.2.15[128]. TMM (trimmed mean of M-values) was used to normalize the gene expression. Differentially expressed genes were identified using the edgeR program[129]. Genes showing altered expression with $p < 0.05$ and more than 1.5-fold changes were considered differentially expressed. Goseq was uesd to perform the GO enrichment analysis and Kobas was used to perform the pathway analysis.

mRNA splicing rates analysis

The mRNA processing rate was estimated by the simple kinetic model (equation 3) where pre-mRNA was converted to mature mRNA with the mRNA processing rate *Kp* and the mature mRNA is subject to decay with a constant decay rate *Kd*.

$$Pre - mRNA \xrightarrow{Kp} mature\ mRNA \xrightarrow{Kd} \tag{3}$$

Under the basal condition (DMSO), we assume a steady state of mature mRNA expression whose level does not change over time; thus, we have:

$$\frac{d\, C(mature\ mRNA)}{dt} = Kp \times\ C(pre - mRNA) - C(mature\ mRNA) \times Kd = 0$$

$$Kp = \frac{C\ (mature\ mRNA) \times Kd}{C\ (pre - mRNA)} \tag{4}$$

Under *Son* overexpression or knocking down condition (condition 2), if we assume the mature mRNA degradation rate does not change with *Son* OE/KD (*K1*d=*K2*d), then the ratio of splicing rates between basal condition 1 and *Son* OE/KD condition 2 is given by:

$$\frac{Kp1}{Kp2} = \frac{C1\ (mature\ mRNA) \times C2 (pre - mRNA)}{C1\ (pre - mRNA) \times C2\ (mature\ mRNA)} \tag{5}$$

Gene set enrichment analysis (GSEA)

GSEA was performed with software version 4.1.0. TPM quantification of transcriptome under different drugs or DMSO control was used as input for gene expression. Parameters used for the analysis: 1000 permutations, permutation type: gene set.

Intron retention detection

Intron retention events were detected by iREAD [31]. Intron retention events are selected with default settings T>=20, J>=1, FPKM>=2.

Gene ontology analysis

DAVID (Version 2021) [130] (https://david.ncifcrf.gov) was used to perform Gene Ontology analyses. Briefly, gene names were first converted to DAVID-recognizable IDs using Gene Accession Conversion Tool. The updated gene list was then subject to GO analysis using all Homo Sapiens as background and with Functional Annotation Chart function. GO_BP_DIRECT, KEGG_PATHWAY or UP_KW_BIOLOGICAL_PROCESS was used as GO categories. Only GO terms with a p value less than 0.05 were included for further analysis.

Motif analysis

Motif analysis was performed with the SeqPos motif tool (version 0.590) [131] embedded in Galaxy Cistrome using all motifs within the homo sapiens reference genome hg19 as background. LISA analysis was performed using webtool (http://lisa.cistrome.org/).

Statistical Analysis

Data was analyzed and presented with GraphPad Prism software. Plots show individual data points and bars at the mean and ± the standard error of the mean (SEM). Individual tests used were provided at the end of each figure legend.

Author contributions

Conceptualization, Y.C., X.C., and B.Z.; Methodology, W.D., B.B.C., S.L., S.P., Y.C., X.C., and B.Z.; Investigation, W.D., Y.T., S.K., S.Z., M.C., R.K.A., M.S., Y.N., M.Y., M.B.L., D.C., E.I., C.D., H.W., S.L., S.P., B.B.C., Y.C., X.,C, and B.Z.; Writing – Original Draft, W.D., Y.C., X.C., and B.Z.; Writing – Review & Editing, all authors; Funding Acquisition, W.D., B.B.C., Y.C., X.C., and B.Z.; Resources, B.B.C. S.P., Y.C., X.C. and B.Z; Supervision, Y.C., X.C., and B.Z.

Acknowledgements

We would like to thank Drs. Yvonne Eisele, Yuan Liu and Toren Finkel (University of Pittsburgh School of Medicine, Pittsburgh, PA, U.S.A.) for their technical assistance and/or comments on the manuscript. We thank Dr. Krzysztof Palczewski who generously shared the 1D4 anti-rhodopsin antibody. W.D. was supported by grant T32 HL082610 through the National Institutes of Health (NIH), the Diana Jacobs Kalman/AFAR Scholarship for Research in the Biology of Aging through the American Federation for Aging Research, and fellowship F31 AG080998. B.B.C. was supported by grant 1R35HL139860 through the NIH. Y.C was supported by the R01 EY030991. X.C. was supported by the National Institutes of Health grants R01AG074273 and R01AG078185. B. Zhu was supported by grants 1DP2GM140924 and 1R21AG071893 through the NIH, and a grant from Richard King Mellon foundation. This research was supported in part by the University of Pittsburgh Center for Research Computing through the resources provided. Specifically, this work used the HTC cluster, which is supported by NIH award number S10OD028483. This research project was supported in part by the Pittsburgh Liver Research Centre supported by NIH/NIDDK Digestive Disease Research Core Center grant P30DK120531, the Ophthalmology and Visual Sciences Research Center core grant P30 EY08098, the Eye and Ear Foundation of Pittsburgh and an unrestricted grant from Research to Prevent Blindness.

Declaration of interests

B.B.C. is Co-founder of Koutif Therapeutic Inc., Co-founder and VP of Drug Discovery for Generian Pharmaceuticals, and Co-founder and C.S.O. of Coloma Therapeutics Inc..

Data availability

All raw and processed sequencing data generated in this study have been submitted to the NCBI Gene Expression Omnibus (GEO; http://www.ncbi.nlm.nih.gov/geo/) under accession numbers GSE224275. The mass spectrometry proteomics data have been deposited to the ProteomeXchange Consortium via the PRIDE partner repository with the dataset identifier PXD050371. All data needed to evaluate the conclusions in the paper are present in the paper and/or the Supplementary Materials.

References and Notes

1. Gestwicki JE, Garza D. Protein quality control in neurodegenerative disease. *Prog Mol Biol Transl Sci* **107**, 327-353 (2012).

2. Golde TE, Borchelt DR, Giasson BI, Lewis J. Thinking laterally about neurodegenerative proteinopathies. *J Clin Invest* **123**, 1847-1855 (2013).

3. Zhu B*, et al.* A Cell-Autonomous Mammalian 12 hr Clock Coordinates Metabolic and Stress Rhythms. *Cell Metab* **25**, 1305-1319 e1309 (2017).

4. Zhu B, Dacso CC, O'Malley BW. Unveiling "Musica Universalis" of the Cell: A Brief History of Biological 12-Hour Rhythms. *J Endocr Soc* **2**, 727-752 (2018).

5. Meng H*, et al.* XBP1 links the 12-hour clock to NAFLD and regulation of membrane fluidity and lipid homeostasis. *Nature Communications* **11**, 6215 (2020).

6. Pan Y*, et al.* 12-h clock regulation of genetic information flow by XBP1s. *PLOS Biology* **18**, e3000580 (2020).

7. Ballance H, Zhu B. Revealing the hidden reality of the mammalian 12-h ultradian rhythms. *Cellular and Molecular Life Sciences*, (2021).

8. Asher G, Zhu B. Beyond circadian rhythms: Emerging roles of ultradian rhythms in control of liver functions. *Hepatology* **n/a**, (2022).

9. Dion W*, et al.* Four-dimensional nuclear speckle phase separation dynamics regulate proteostasis. *Science Advances* **8**, eabl4150 (2022).

10. Meng H*, et al.* Defining the mammalian coactivation of hepatic 12-h clock and lipid metabolism. *Cell Reports* **38**, 110491 (2022).

11. Scott MR*, et al.* Twelve-hour rhythms in transcript expression within the human dorsolateral prefrontal cortex are altered in schizophrenia. *PLOS Biology* **21**, e3001688 (2023).

12. Zhu B*, et al.* Evidence for conservation of a primordial 12-hour ultradian gene program in humans. *bioRxiv*, 2023.2005.2002.539021 (2023).

13. Zhu B, Liu S. Preservation of ~12-h ultradian rhythms of gene expression of mRNA and protein metabolism in the absence of canonical circadian clock. *Frontiers in Physiology* **14**, (2023).

14. Spector DL, Lamond AI. Nuclear speckles. *Cold Spring Harb Perspect Biol* **3**, (2011).

15. Hasenson SE, Shav-Tal Y. Speculating on the Roles of Nuclear Speckles: How RNA-Protein Nuclear Assemblies Affect Gene Expression. *Bioessays* **42**, e2000104 (2020).

16. Liao SE, Regev O. Splicing at the phase-separated nuclear speckle interface: a model. *Nucleic Acids Research* **49**, 636-645 (2020).

17. Alexander KA*, et al.* Nuclear speckles regulate HIF-2α programs and correlate with patient survival in kidney cancer. *bioRxiv*, 2023.2009.2014.557228 (2023).

18. Alexander KA*, et al.* p53 mediates target gene association with nuclear speckles for amplified RNA expression. *Mol Cell* **81**, 1666-1681 e1666 (2021).

19. Dion W*, et al.* Four-dimensional nuclear speckle phase separation dynamics regulate proteostasis. *Science Advances* **8**, eabl4150 (2022).

20. Jia M*, et al.* Transcriptional changes of the aging lung. *Aging Cell* **22**, e13969 (2023).

21. Chavez A*, et al.* Comparison of Cas9 activators in multiple species. *Nature methods* **13**, 563-567 (2016).

22. Qin Q*, et al.* Lisa: inferring transcriptional regulators through integrative modeling of public chromatin accessibility and ChIP-seq data. *Genome Biology* **21**, 32 (2020).

23. Cretenet G, Le Clech M, Gachon F. Circadian clock-coordinated 12 Hr period rhythmic activation of the IRE1alpha pathway controls lipid metabolism in mouse liver. *Cell Metab* **11**, 47-57 (2010).

24. Pocaterra A, Romani P, Dupont S. YAP/TAZ functions and their regulation at a glance. *Journal of Cell Science* **133**, jcs230425 (2020).

25. Panciera T, Azzolin L, Cordenonsi M, Piccolo S. Mechanobiology of YAP and TAZ in physiology and disease. *Nature Reviews Molecular Cell Biology* **18**, 758-770 (2017).

26. Piccolo S, Dupont S, Cordenonsi M. The Biology of YAP/TAZ: Hippo Signaling and Beyond. *Physiological Reviews* **94**, 1287-1312 (2014).

27. Reich S*, et al.* A multi-omics analysis reveals the unfolded protein response regulon and stress-induced resistance to folate-based antimetabolites. *Nature Communications* **11**, 2936 (2020).

28. Lu X, Ng H-H, Bubulya PA. The role of SON in splicing, development, and disease. *Wiley Interdiscip Rev RNA* **5**, 637-646 (2014).

29. Ahn EY*, et al.* SON controls cell-cycle progression by coordinated regulation of RNA splicing. *Mol Cell* **42**, 185-198 (2011).

30. Kim J-H*, et al.* SON drives oncogenic RNA splicing in glioblastoma by regulating PTBP1/PTBP2 switching and RBFOX2 activity. *Nature Communications* **12**, 5551 (2021).

31. Li H-D, Funk CC, Price ND. iREAD: a tool for intron retention detection from RNA-seq data. *BMC Genomics* **21**, 128 (2020).

32. Sureau A, Gattoni R, Dooghe Y, Stévenin J, Soret J. SC35 autoregulates its expression by promoting splicing events that destabilize its mRNAs. *Embo j* **20**, 1785-1796 (2001).

33. Ding F, Su CJ, Edmonds KK, Liang G, Elowitz MB. Dynamics and functional roles of splicing factor autoregulation. *Cell Rep* **39**, 110985 (2022).

34. Grandjean JMD*, et al.* Pharmacologic IRE1/XBP1s activation confers targeted ER proteostasis reprogramming. *Nat Chem Biol* **16**, 1052-1061 (2020).

35. Madhavan A*, et al.* Pharmacologic IRE1/XBP1s activation promotes systemic adaptive remodeling in obesity. *Nature Communications* **13**, 608 (2022).

36. Grandjean JMD, Wiseman RL. Small molecule strategies to harness the unfolded protein response: where do we go from here? *Journal of Biological Chemistry* **295**, 15692-15711 (2020).

37. Schor IE*, et al.* Perturbation of chromatin structure globally affects localization and recruitment of splicing factors. *PloS one* **7**, e48084 (2012).

38. Subramanian A*, et al.* Gene set enrichment analysis: A knowledge-based approach for interpreting genome-wide expression profiles. *Proceedings of the National Academy of Sciences* **102**, 15545-15550 (2005).

39. Molina DM*, et al.* Monitoring Drug Target Engagement in Cells and Tissues Using the Cellular Thermal Shift Assay. *Science* **341**, 84-87 (2013).

40. Jafari R*, et al.* The cellular thermal shift assay for evaluating drug target interactions in cells. *Nature Protocols* **9**, 2100-2122 (2014).

41. Ilik İA, Malszycki M, Lübke AK, Schade C, Meierhofer D, Aktaş T. SON and SRRM2 are essential for nuclear speckle formation. *eLife* **9**, e60579 (2020).

42. Fei J*, et al.* Quantitative analysis of multilayer organization of proteins and RNA in nuclear speckles at super resolution. *Journal of Cell Science* **130**, 4180-4192 (2017).

43. Sharma A, Takata H, Shibahara K, Bubulya A, Bubulya PA. Son is essential for nuclear speckle organization and cell cycle progression. *Mol Biol Cell* **21**, 650-663 (2010).

44. Liao SE, Regev O. Splicing at the phase-separated nuclear speckle interface: a model. *Nucleic Acids Res* **49**, 636-645 (2021).

45. Xu S, Lai SK, Sim DY, Ang WSL, Li HY, Roca X. SRRM2 organizes splicing condensates to regulate alternative splicing. *Nucleic Acids Res* **50**, 8599-8614 (2022).

46. Gouveia B, Kim Y, Shaevitz JW, Petry S, Stone HA, Brangwynne CP. Capillary forces generated by biomolecular condensates. *Nature* **609**, 255-264 (2022).

47. Sabari BR*, et al.* Coactivator condensation at super-enhancers links phase separation and gene control. *Science* **361**, eaar3958 (2018).

48. Chen Z*, et al.* Screening membraneless organelle participants with machine-learning models that integrate multimodal features. *Proceedings of the National Academy of Sciences* **119**, e2115369119 (2022).

49. Romero, Obradovic, Dunker K. Sequence Data Analysis for Long Disordered Regions Prediction in the Calcineurin Family. *Genome Inform Ser Workshop Genome Inform* **8**, 110-124 (1997).

50. Walsh I, Martin AJM, Di Domenico T, Tosatto SCE. ESpritz: accurate and fast prediction of protein disorder. *Bioinformatics* **28**, 503-509 (2011).

51. Santos J, Calero N, Trujillo-Cayado LA, Garcia MC, Muñoz J. Assessing differences between Ostwald ripening and coalescence by rheology, laser diffraction and multiple light scattering. *Colloids and Surfaces B: Biointerfaces* **159**, 405-411 (2017).

52. Dopie J, Sweredoski MJ, Moradian A, Belmont AS. Tyramide signal amplification mass spectrometry (TSA-MS) ratio identifies nuclear speckle proteins. *Journal of Cell Biology* **219**, (2020).

53. Saitoh N, Spahr CS, Patterson SD, Bubulya P, Neuwald AF, Spector DL. Proteomic analysis of interchromatin granule clusters. *Mol Biol Cell* **15**, 3876-3890 (2004).

54. Riback JA*, et al.* Viscoelasticity and advective flow of RNA underlies nucleolar form and function. *Molecular Cell* **83**, 3095-3107.e3099 (2023).

55. Pancholi A*, et al.* RNA polymerase II clusters form in line with liquid phase wetting of chromatin. *bioRxiv*, 2021.2002.2003.429626 (2021).

56. Liu X*, et al.* Time-dependent effect of 1,6-hexanediol on biomolecular condensates and 3D chromatin organization. *Genome Biology* **22**, 230 (2021).

57. Liu J, Rivas FV, Wohlschlegel J, Yates JR, 3rd, Parker R, Hannon GJ. A role for the P-body component GW182 in microRNA function. *Nat Cell Biol* **7**, 1261-1266 (2005).

58. Ravi V, Jain A, Mishra S, Sundaresan NR. Measuring Protein Synthesis in Cultured Cells and Mouse Tissues Using the Non-radioactive SUnSET Assay. *Curr Protoc Mol Biol* **133**, e127 (2020).

59. Pakos-Zebrucka K, Koryga I, Mnich K, Ljujic M, Samali A, Gorman AM. The integrated stress response. *EMBO Rep* **17**, 1374-1395 (2016).

60. Mauvezin C, Neufeld TP. Bafilomycin A1 disrupts autophagic flux by inhibiting both V-ATPase-dependent acidification and Ca-P60A/SERCA-dependent autophagosome-lysosome fusion. *Autophagy* **11**, 1437-1438 (2015).

61. Harada Y, Ishii I, Hatake K, Kasahara T. Pyrvinium pamoate inhibits proliferation of myeloma/erythroleukemia cells by suppressing mitochondrial respiratory complex I and STAT3. *Cancer Letters* **319**, 83-88 (2012).

62. Ishii I, Harada Y, Kasahara T. Reprofiling a classical anthelmintic, pyrvinium pamoate, as an anti-cancer drug targeting mitochondrial respiration. *Frontiers in Oncology* **2**, (2012).

63. Bayer TA. Proteinopathies, a core concept for understanding and ultimately treating degenerative disorders? *Eur Neuropsychopharmacol* **25**, 713-724 (2015).

64. Hartong DT, Berson EL, Dryja TP. Retinitis pigmentosa. *Lancet* **368**, 1795-1809 (2006).

65. Lee E-J, Chan P, Chea L, Kim K, Kaufman RJ, Lin JH. ATF6 is required for efficient rhodopsin clearance and retinal homeostasis in the P23H rho retinitis pigmentosa mouse model. *Scientific Reports* **11**, 16356 (2021).

66. Vats A*, et al.* Nonretinoid chaperones improve rhodopsin homeostasis in a mouse model of retinitis pigmentosa. *JCI Insight* **7**, (2022).

67. Chiang W-C*, et al.* Robust Endoplasmic Reticulum-Associated Degradation of Rhodopsin Precedes Retinal Degeneration. *Molecular Neurobiology* **52**, 679-695 (2015).

68. Chiang W-C, Hiramatsu N, Messah C, Kroeger H, Lin JH. Selective Activation of ATF6 and PERK Endoplasmic Reticulum Stress Signaling Pathways Prevent Mutant Rhodopsin Accumulation. *Investigative Ophthalmology & Visual Science* **53**, 7159-7166 (2012).

69. Lobanova ES*, et al.* Increased proteasomal activity supports photoreceptor survival in inherited retinal degeneration. *Nat Commun* **9**, 1738 (2018).

70. Liu X*, et al.* Pharmacological clearance of misfolded rhodopsin for the treatment of RHO-associated retinitis pigmentosa. *The FASEB Journal* **34**, 10146-10167 (2020).

71. Lee MJ, Lee JH, Rubinsztein DC. Tau degradation: The ubiquitin–proteasome system versus the autophagy-lysosome system. *Progress in Neurobiology* **105**, 49-59 (2013).

72. Limanaqi F, Biagioni F, Gambardella S, Familiari P, Frati A, Fornai F. Promiscuous Roles of Autophagy and Proteasome in Neurodegenerative Proteinopathies. *Int J Mol Sci* **21**, (2020).

73. Samelson AJ*, et al.* CRISPR screens in iPSC-derived neurons reveal principles of tau proteostasis. *bioRxiv*, 2023.2006.2016.545386 (2023).

74. Bravo CP*, et al.* Human iPSC 4R tauopathy model uncovers modifiers of tau propagation. *bioRxiv*, 2023.2006.2019.544278 (2023).

75. Bugiani O*, et al.* Frontotemporal dementia and corticobasal degeneration in a family with a P301S mutation in tau. *Journal of neuropathology and experimental neurology* **58**, 667-677 (1999).

76. Chen X*, et al.* Promoting tau secretion and propagation by hyperactive p300/CBP via autophagy-lysosomal pathway in tauopathy. *Molecular Neurodegeneration* **15**, 2 (2020).

77. Triastuti E*, et al.* Pharmacological inhibition of Hippo pathway, with the novel kinase inhibitor XMU-MP-1, protects the heart against adverse effects during pressure overload. *Br J Pharmacol* **176**, 3956-3971 (2019).

78. Hao X*, et al.* XMU-MP-1 attenuates osteoarthritis via inhibiting cartilage degradation and chondrocyte apoptosis. *Frontiers in Bioengineering and Biotechnology* **10**, (2022).

79. Kastan N*, et al.* Small-molecule inhibition of Lats kinases may promote Yap-dependent proliferation in postmitotic mammalian tissues. *Nature Communications* **12**, 3100 (2021).

80. Qin F, Tian J, Zhou D, Chen L. Mst1 and Mst2 kinases: regulations and diseases. *Cell & Bioscience* **3**, 31 (2013).

81. Arno G*, et al.* Mutations in REEP6 Cause Autosomal-Recessive Retinitis Pigmentosa. *Am J Hum Genet* **99**, 1305-1315 (2016).

82. Pi S*, et al.* Fully automated OCT-based tissue screening system. *Opt Lett* **49**, 4481-4484 (2024).

83. Wittmann CW*, et al.* Tauopathy in <i>Drosophila</i>: Neurodegeneration Without Neurofibrillary Tangles. *Science* **293**, 711-714 (2001).

84. Berger C, Renner S, Lüer K, Technau GM. The commonly used marker ELAV is transiently expressed in neuroblasts and glial cells in the Drosophila embryonic CNS. *Developmental Dynamics* **236**, 3562-3568 (2007).

85. Hirabayashi S, Baranski TJ, Cagan RL. Transformed Drosophila cells evade diet-mediated insulin resistance through wingless signaling. *Cell* **154**, 664-675 (2013).

86. Wang L*, et al.* JNK modifies neuronal metabolism to promote proteostasis and longevity. *Aging Cell* **18**, e12849 (2019).

87. Xu M*, et al.* A systematic integrated analysis of brain expression profiles reveals YAP1 and other prioritized hub genes as important upstream regulators in Alzheimer's disease. *Alzheimers Dement* **14**, 215-229 (2018).

88. Mathys H*, et al.* Single-cell transcriptomic analysis of Alzheimer’s disease. *Nature* **570**, 332-337 (2019).

89. Wang C*, et al.* Scalable Production of iPSC-Derived Human Neurons to Identify Tau-Lowering Compounds by High-Content Screening. *Stem Cell Reports* **9**, 1221-1233 (2017).

90. Wu R*, et al.* Disruption of nuclear speckle integrity dysregulates RNA splicing in C9ORF72-FTD/ALS. *Neuron*, (2024).

91. Lester E*, et al.* Tau aggregates are RNA-protein assemblies that mislocalize multiple nuclear speckle components. *Neuron* **109**, 1675-1691.e1679 (2021).

92. McMillan PJ*, et al.* Pathological tau drives ectopic nuclear speckle scaffold protein SRRM2 accumulation in neuron cytoplasm in Alzheimer's disease. *Acta Neuropathologica Communications* **9**, 117 (2021).

93. Mordes D*, et al.* Pre-mRNA splicing and retinitis pigmentosa. *Mol Vis* **12**, 1259-1271 (2006).

94. Lester E*, et al.* Tau aggregates are RNA-protein assemblies that mislocalize multiple nuclear speckle components. *Neuron* **109**, 1675-1691 e1679 (2021).

95. Tracy TE*, et al.* Tau interactome maps synaptic and mitochondrial processes associated with neurodegeneration. *Cell* **185**, 712-728.e714 (2022).

96. Hsieh YC*, et al.* Tau-Mediated Disruption of the Spliceosome Triggers Cryptic RNA Splicing and Neurodegeneration in Alzheimer's Disease. *Cell Rep* **29**, 301-316 e310 (2019).

97. Wheeler RJ. Therapeutics-how to treat phase separation-associated diseases. *Emerg Top Life Sci* **4**, 307-318 (2020).

98. Conti BA, Oppikofer M. Biomolecular condensates: new opportunities for drug discovery and RNA therapeutics. *Trends in Pharmacological Sciences* **43**, 820-837 (2022).

99. Kilgore HR*, et al.* Distinct chemical environments in biomolecular condensates. *Nature Chemical Biology*, (2023).

100. Schultz CW, Nevler A. Pyrvinium Pamoate: Past, Present, and Future as an Anti-Cancer Drug. *Biomedicines* **10**, 3249 (2022).

101. Jawerth LM*, et al.* Salt-Dependent Rheology and Surface Tension of Protein Condensates Using Optical Traps. *Physical Review Letters* **121**, 258101 (2018).

102. Spruijt E, Sprakel J, Cohen Stuart MA, van der Gucht J. Interfacial tension between a complex coacervate phase and its coexisting aqueous phase. *Soft Matter* **6**, 172-178 (2010).

103. Cai D, Sukenik S, Feliciano D, Gruebele M, Lippincott-Schwartz J. Phase Separation of YAP Reprograms Cells for Long-term YAP Target Gene Expression. *bioRxiv*, 438416 (2018).

104. Yang S*, et al.* Bip-Yorkie interaction determines oncogenic and tumor-suppressive roles of Ire1/Xbp1s activation. *Proceedings of the National Academy of Sciences* **119**, e2202133119 (2022).

105. Rivera-Reyes A*, et al.* YAP1 enhances NF-κB-dependent and independent effects on clock-mediated unfolded protein responses and autophagy in sarcoma. *Cell Death Dis* **9**, 1108 (2018).

106. Min Y*, et al.* Cross species systems biology discovers glial DDR2, STOM, and KANK2 as therapeutic targets in progressive supranuclear palsy. *Nature Communications* **14**, 6801 (2023).

107. Vallazza-Deschamps G*, et al.* Excessive activation of cyclic nucleotide-gated channels contributes to neuronal degeneration of photoreceptors. *Eur J Neurosci* **22**, 1013-1022 (2005).

108. Vats A*, et al.* Nonretinoid chaperones improve rhodopsin homeostasis in a mouse model of retinitis pigmentosa. *JCI Insight* **7**, (2022).

109. Pi S*, et al.* Retinal capillary oximetry with visible light optical coherence tomography. *Proceedings of the National Academy of Sciences of the United States of America* **117**, 11658-11666 (2020).

110. Fanning S, Selkoe D, Dettmer U. Parkinson's disease: proteinopathy or lipidopathy? *NPJ Parkinsons Dis* **6**, 3 (2020).

111. Wulansari N*, et al.* Neurodevelopmental defects and neurodegenerative phenotypes in human brain organoids carrying Parkinson's disease-linked DNAJC6 mutations. *Sci Adv* **7**, (2021).

112. Dion W*, et al.* Four-dimensional nuclear speckle phase separation dynamics regulate proteostasis. *Sci Adv* **8**, eabl4150 (2022).

113. Dupont S*, et al.* Role of YAP/TAZ in mechanotransduction. *Nature* **474**, 179-183 (2011).

114. Stirling DR, Swain-Bowden MJ, Lucas AM, Carpenter AE, Cimini BA, Goodman A. CellProfiler 4: improvements in speed, utility and usability. *BMC bioinformatics* **22**, 1-11 (2021).

115. Liu X*, et al.* Pharmacological clearance of misfolded rhodopsin for the treatment of RHO-associated retinitis pigmentosa. *Faseb j* **34**, 10146-10167 (2020).

116. Schneider CA, Rasband WS, Eliceiri KW. NIH Image to ImageJ: 25 years of image analysis. *Nature methods* **9**, 671-675 (2012).

117. Zhu B*, et al.* Coactivator-Dependent Oscillation of Chromatin Accessibility Dictates Circadian Gene Amplitude via REV-ERB Loading. *Mol Cell* **60**, 769-783 (2015).

118. Zhu B*, et al.* A Cell-Autonomous Mammalian 12 hr Clock Coordinates Metabolic and Stress Rhythms. *Cell Metabolism* **25**, 1305-1319.e1309 (2017).

119. Zhu B*, et al.* Peroxisome proliferator-activated receptor beta/delta cross talks with E2F and attenuates mitosis in HRAS-expressing cells. *Mol Cell Biol* **32**, 2065-2082 (2012).

120. Bolger AM, Lohse M, Usadel B. Trimmomatic: a flexible trimmer for Illumina sequence data. *Bioinformatics* **30**, 2114-2120 (2014).

121. Kim D, Langmead B, Salzberg SL. HISAT: a fast spliced aligner with low memory requirements. *Nat Methods* **12**, 357-360 (2015).

122. Quinlan AR, Hall IM. BEDTools: a flexible suite of utilities for comparing genomic features. *Bioinformatics* **26**, 841-842 (2010).

123. Blankenberg D*, et al.* Galaxy: A Web-Based Genome Analysis Tool for Experimentalists. *Current Protocols in Molecular Biology* **89**, 19.10.11-19.10.21 (2010).

124. Krueger F. Trim Galore.) (2021).

125. Patro R, Duggal G, Love MI, Irizarry RA, Kingsford C. Salmon provides fast and bias-aware quantification of transcript expression. *Nature methods* **14**, 417-419 (2017).

126. Guo W*, et al.* 3D RNA-seq: a powerful and flexible tool for rapid and accurate differential expression and alternative splicing analysis of RNA-seq data for biologists. *RNA biology* **18**, 1574-1587 (2021).

127. Langmead B, Salzberg SL. Fast gapped-read alignment with Bowtie 2. *Nat Methods* **9**, 357-359 (2012).

128. Li B, Dewey CN. RSEM: accurate transcript quantification from RNA-Seq data with or without a reference genome. *BMC Bioinformatics* **12**, 323 (2011).

129. Robinson MD, McCarthy DJ, Smyth GK. edgeR: a Bioconductor package for differential expression analysis of digital gene expression data. *Bioinformatics* **26**, 139-140 (2010).

130. Huang da W, Sherman BT, Lempicki RA. Systematic and integrative analysis of large gene lists using DAVID bioinformatics resources. *Nat Protoc* **4**, 44-57 (2009).

131. He HH*, et al.* Nucleosome dynamics define transcriptional enhancers. *Nature Genetics* **42**, 343-347 (2010).

132. Zhang MJ, Pisco AO, Darmanis S, Zou J. Mouse aging cell atlas analysis reveals global and cell type-specific aging signatures. *Elife* **10**, (2021).

133. A single-cell transcriptomic atlas characterizes ageing tissues in the mouse. *Nature* **583**, 590-595 (2020).

134. Jiang J, Wang C, Qi R, Fu H, Ma Q. scREAD: A Single-Cell RNA-Seq Database for Alzheimer's Disease. *iScience* **23**, 101769 (2020).

Fig. legends

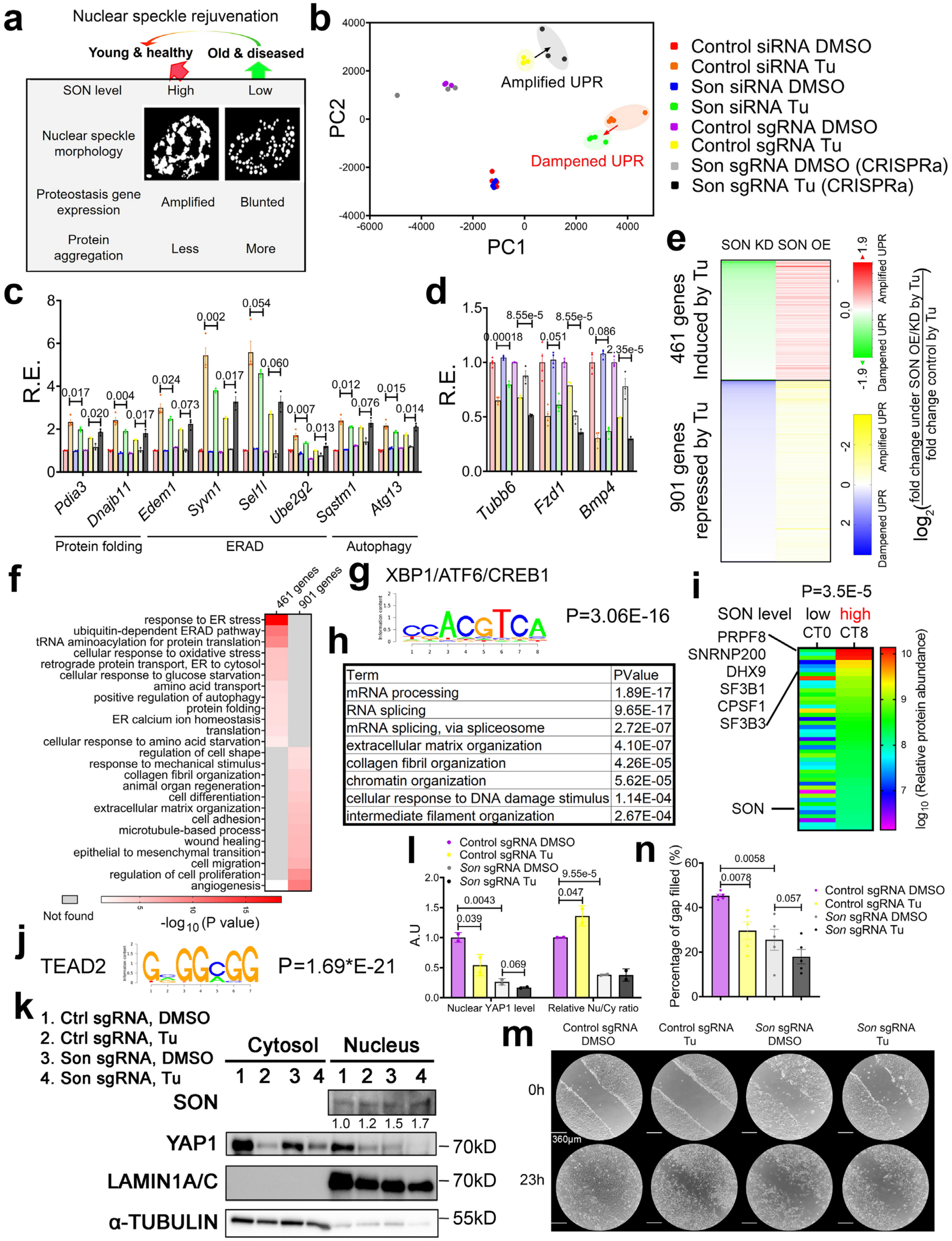

Term	PValue
mRNA processing	1.89E-17
RNA splicing	9.65E-17
mRNA splicing, via spliceosome	2.72E-07
extracellular matrix organization	4.10E-07
collagen fibril organization	4.26E-05
chromatin organization	5.62E-05
cellular response to DNA damage stimulus	1.14E-04
intermediate filament organization	2.67E-04

Fig. 1. Genetic rejuvenation of nuclear speckle transcriptionally reprograms global proteostasis and YAP1 signaling in an opposing manner. (**a**) The diagram of the approach of

nuclear speckle rejuvenation to alleviate proteinopathy. (**b**) PCA of global transcriptional response to Tu in the presence of SON OE (via CRISPRa) or KD (via siRNA). (**c, d**) Relative expression (R.E.) of representative proteostasis genes (**c**) and YAP1 target genes (**d**) in response to Tu in the presence of SON OE/KD (n=4 for SON KD, and n=3 for SON OE). (**e**) Heat map of relative fold change of gene expression by Tu in SON OE/KD cells compared to control cells. Only those genes with at least 1.4-fold induction by Tu ($\log_2 > 0.5$) with a p value smaller than 0.05 in control condition are included. Among these genes are 461 genes whose induction by Tu are further amplified by SON OE (induced more) and dampened (induced less) *by* SON KD; and 901 genes whose repression by Tu are further amplified by *Son* OE (repressed further) and dampened (repressed less) by SON KD. (**f**) GO analysis of those 461 and 901 genes showing enriched KEGG pathways. (**g**) Enriched XBP1s binding motif ACGTCA on the promoters of 461 genes. (**h**) Top enriched GO terms for top 500 most abundant proteins that are detected in hepatic XBP1s interactome at CT8, as previously reported [10]. (**i**) Heatmap showing relative abundance of 45 proteins involved in mRNA splicing and processing within the XBP1s interactome at CT0 and CT8, respectively. (**j**) Enriched TEAD2 binding motif GGCGG on the promoters of 901 genes. Western blot (**k**) and quantification (**l**) of nuclear and cytosolic level of YAP1 in control and SON OE cells in response to Tu (n=2). Scratch assay with representative images (**m**) and quantification (**n**) of cell migration rate in control and SON OE cells in response to Tu (n=5). All data mean ± standard error of the mean (S.E.M.). Statistical tests used: unpaired one-tailed Student's t-test for c, d, l, and n. Paired one-tailed Student's t-test for i.

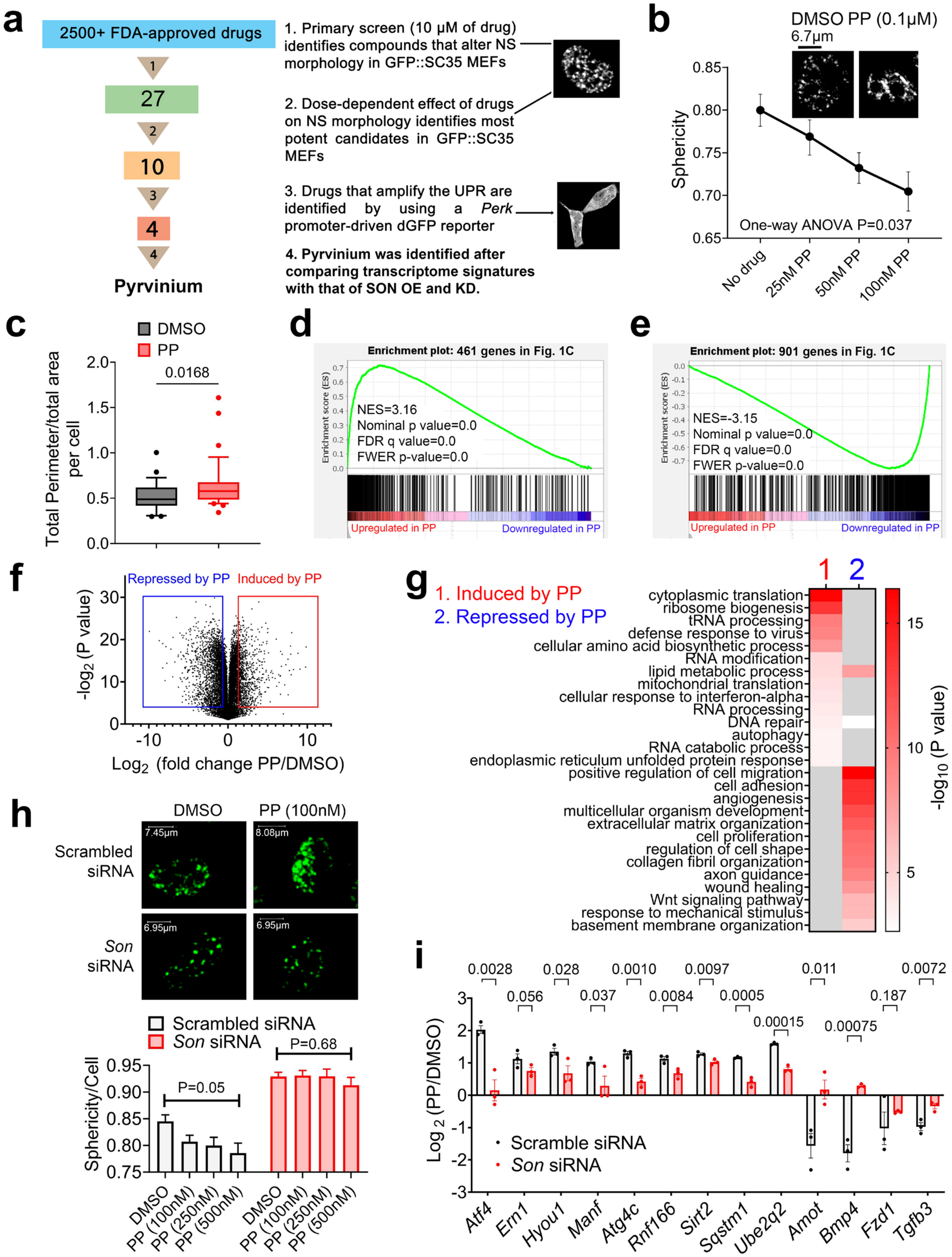

Fig. 2. HTS identifies pyrvinium as a SON-dependent nuclear speckle rejuvenator. (**a**) Workflow detailing our initial drug screen and subsequent steps to identify compounds that affect the nuclear speckle morphology in a dose-dependent manner and amplifies the UPR. (**b**) Dose-

dependent effect on nuclear speckles morphology by PP, with a representative image of nuclear speckles under DMSO or 0.1μM of PP (n=25~57). (**c**) Quantification of total area-normalized perimeter of nuclear speckles in control and 1μM PP condition per cell (n=26 for DMSO and n=35 for PP). (**d**) GSEA analysis showing a similar transcriptome signature between PP-upregulated genes and 461 genes further amplified by SON OE during ER stress. (**e**) GSEA analysis showing a similar transcriptome signature between PP-downregulated genes and 901 genes further blunted by SON OE during ER stress. (**f**) Volcano plot showing fold change by PP versus log transformed p values. Genes induced or repressed by at least 1.41-fold with a p value smaller than 0.05 are boxed. (**g**) GO analysis of differentially expressed genes by PP. (**h**) Representative images and quantification of sphericity of GFP signal from GFP::SRSF2 MEFs with scrambled or *Son* siRNA treated with DMSO or increasing concentration of PP for 25 hours (n=31~81). (**i**) Log_2 normalized fold change in response to PP treatment (0.3 μm) for 24 hours in control and SON KD MEFs with p values shown for one tailed t-test (n=3). All data mean ± S.E.M. Statistical tests used: unpaired one-tailed Student's t-test for c and i. Ordinary one-way ANOVA for b and h.

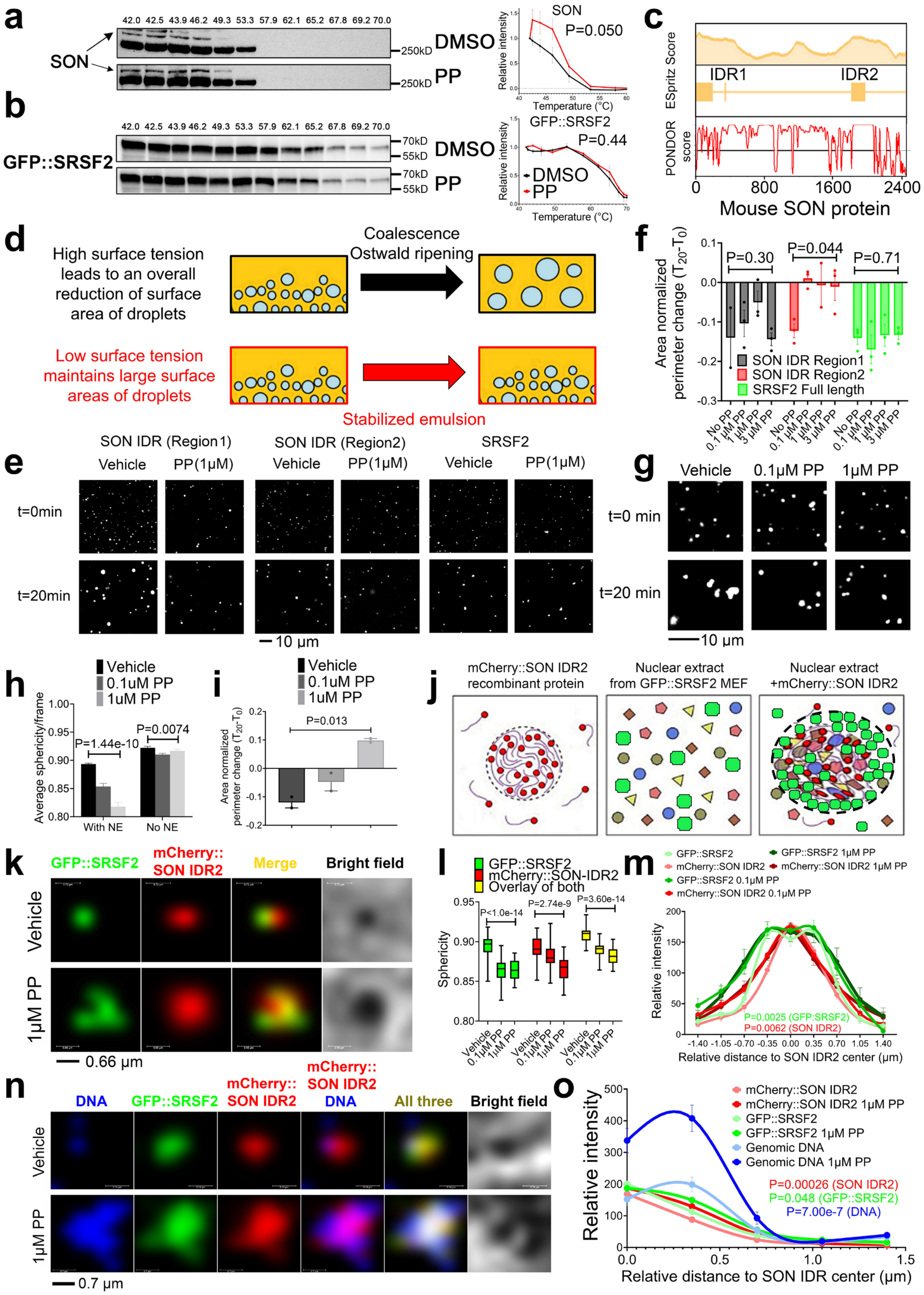
a
SON
42.0 42.5 43.9 46.2 49.3 53.3 57.9 62.1 65.2 67.8 69.2 70.0
250kD DMSO
250kD PP
SON
P=0.050
Relative intensity
Temperature (°C)
b
GFP::SRSF2
70kD
55kD DMSO
70kD
55kD PP
GFP::SRSF2
P=0.44
DMSO
PP
c
ESpritz Score
IDR1
IDR2
PONDOR score
0 800 1600 2400
Mouse SON protein
d
High surface tension leads to an overall reduction of surface area of droplets
Coalescence
Ostwald ripening
Low surface tension maintains large surface areas of droplets
Stabilized emulsion
f
Area normalized perimeter change (T_{20}-T_0)
P=0.30
P=0.044
P=0.71
SON IDR Region1
SON IDR Region2
SRSF2 Full length
No PP
0.1 μM PP
1 μM PP
5 μM PP
e
SON IDR (Region1)
SON IDR (Region2)
SRSF2
Vehicle
PP(1μM)
t=0min
t=20min
10 μm
g
Vehicle
0.1μM PP
1μM PP
t=0 min
t=20 min
10 μm
h
Vehicle
0.1uM PP
1uM PP
Average sphericity/frame
P=1.44e-10
P=0.0074
With NE
No NE
i
Vehicle
0.1uM PP
1uM PP
Area normalized perimeter change (T_{20}-T_0)
P=0.013
j
mCherry::SON IDR2 recombinant protein
Nuclear extract from GFP::SRSF2 MEF
Nuclear extract +mCherry::SON IDR2
k
GFP::SRSF2
mCherry:: SON IDR2
Merge
Bright field
Vehicle
1μM PP
0.66 μm
l
GFP::SRSF2
mCherry::SON-IDR2
Overlay of both
Sphericity
P<1.0e-14
P=2.74e-9
P=3.60e-14
Vehicle
0.1μM PP
1μM PP
m
GFP::SRSF2
mCherry::SON IDR2
GFP::SRSF2 0.1μM PP
mCherry::SON IDR2 0.1μM PP
GFP::SRSF2 1μM PP
mCherry::SON IDR2 1μM PP
Relative intensity
P=0.0025 (GFP:SRSF2)
P=0.0062 (SON IDR2)
Relative distance to SON IDR2 center (μm)
n
DNA
GFP::SRSF2
mCherry:: SON IDR2
mCherry:: SON IDR2 DNA
All three
Bright field
Vehicle
1μM PP
0.7 μm
o
mCherry::SON IDR2
mCherry::SON IDR2 1μM PP
GFP::SRSF2
GFP::SRSF2 1μM PP
Genomic DNA
Genomic DNA 1μM PP
P=0.00026 (SON IDR2)
P=0.048 (GFP::SRSF2)
P=7.00e-7 (DNA)
Relative intensity
Relative distance to SON IDR center (μm)

Fig. 3. PP targets SON to reduce the interfacial tension of nuclear speckles. CETSA of SON (**a**) and GFP::SRSF2 (**b**) with 3μM PP. Both representative blot and quantification from independent replicates are shown. (SON: n=6 for DMSO and n=5 for PP; GFP::SRSF2: n=3 for both DMSO and PP). (**c**) Computational prediction of IDR in mouse SON. (**d**) Diagram illustrating how surface tension influences droplets coalescence kinetics. (**e, f**) Representative images of droplet formation assay with different recombinant proteins (**e**) and quantification (**f**) of area-normalized perimeter changes in the time span of 20 minutes with 125mM NaCl (n=2~3). (**g-i**) Representative images of droplet formation with NE-supplemented SON IDR2 with increasing concentration of PP (**g**) and quantification of sphericity (n=12 for with NE and n=42 for without NE) (**h**) and area-normalized perimeter changes (n=2) (**i**) in the time span of 20 minutes. (**j-m**) Diagram of droplet formation assay where SON IDR2 is expected to compartmentalize splicing factors, including GFP::SRSF2 into the nuclear speckle-like condensates. GFP::SRSF2 is expected to exhibit a broader spatial distribution than the SON IDR2 core (**j**). Representative images (**k**) and quantification of sphericity (**l**) and spatial distribution of mCherry::SON IDR2 and GFP::SRSF2 (**m**). (**n, o**) Mouse genomic DNA was further added to the solution. Representative images (**n**) and quantification (**o**) of spatial distribution of mCherry::SON IDR2, GFP::SRSF2 and DNA. All data mean ± S.E.M. Statistical tests used: mixed-effects analysis for a, b and m. Ordinary one-way ANOVA for f, h, I and l. Two-way RM ANOVA for o.

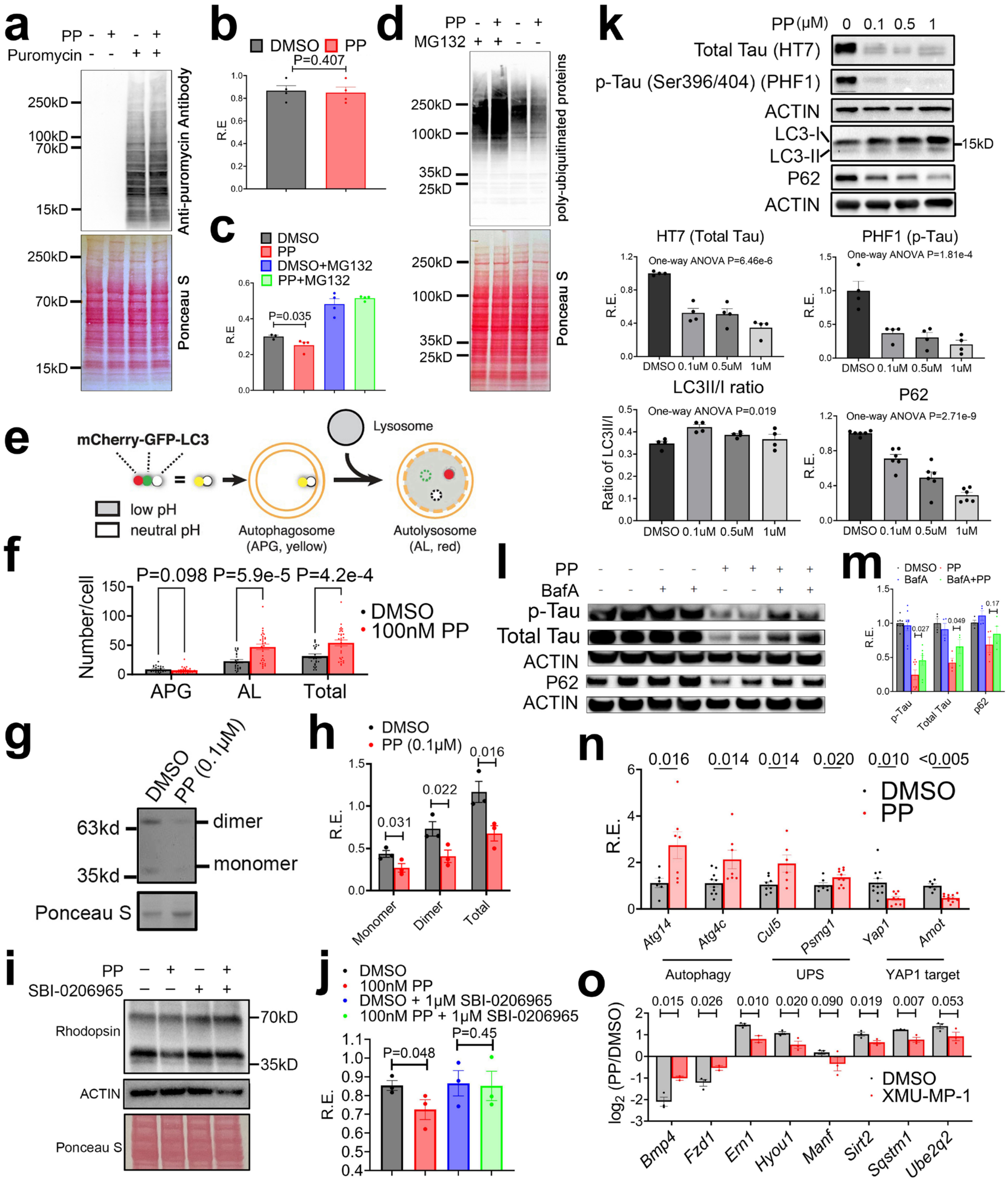

Fig. 4. PP reduces pathological Tau and Rhodopsin level by boosting autophagy and UPS activity. (**a-d**) MEFs were treated with DMSO or 0.1μM PP for ~24 hours and then co-treated with or without puromycin (10 μg/mL for 30 minutes), or MG132 (10μM for 110 minutes) (n=4 for all samples). Western blot and quantification of puromycin-incorporated proteins (**a, b**), and poly-ubiquitinated protein (**c, d**). (**e, f**) MEFs were treated with DMSO or 0.1μM PP for ~24 hours and autophagic flux was measured via a mCherry::GFP::LC3 fusion protein reporter. Chimeric proteins comprising LC3B fused with both GFP and mCherry offer a method to track autophagic flux. Autophagosomes (APG) marked by mCherry::GFP::LC3 exhibit both mCherry and GFP

signals. Following fusion with lysosome to form autolysosome (AL), GFP signals diminish significantly in the acidic environment, while mCherry signals remain relatively stable. (**e**). Quantification of the number of APG, AL and total vesicles (**f**). n=23 for DMSO and 29 for PP. (**g, h**) NIH3T3 RHO^{P23H} cells were treated with 0.1µM PP for 24 hours and Western blot (**g**) and quantification (**h**) of RHO^{P23H} level (n=3). (**i, j**) 0.1µM PP-treated NIH3T3 RHO^{P23H} cells were co-treated with or without 1µM SBI-0206965 for 24 hours. Western blot (**i**) and quantification (**j**) of RHO^{P23H} level (n=3). (**k-m**) Tau (P301S)-expressing primary neurons were treated with increasing concentration of PP for 24 hours, and western blot and quantification of different proteins (n=4 for HT7, PHF1 and LC3, and n=6 for P62) (**k**) or treated with 0.1µM PP for 12h hours in the presence or absence of BafA (50nM) in the last hour and western blot (**l**) and quantification (n=4 for total Tau and P62 and n=8 for p-Tau) (**m**) of different proteins. (**n**) Tau P301S-expressing neurons were treated with DMSO or 0.1µM PP for 12 hours and qPCR of selective proteostasis and YAP1 target genes (n=6~11). (**o**) MEFs were treated with DMSO, PP (1µM), XMU-MP-1 (1µM) or XMU-MP-1+PP for 24 hours, and qPCR of protein quality control and YAP1s output gene expression quantified as log transformed fold change under DMSO or XMU-MP-1 condition by PP (n=3). All data mean ± S.E.M. Statistical tests used: unpaired one-tailed Student's t-test for b, c, f, h, j, m, n and o. Ordinary one-way ANOVA for k.

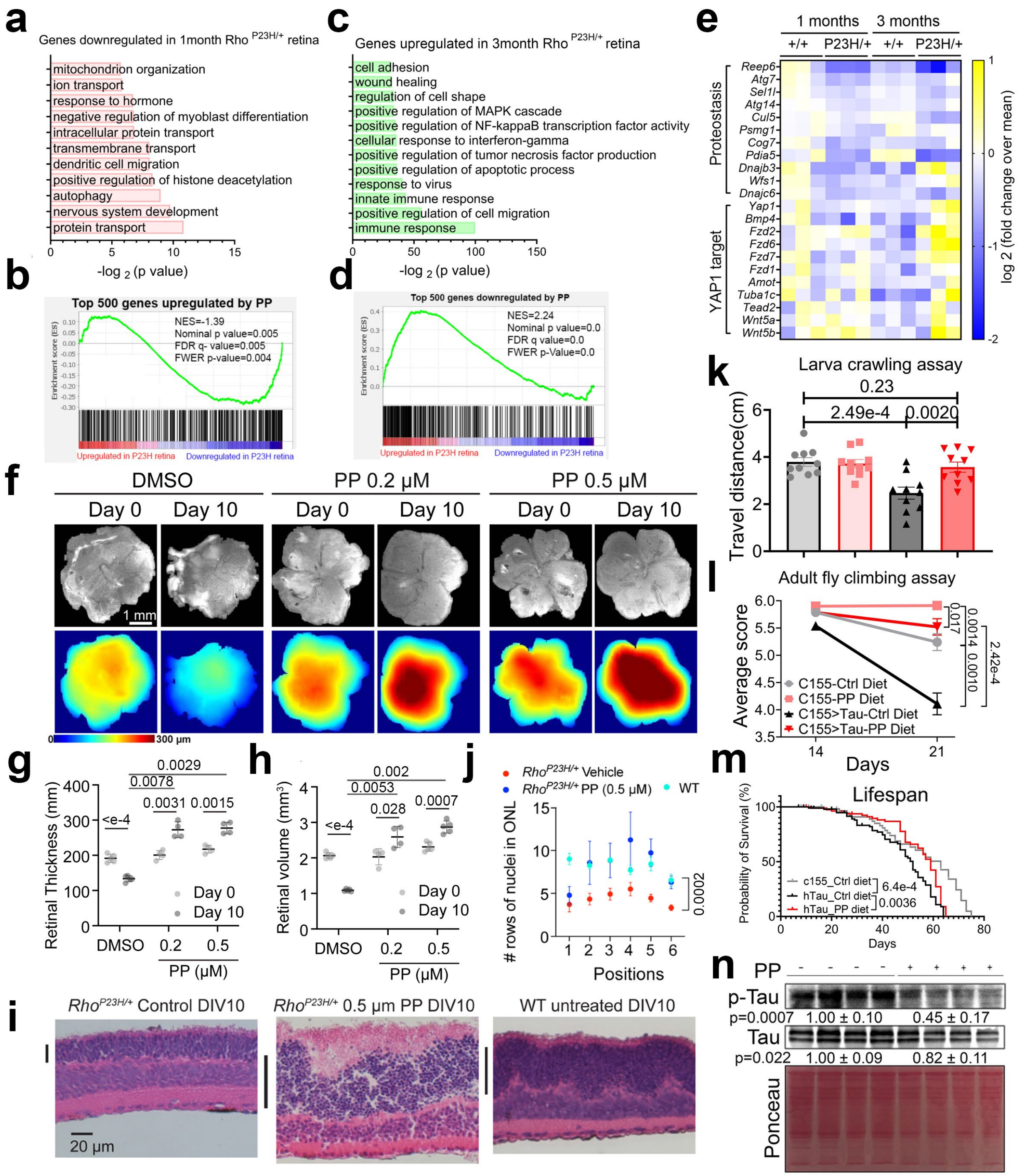

Fig. 5. PP alleviates proteinopathies in preclinical models. (**a-e**) RNA-seq was performed in the retina of 1 and 3 months-old wild-type and Rho $^{P23H/+}$ mice. GO of differentially expressed genes (DEG) (FDR<0.1) (**a, c**) and GSEA comparing these DEG with that of PP (**b, d**). Heatmap of selective genes (**e**). (**f-j**) Retina explants isolated either from *Rho*$^{P23H/+}$ mice P15 and cultured with PP or DMSO vehicle control or from wild-type mice cultured for 10 days *ex vivo*. (**f**) The morphology retinae were imaged and scanned before (Day 0) and after treatment (Day 10) by a webcam (top) and visible light optical coherence tomography (vis-OCT) with tissue thickness

shown as a heatmap with a color legend indicating thickness from 0-300 μm (bottom). Scale, 1 mm. (**g**) and (**h**) are bar plots of retinal thickness and volume, respectively, measured from the vis-OCT scanning data. n=4~5. (**i**) Representative retinal histology images of the retina explants cultured for 10 days with black bars showing the outer nuclear layer (ONL). (**j**) The nuclei count in the outer nuclei layer (ONL) along six horizontal positions at peripheral-central-peripheral positions across each cross-section in (**i**). n=3-4. (**k-n**) Male C155>UAS-hTau1.13 and C155 flies were fed with either standard diet or diet supplemented with 25μM PP. Quantification of distance travelled from larval crawling assay (n=10) (**k**), climbing index score from adult fly climbing assay at 14 days and 21 days (n=5) (**l**) of age, and lifespan assay (**m**) (n=32 for C155-Ctrl, n=65 for hTau-Ctrl and n=44 for hTau-PP). (**n**) Western blot and quantification of p-Tau (AT8 antibody) and total Tau (DAKO antibody) level in 21 days C155>UAS-hTau1.13 flies fed with control or PP diet n=4. All data mean ± S.E.M. Statistical tests used: two-way ANOVA and Turkey multiple comparison for g and h, two-way ANOVA for j, unpaired one-tailed Student's t-test for k, l (day 21) and n. Log-rank (Mantel-Cox) test for m.

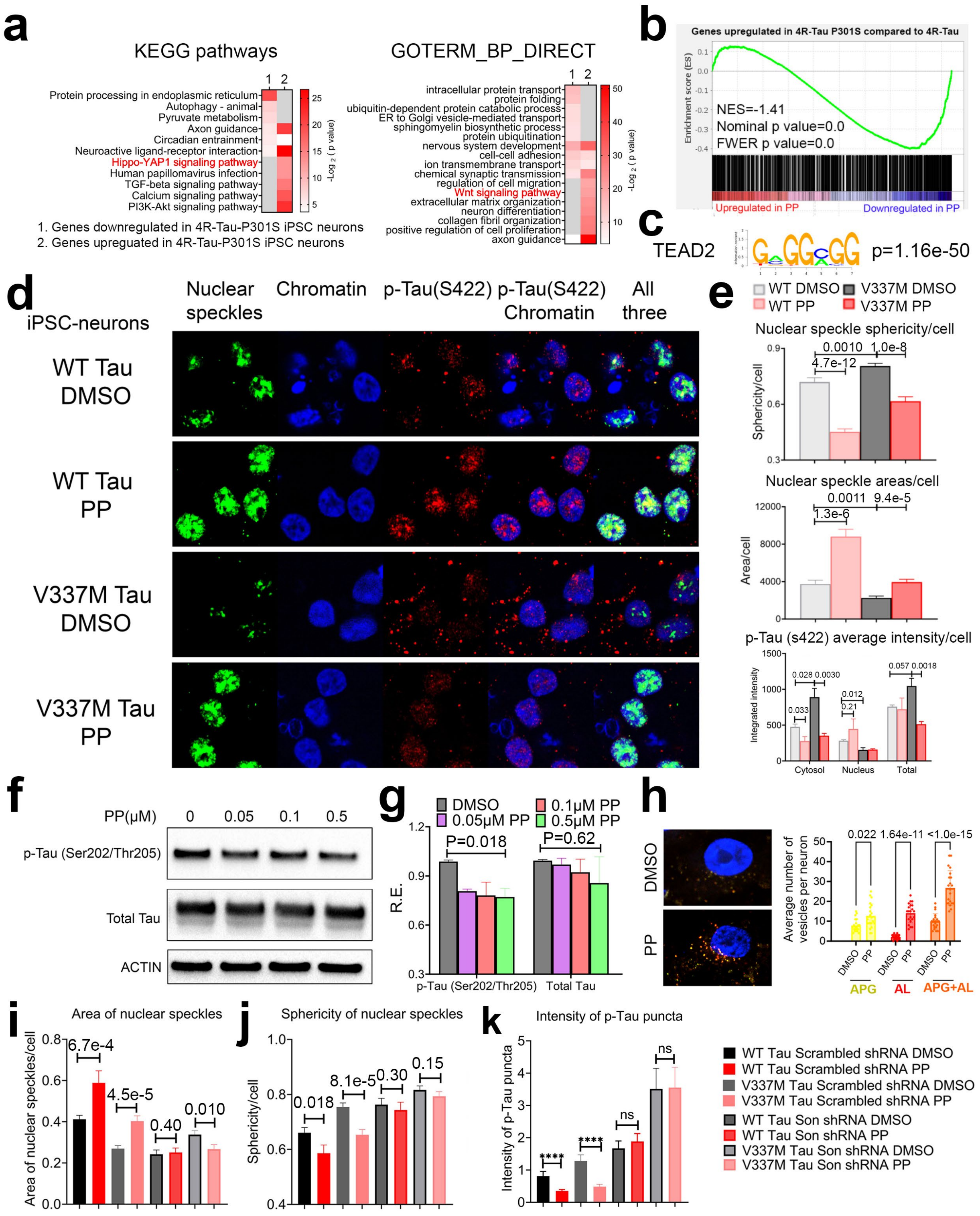

Fig. 6. PP rejuvenates nuclear speckles and alleviates tau burden in human iPSC-neurons expressing mutant Tau. (**a**) GO analysis of up and downregulated genes in 4R-Tau P301S iPSC neurons reported in [74]. (**b**) GSEA comparing genes upregulated in 4R-Tau P301S iPSC neurons with those downregulated by PP. (**c**) Motif analysis of promoters of genes upregulated in 4R-Tau

P301S iPSC neurons compared to 4R-Tau (FDR<0.05) revealed top enriched motif of TEAD2. (**d, e**) Wild-type and V337M Tau-expressing iPSC-neurons were treated with DMSO or PP (10nM) for 12 hours, and IF against nuclear speckle (Ab11826 against SRRM2), p-Tau (Ser422) and chromatin (DAPI) were performed. Representative images (**d**) and quantification of nuclear speckle sphericity and area, intensity of nuclear, cytosol and total level of p-Tau (Ser422) and ratio of cytosol versus nuclear level of p-Tau (**e**). (**f, g**) V337M Tau-expressing iPSC-neurons were treated with DMSO or increasing concentrations of PP for 12 hours. Representative western blot (**f**) and quantification (**g**) of total and p-Tau (Ser202/Thr205) (n=3). (**h**) V337M Tau-expressing iPSC-neurons were treated with DMSO or 100nM PP for 12 hours, and autophagy flux was quantified by the autophagy reporter. (**i-k**) Wild-type and V337M Tau-expressing iPSC-neurons were infected with scrambled shRNA or SON shRNA-encoding lentivirus and treated with DMSO or PP (100nM) for 12 hours, and IF against nuclear speckle (Ab11826 against SRRM2), p-Tau (Ser422) and chromatin (DAPI) were performed. Quantification of nuclear speckle area (**i**) sphericity (**j**), intensity of total level of p-Tau (Ser422) (**k**) were shown. Data: Mean ± SEM.

Supplementary Figures.

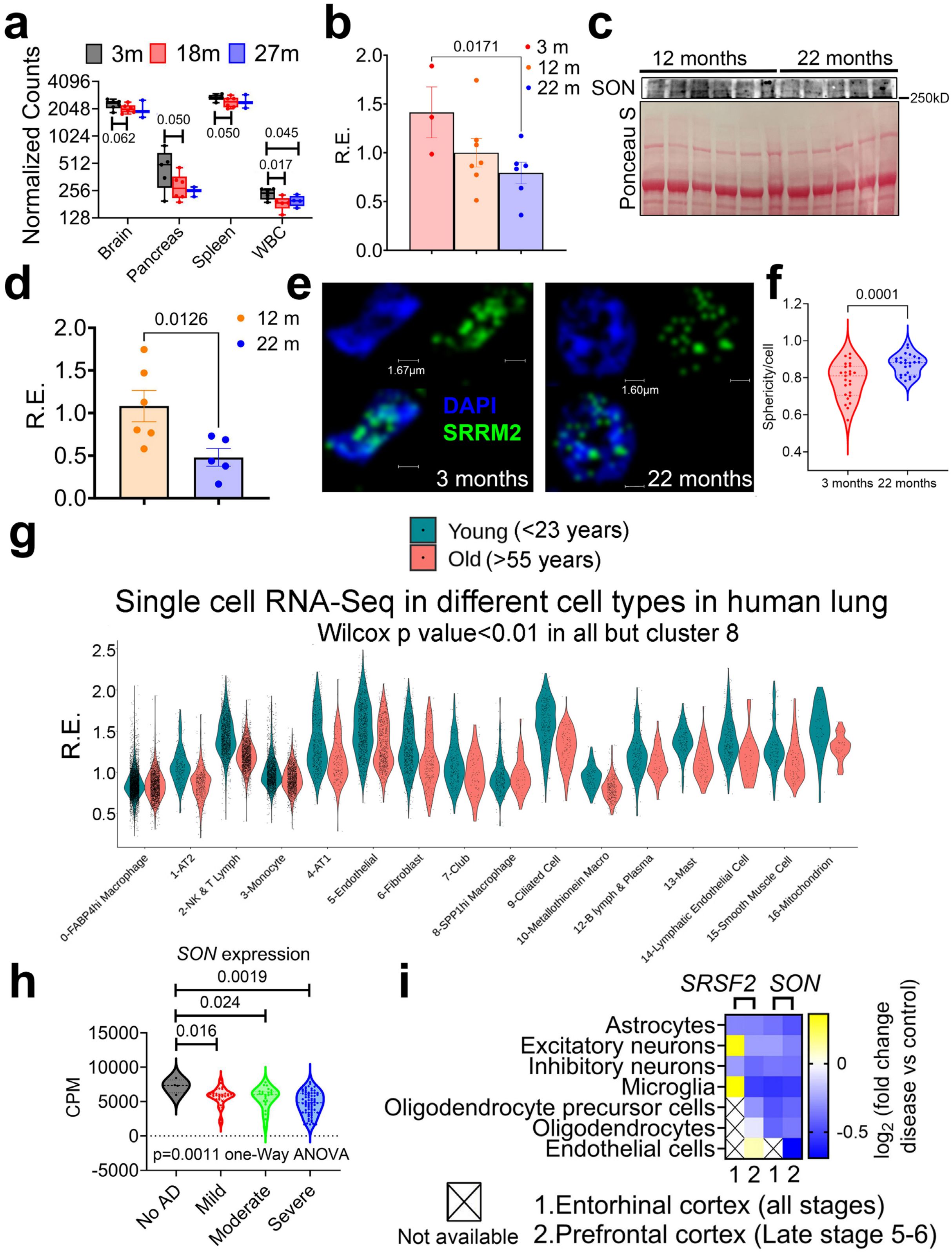

Supplementary Figure 1. SON expression is reduced during aging in mice and humans. (**a**) Normalized counts of *Son* mRNA in different mouse tissues with different ages (WBC; White blood cells) according to Tabula Muris Senis database (n=3~6) [132, 133]. (**b**) qPCR of *Son* level in liver of mice with different ages (n=3~7). (**c, d**) Western blot (**c**) and quantification (**d**) of SON level in liver of mice with different ages (n=5~6). (**e, f**) Representative immunofluorescence images of SRRM2 and DAPI in the liver of 3 and 22 months old male mice (**e**) and quantification of the sphericity of nuclear speckles (**f**). n=25 for both age groups. (**g**) Single cell RNA-seq data of *SON* mRNA level in different cell types in lung tissues of young and aging humans, reported from [20]. (**h**) Counts per million normalized expressions of *SON* in brains of human AD compiled from RNA-seq data from the AMP-AD consortium. (**i**) Heat map showing relative expression of *SRSF2* and *SON* in different cell types in the cortex of human AD subjects [134]. Blue color indicates lower level in AD subjects compared to controls. Data: Mean ± S.E.M. Statistical tests used: two-way ANOVA and Turkey multiple comparison for h, unpaired one-tailed Student's t-test for a, b, d, and f. Wilcoxon test for g.

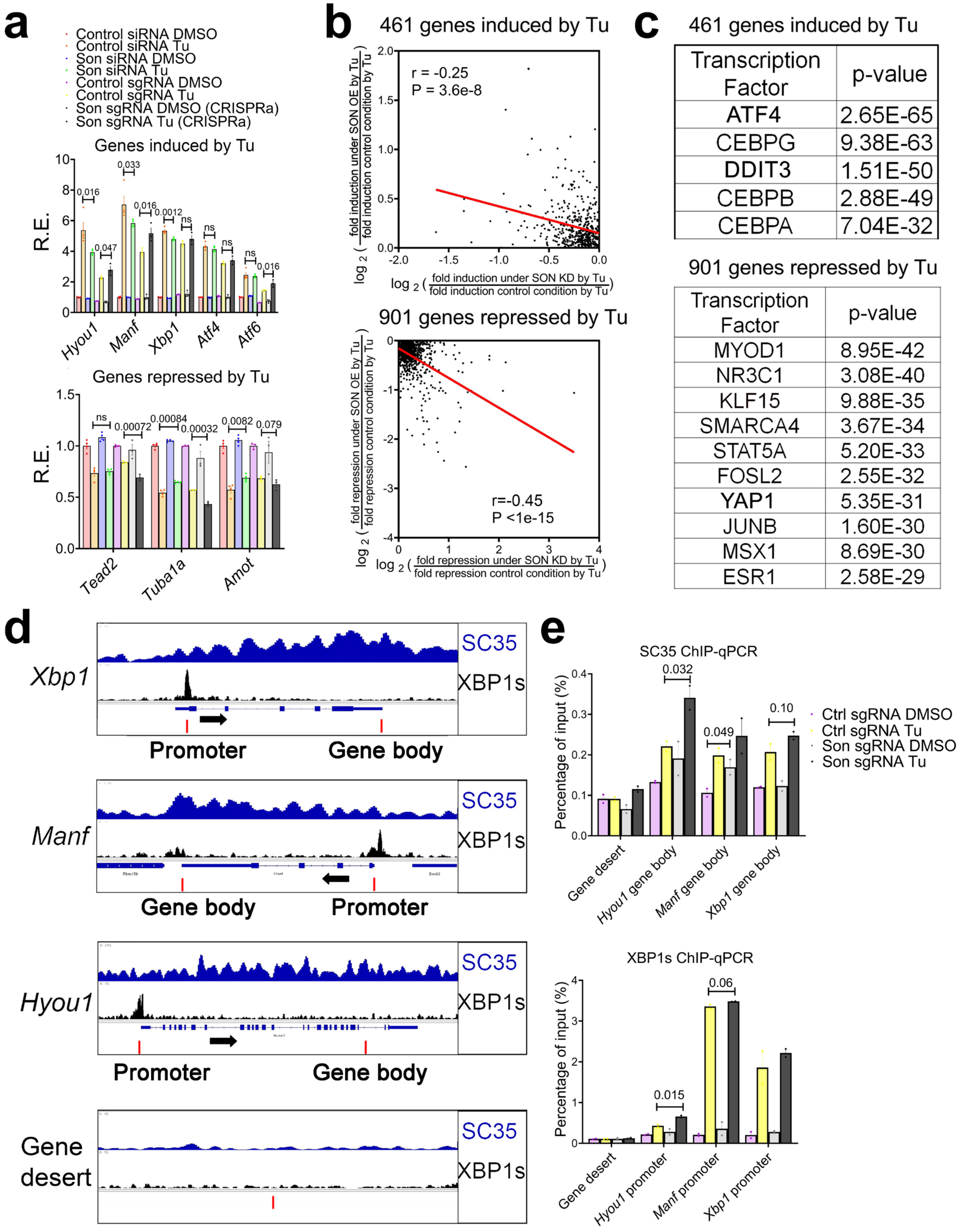

461 genes induced by Tu

Transcription Factor	p-value
ATF4	2.65E-65
CEBPG	9.38E-63
DDIT3	1.51E-50
CEBPB	2.88E-49
CEBPA	7.04E-32

901 genes repressed by Tu

Transcription Factor	p-value
MYOD1	8.95E-42
NR3C1	3.08E-40
KLF15	9.88E-35
SMARCA4	3.67E-34
STAT5A	5.20E-33
FOSL2	2.55E-32
YAP1	5.35E-31
JUNB	1.60E-30
MSX1	8.69E-30
ESR1	2.58E-29

Supplementary Figure 2. Genetic rejuvenation of nuclear speckles by SON. (**a**) Relative expression (R.E.) of representative proteostasis genes (top) and YAP1 target genes (bottom) in response to Tu in the presence of SON OE/KD (n=4 for SON KD and n=3 for SON OE). (**b**) Scatter plot showing relative fold change by *Son* KD versus SON OE for both Tu-induced and Tu-repressed genes. (**c**) Top predicted transcription regulators of 461 and 901 genes by the LISA Cistrome DB TR ChIP-Seq models. (**d, e**) Selected genes aligned for SC35 and XBP1s ChIP-seq signal from CT12 in XBP1^{Flox} mice [6] (**d**) and ChIP-qPCR of XBP1s and SC35 on selected regions (indicated by red bars) (n=2) (**e**). Data: Mean ± S.E.M. Statistical tests used: unpaired one-tailed Student's t-test for a and e. Linear regression for b.

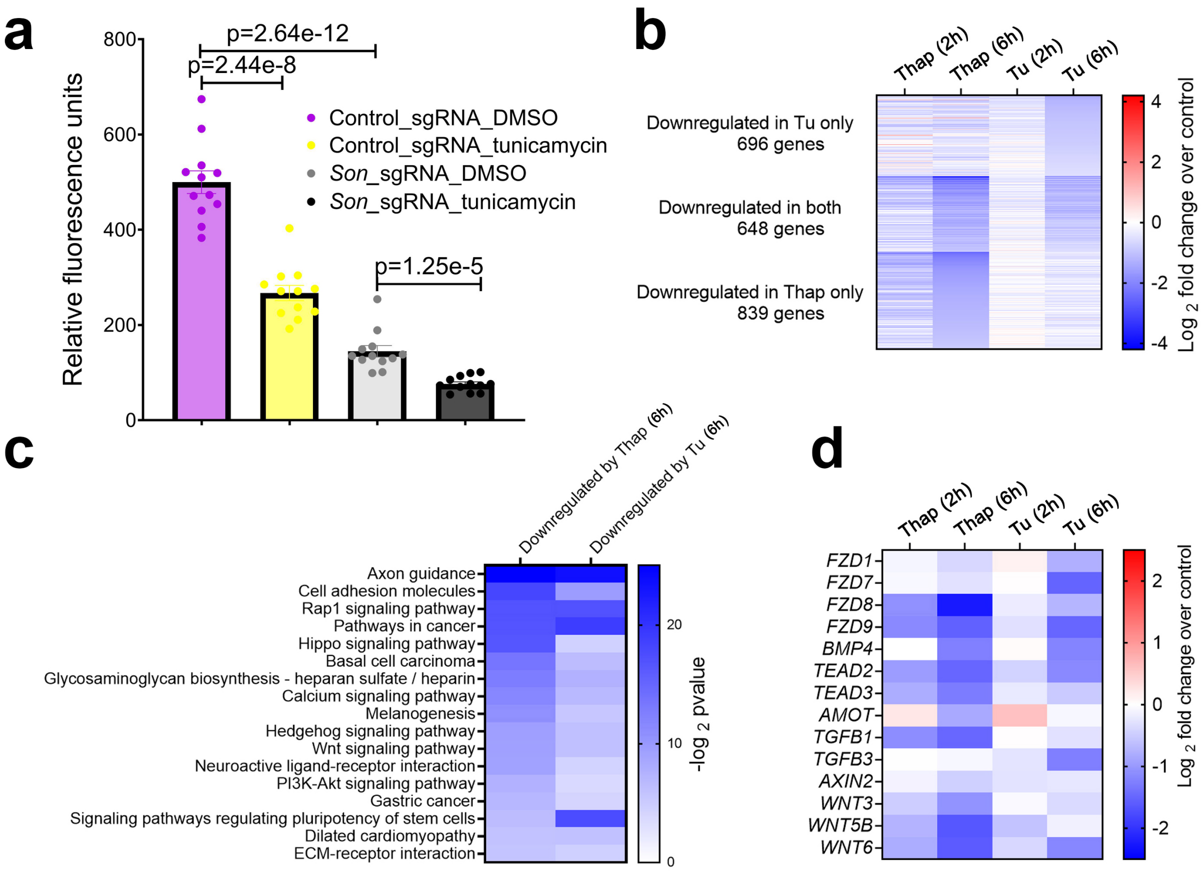

Supplementary Figure 3. YAP1 transcriptional output is repressed during ER stress. (**a**) TEAD luciferase reporter assay in control and SON OE MEFs in response to Tu (n=12 for all groups). (**b**) Heatmap showing transcriptomes that are significantly downregulated (log $_2$-fold change smaller than -0.5) with a p value less than 0.05) either under Tu or Thap treatment at 6h. (**c**) GO analysis of genes that are significantly downregulated either under Tu or Thap treatment at 6h. (**d**) Heatmap of representative YAP1 target genes as in **b**. Data: Mean ± S.E.M. Statistical tests used: unpaired one-tailed Student's t-test for a.

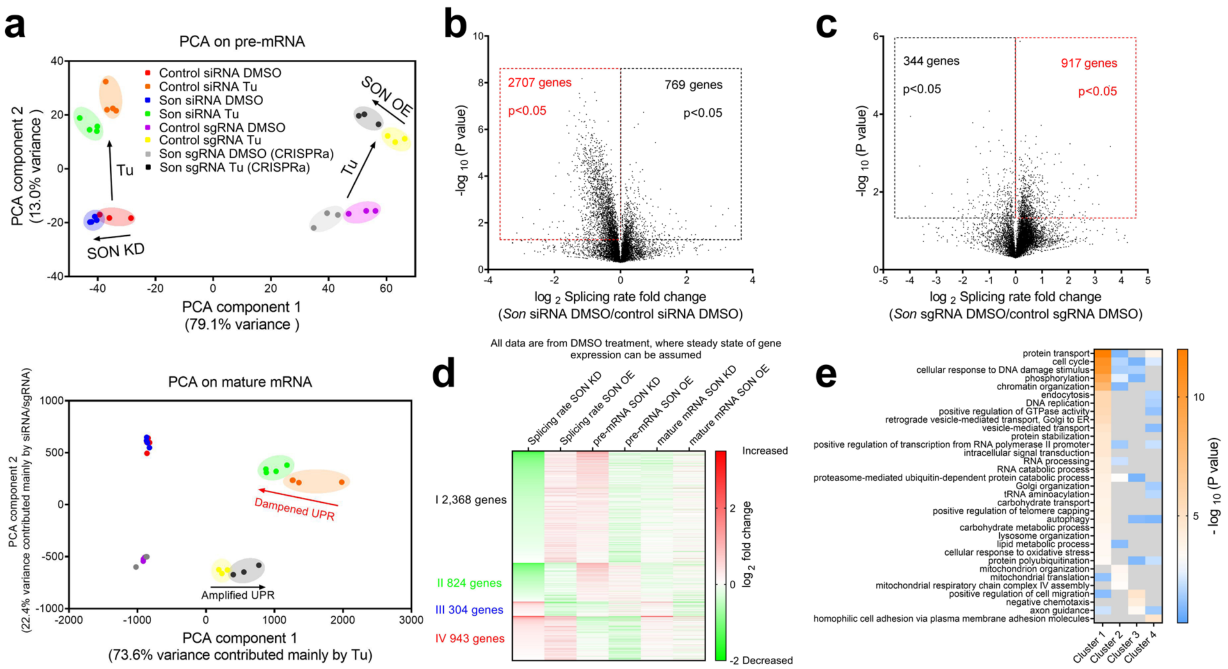

Supplementary Figure 4. SON regulates mRNA splicing rates under both basal and ER stress conditions (**a**) PCA analysis of global transcriptional response to Tu in the presence of SON OE/KD. Both pre-mRNA (top) and mature mRNA (bottom) are shown. (**b, c**) Volcano plot of mRNA splicing rates changes in SON KD (**b**) or OE (**c**) MEFs under basal condition (DMSO). (**d**) Heat map of fold change of RNA splicing rate, pre and mature mRNA level in SON OE/KD MEFs compared to control MEFs under vehicle (DMSO) condition. Four clusters of genes are shown. (**e**) GO analysis of genes in four clusters showing enriched KEGG pathways.

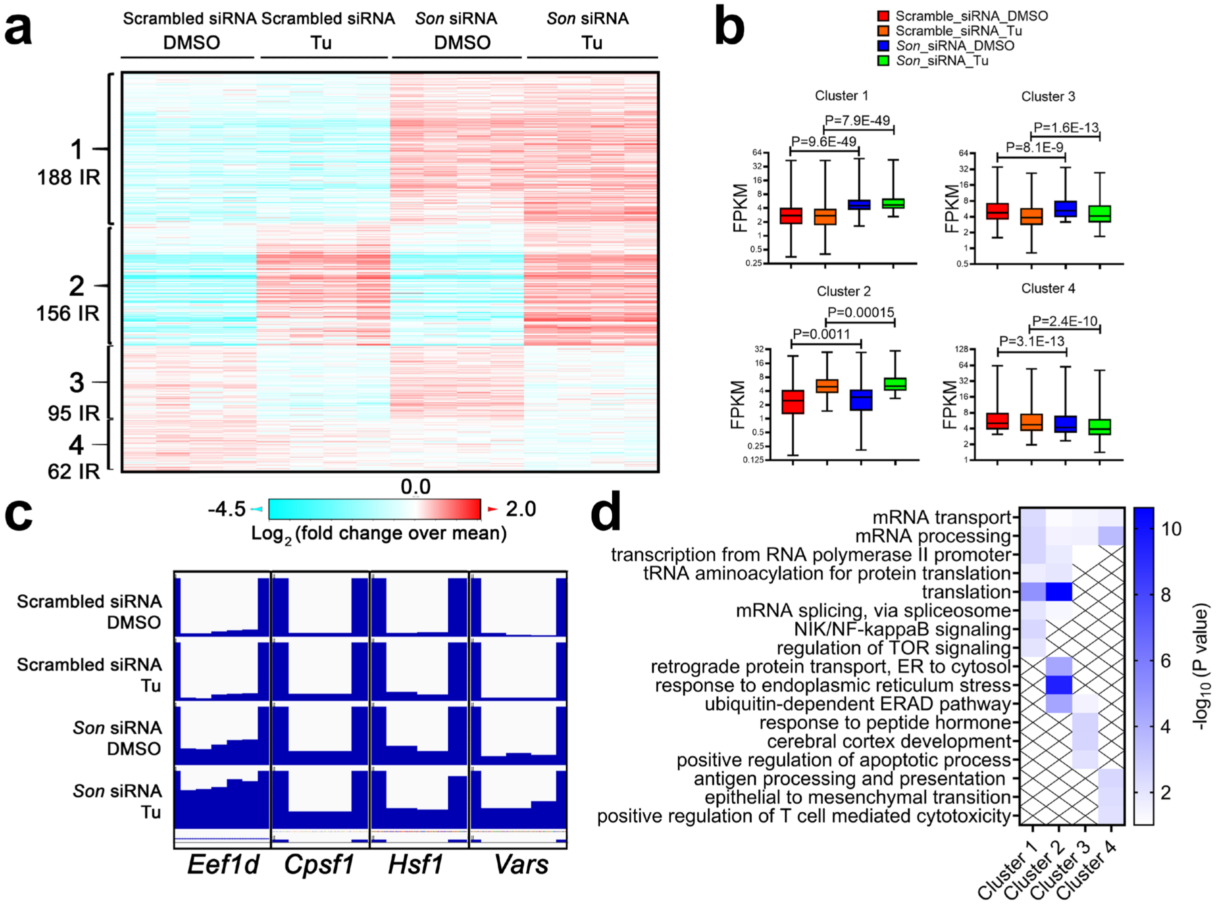

Supplementary Figure 5. SON knockdown increases intron retention of proteostasis and mRNA metabolism genes. Heat map (**a**) and quantification (**b**) of intron retention events in MEFs with control or SON KD under basal (DMSO) and Tu conditions. Four clusters are shown. (**c**) The Integrative Genome Viewer representation of intron retention in selected genes. (**d**) GO analysis of genes in four clusters showing enriched KEGG pathways. Data: box and whiskers with minimum to maximum. Statistical tests used: unpaired one-tailed Student's t-test for b.

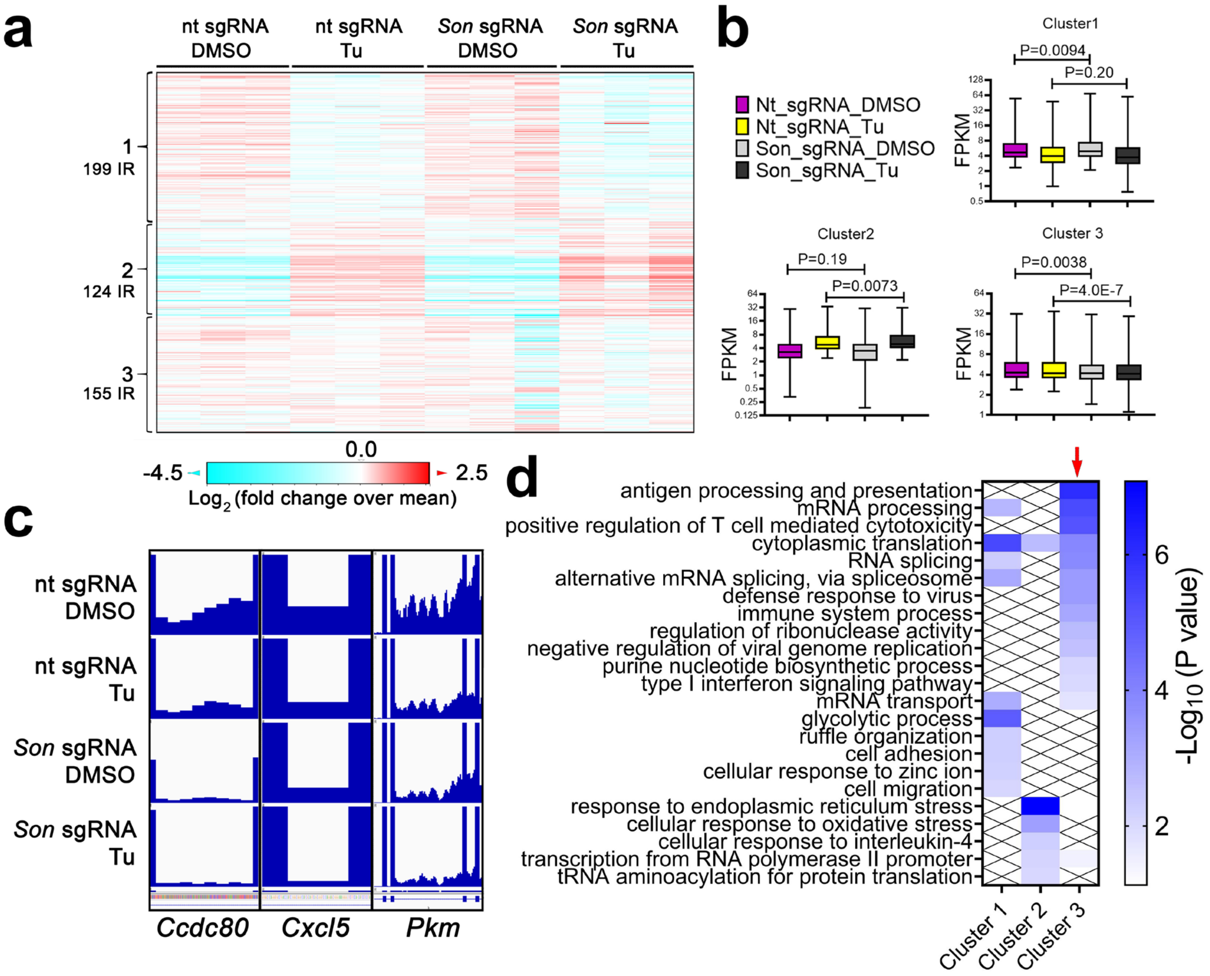

Supplementary Figure 6. SON overexpression decreases intron retention of protein processing and mRNA metabolism genes. Heat map (**a**) and quantification (**b**) of intron retention events in MEFs with control or SON overexpression under basal (DMSO) and Tu conditions. Three clusters are shown. (**c**) The Integrative Genome Viewer representation of intron retention in selected genes. (**d**) GO analysis of genes in three clusters showing enriched KEGG pathways. Data: box and whiskers with minimum to maximum. Statistical tests used: unpaired one-tailed Student's t-test for b.

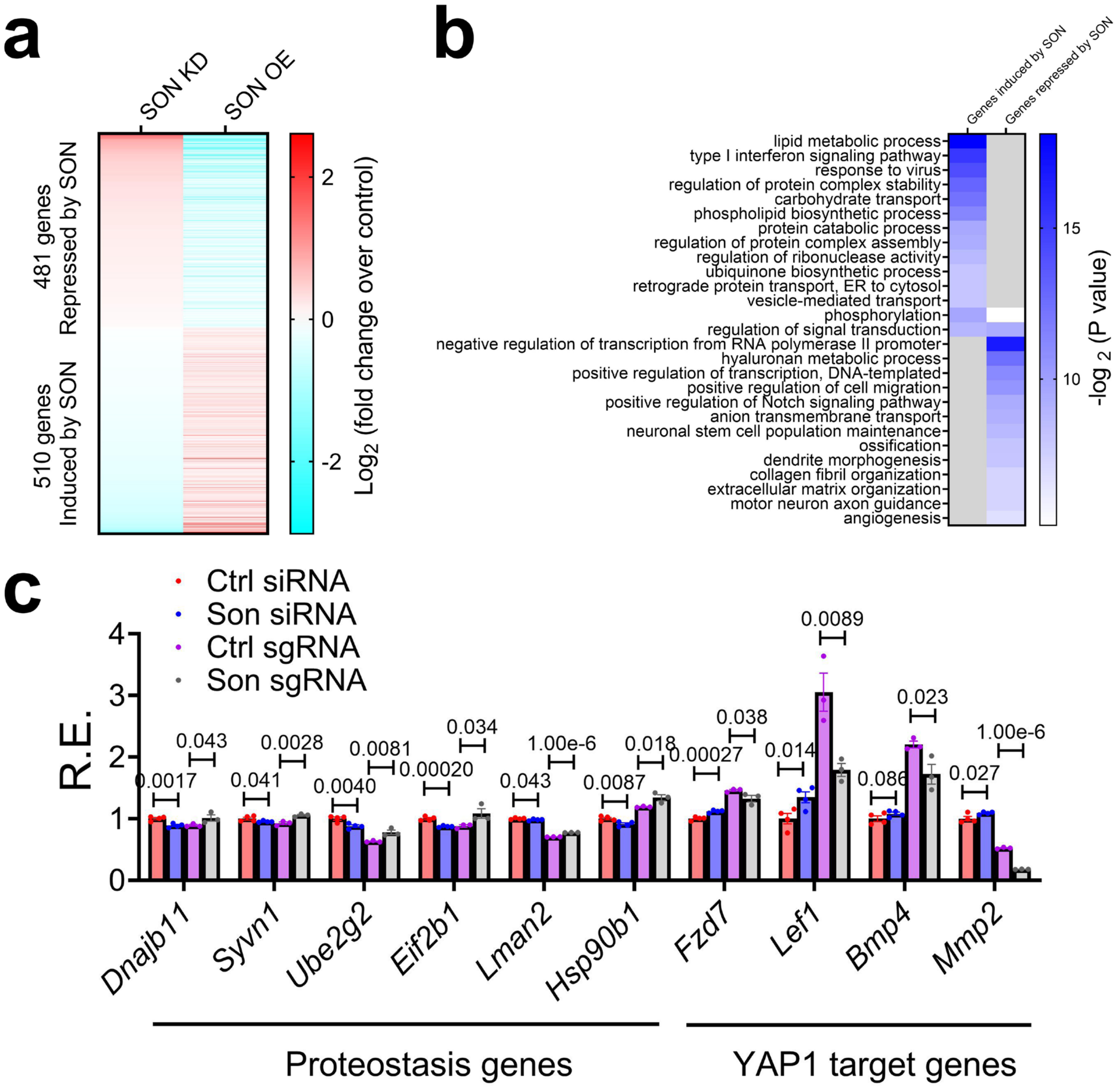

Supplementary Figure 7. SON reprograms opposing proteostasis and YAP1 transcriptional output under basal conditions. (**a**) Heat map of fold change of mature mRNA level in *Son* OE/KD MEFs compared to control MEFs under vehicle (DMSO) condition. All mature mRNAs in this heatmap are statistically differentially expressed (P<0.05) in both SON OE/KD conditions, compared to their respective controls. (**b**) GO analysis of these 481 and 501 genes. (**c**) Representative mature mRNA expression of proteostasis and YAP1 target genes (n=4 for Ctrl and *Son* siRNA and n=3 for Ctrl and *Son* sgRNA). Data: Mean ± S.E.M. Statistical tests used: unpaired one-tailed Student's t-test for c.

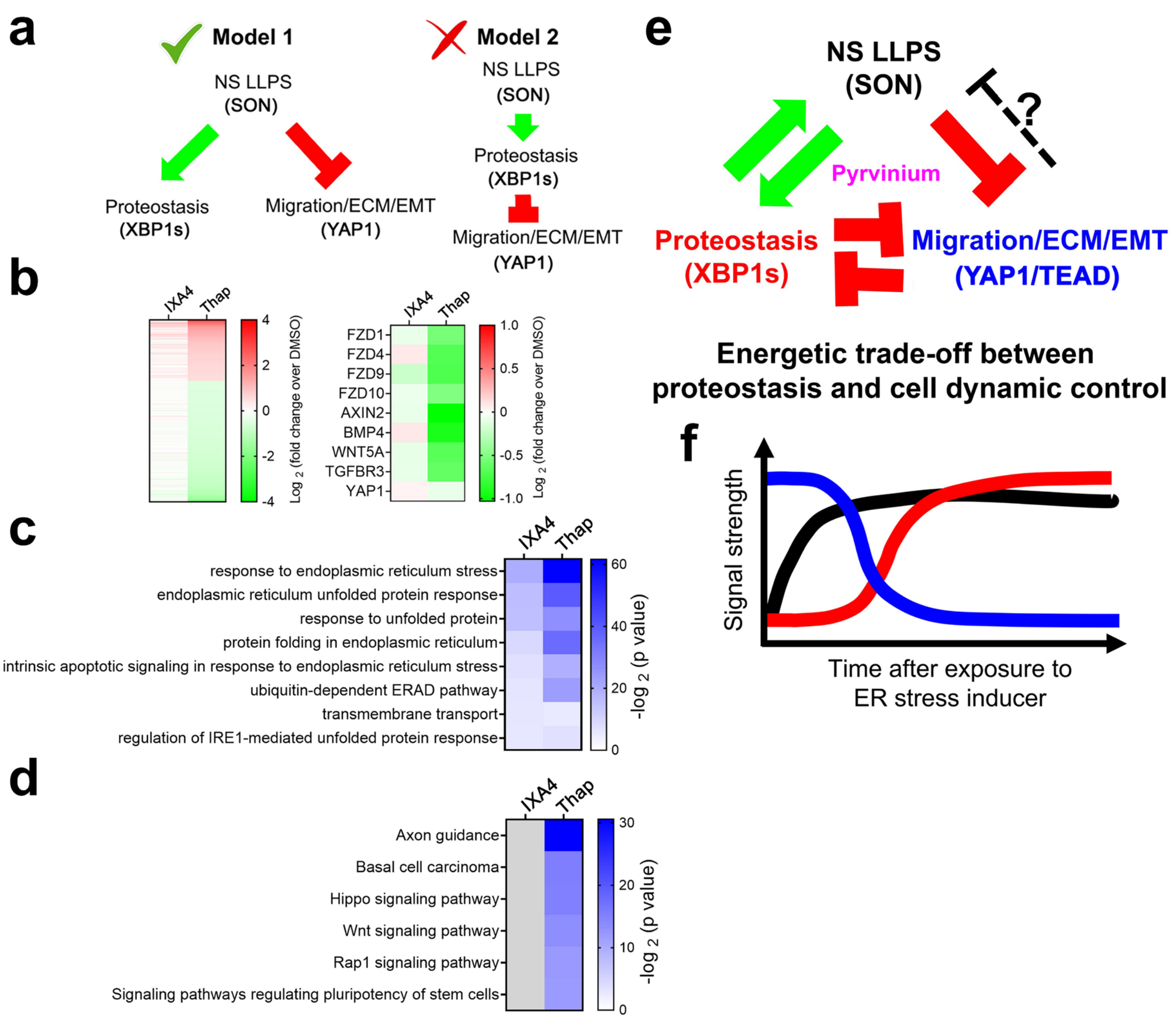

Supplementary Figure 8. Nuclear speckle LLPS dictates opposing proteostasis and YAP1 signaling. (**a**) Two models explaining the relationship among nuclear speckles LLPS dynamics, proteostasis and YAP1 transcriptional output. Our results support model 1. (**b**) Heatmap demonstrates relative fold change of gene expression relative to DMSO control in IXA4, or Thap treated HEK293T cells. All genes induced or repressed by at least 1.41-fold with p value smaller than 0.05 in Thap condition (left), and representative YAP1-related genes (right). (**c, d**) GO analysis of all upregulated (**c**) or downregulated (**d**) genes in either IXA4 or Thap treatment by at least 1.41-fold with a p-value smaller than 0.05. (**e**) An expanded model of how the LLPS of nuclear speckles can dictate proteostasis and YAP1 transcriptional output. Please see the main text for details. (**f, g**) Diagram showing temporal changes of NS' LLPS (black), proteostasis (red) and YAP1 transcriptional output (blue) signal during ER stress (**f**).

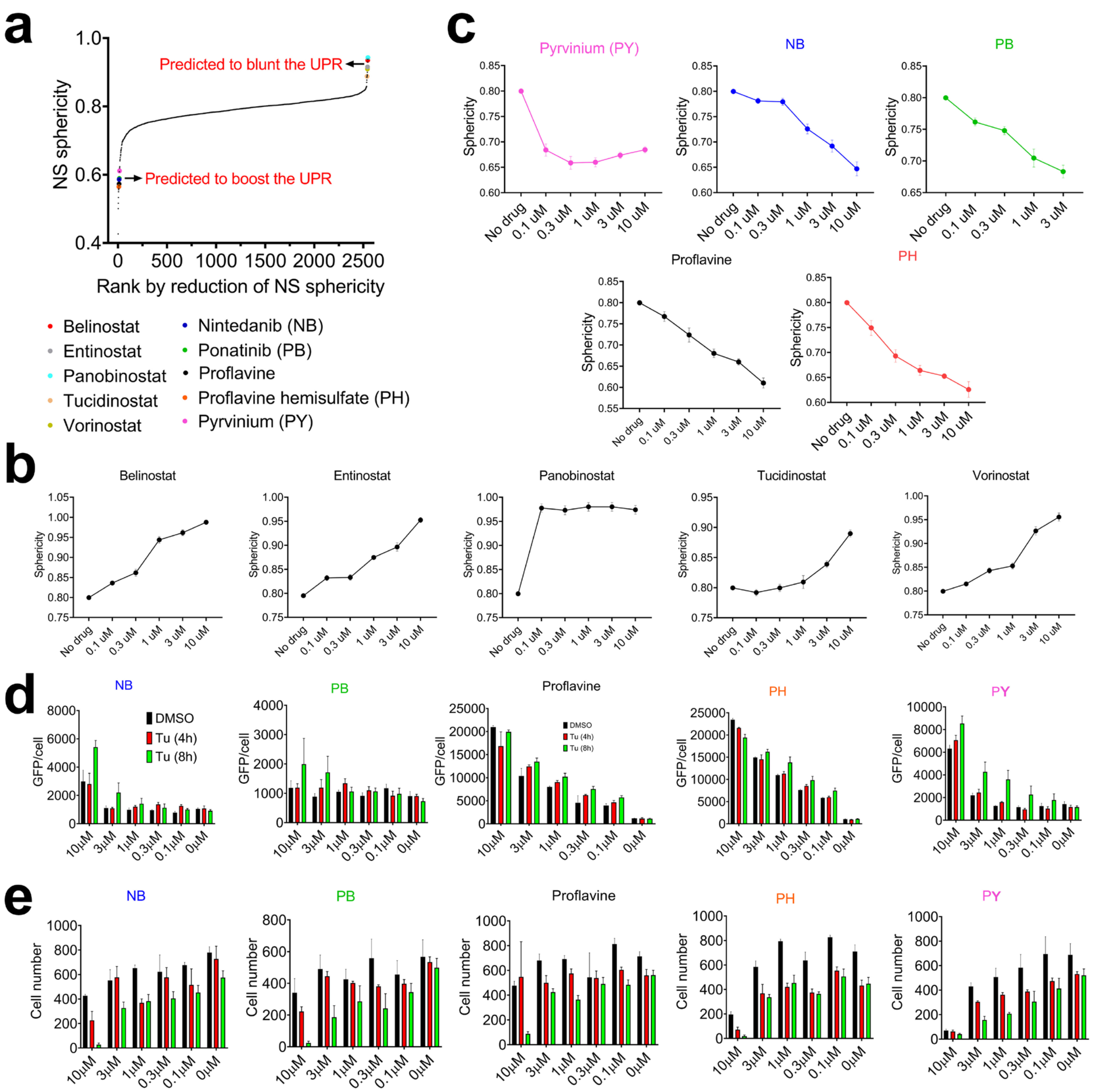

Supplementary Figure 9. HTS identifies compounds that alter nuclear speckle morphology and the UPR. (**a**) Compounds in the FDA-approved library ranked from lowest to highest on their ability to reduce NS sphericity. (**b**) Five drugs are shown to have a dose-dependent effect on increasing sphericity of NS (n=16). (**c**) Dose-dependent effects of drugs on decreasing NS sphericity (n=16). (**d, e**) GFP/cell (**d**) or cell number (**e**) measured in *Perk* promoter-driven dGFP reporter MEFs in the presence of Tu for four or eight hours after pre-treatment of different concentrations of drugs or DMSO for 24 hours (n=4). Data: Mean ± S.E.M.

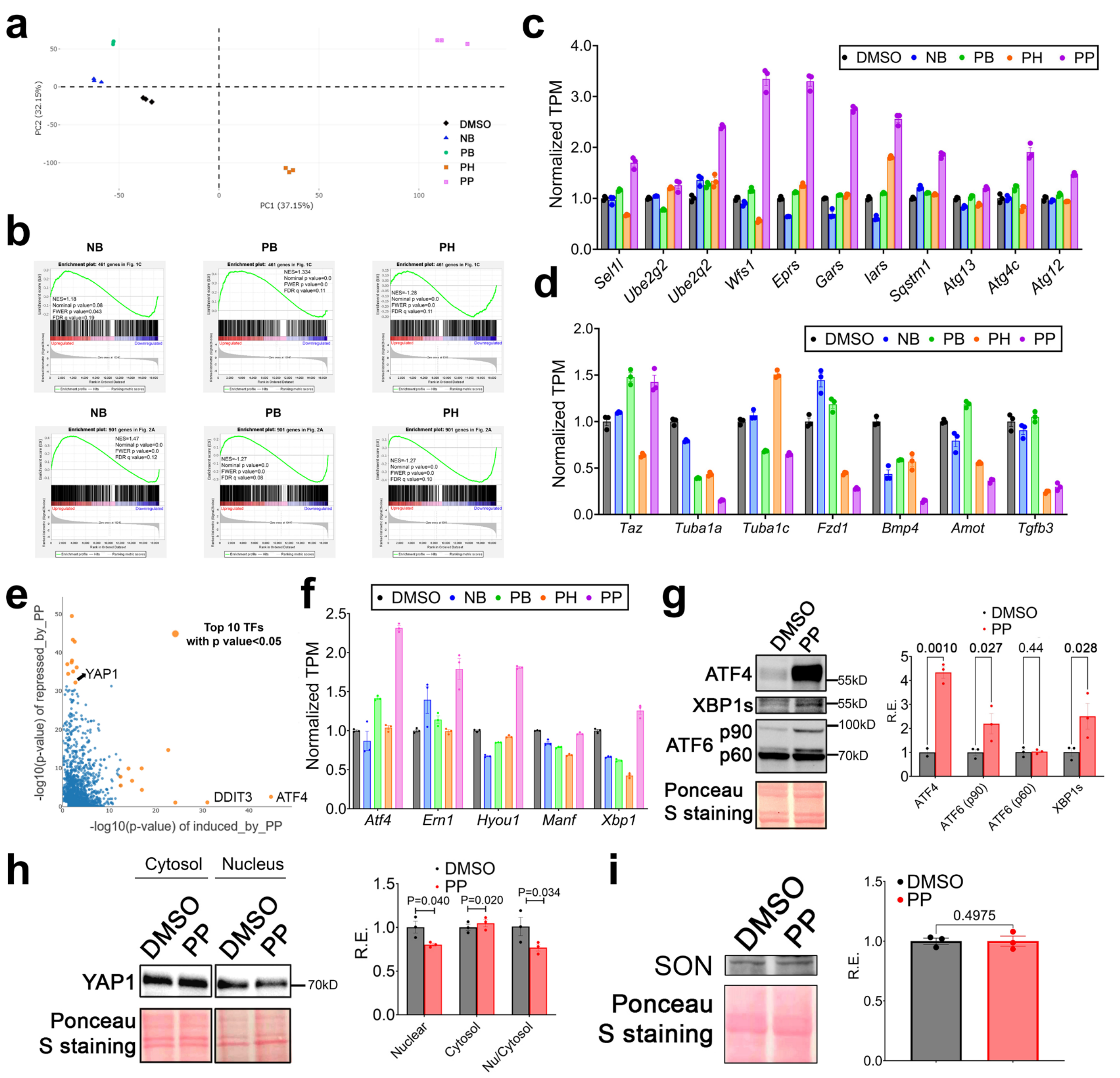

Supplementary Figure 10. PP is a bona fide nuclear speckle rejuvenator. (**a**) MEFs were treated with 3 µM NB, 1 µM PB, 3 µM PH, and 1 µM PP for 24 hours and RNA-seq was performed. PCA of global transcriptional response to drug treatments. (**b**) For each of the GSEA analysis, genes further activated by SON OE or further repressed by SON OE are compared to the transcriptome signatures of MEFs under different drug treatments. (**c, d**) Gene expression of select protein quality control (**c**) and YAP1 target genes (**d**) genes determined through mRNA-Seq (n=3). (**e**) LISA analysis listing log transformed p values for top predicted transcription regulators for genes upregulated (x-axis) and downregulated (y-axis) by PP. (**f**) Gene expression of select UPR genes determined through mRNA-Seq under different drugs treatment (n=3). (**g-i**) Western blot and quantification of UPR TFs (**g**), YAP1 nuclear and cytosol (**h**) and SON (**i**) level in response to 1 µM PP for 24 hours (n=3). Data: Mean ± S.E.M. Statistical tests used: unpaired one-tailed Student's t-test for g-i.

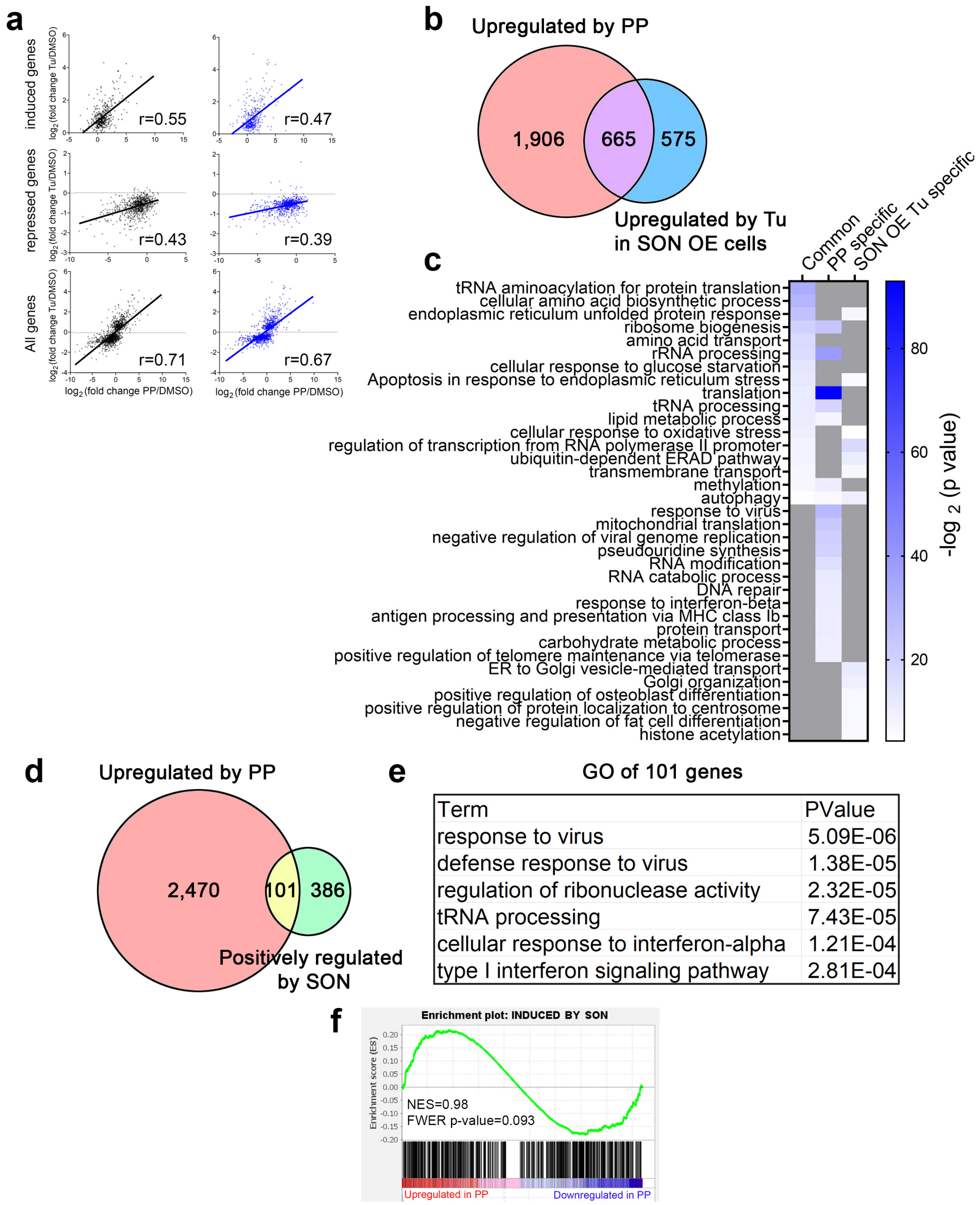

Supplementary Figure 11. Comparison of upregulated genes by PP and SON OE. (**a**) Scatter plot comparing the fold change of gene expression by PP (x-axis) and by Tu (y-axis) under SON OE or SON KD condition. Correlation coefficient and p value are shown for each plot. Chow test indicates statistically significant coefficients between the two linear regressions with p=0.00195. (**b, c**) Venn diagram showing (**b**) and GO analysis of (**c**) specific and commonly upregulated genes by PP and Tu in SON OE MEFs. (**d**) Venn diagram showing specific and common upregulated genes by PP and SON in MEFs. (**e**) GO analysis of common 101 genes. (**f**) GSEA analysis comparing genes upregulated by SON with those regulated by PP.

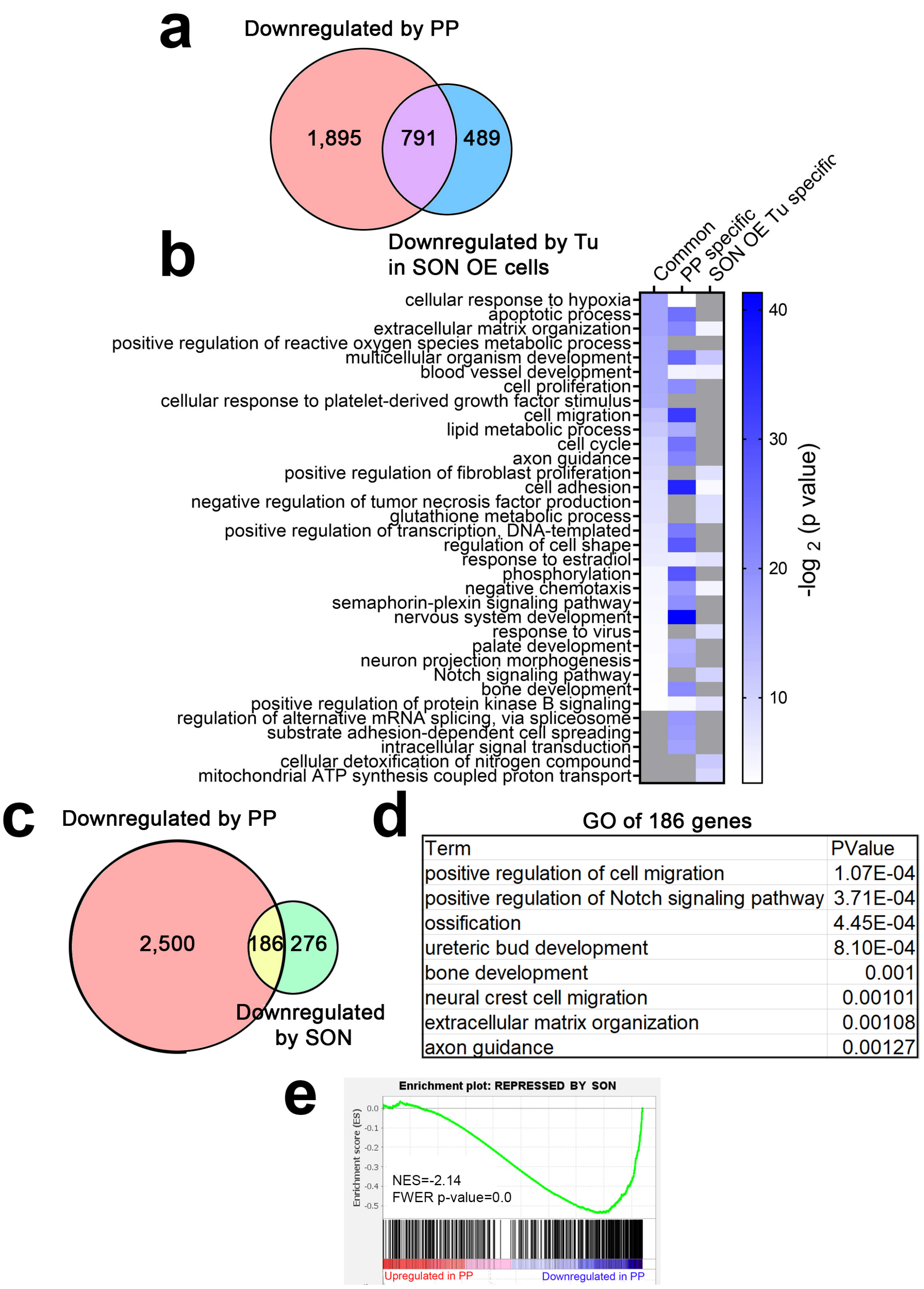

GO of 186 genes

Term	PValue
positive regulation of cell migration	1.07E-04
positive regulation of Notch signaling pathway	3.71E-04
ossification	4.45E-04
ureteric bud development	8.10E-04
bone development	0.001
neural crest cell migration	0.00101
extracellular matrix organization	0.00108
axon guidance	0.00127

Supplementary Figure 12. Comparison of downregulated genes by PP and SON OE. (**a-b**) Venn diagram showing (**a**) and GO analysis of (**b**) specific and common downregulated genes by PP and Tu in SON OE MEFs. (**c**) Venn diagram showing specific and common downregulated genes by PP and SON in MEFs. (**d**) GO analysis of 186 common genes. (**e**) GSEA analysis comparing genes downregulated by SON with those regulated by PP.

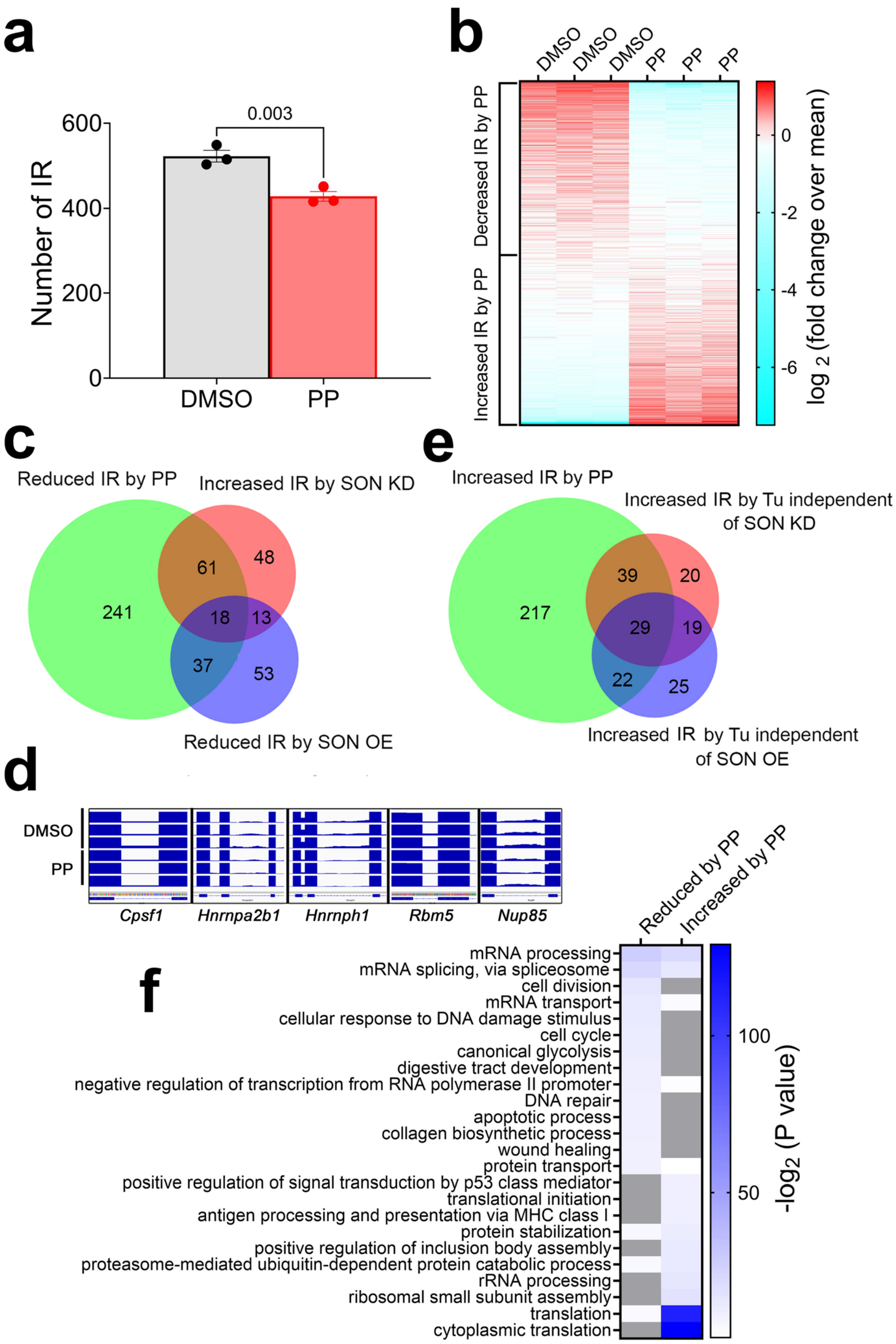

Supplementary Figure 13. Comparison of intron retention (IR) events among PP, SON OE and SON KD. (**a**) Quantification of IR under DMSO and PP condition (n=3). (**b**) Heatmap showing RPKM normalized level of retained introns in DMSO and PP condition. (**c, d**) Venn diagram comparing genes with specific or common IRs between different conditions. (**e**) Genome browser view of selective genes with reduced IR by PP. (**f**) GO analysis of genes with increased or reduced IR by PP. Data: Mean ± S.E.M. Statistical tests used: unpaired one-tailed Student's t-test for a.

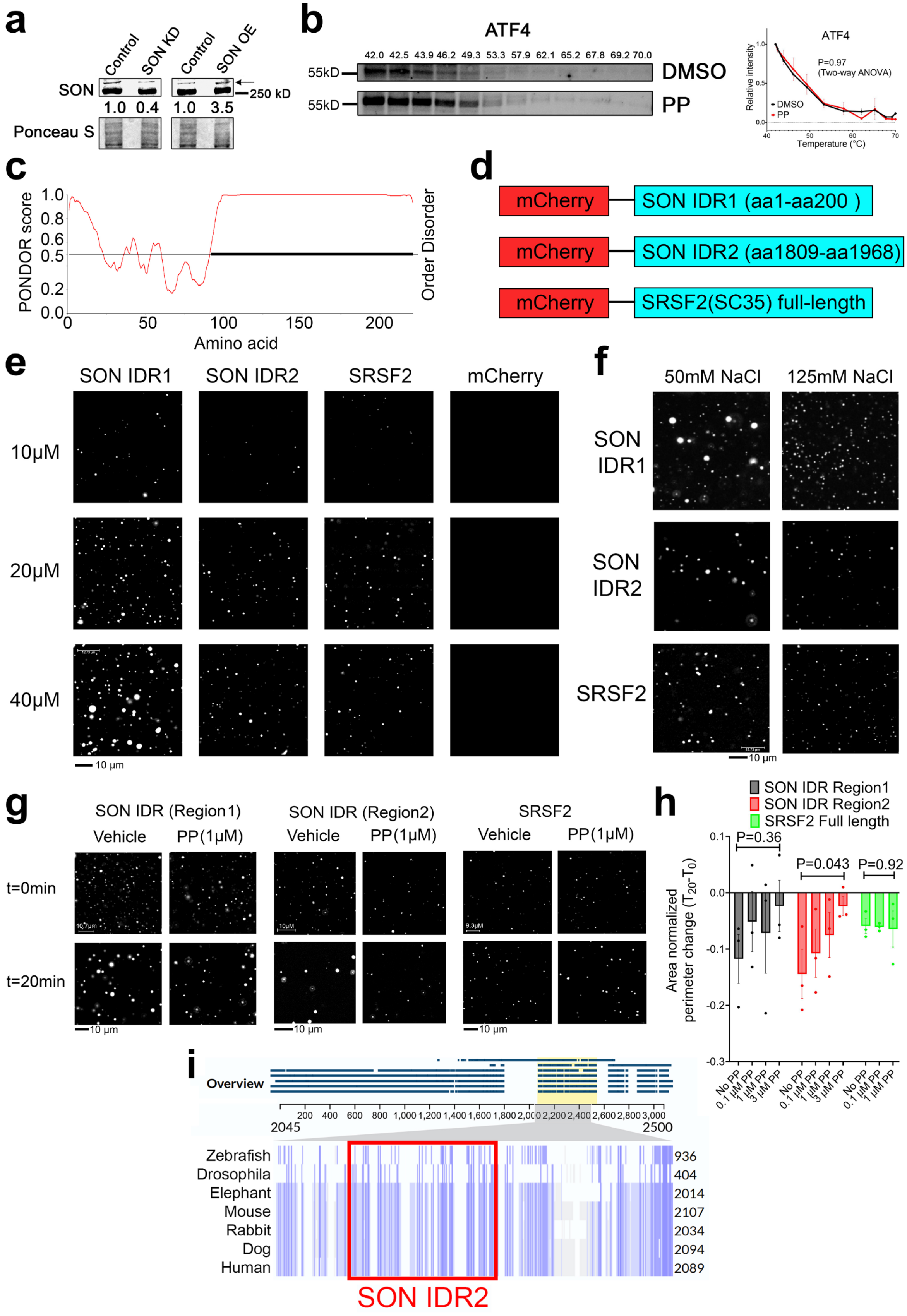
a
Control
SON KD
Control
SON OE
SON
250 kD
1.0 0.4
1.0 3.5
Ponceau S
b
ATF4
42.0 42.5 43.9 46.2 49.3 53.3 57.9 62.1 65.2 67.8 69.2 70.0
55kD
DMSO
55kD
PP
ATF4
Relative intensity
P=0.97
(Two-way ANOVA)
DMSO
PP
Temperature (°C)
c
PONDOR score
Order Disorder
Amino acid
d
mCherry
SON IDR1 (aa1-aa200)
mCherry
SON IDR2 (aa1809-aa1968)
mCherry
SRSF2(SC35) full-length
e
SON IDR1
SON IDR2
SRSF2
mCherry
10μM
20μM
40μM
10 μm
f
50mM NaCl
125mM NaCl
SON IDR1
SON IDR2
SRSF2
10 μm
g
SON IDR (Region1)
SON IDR (Region2)
SRSF2
Vehicle
PP(1μM)
Vehicle
PP(1μM)
Vehicle
PP(1μM)
t=0min
t=20min
10 μm
10 μm
10 μm
h
SON IDR Region1
SON IDR Region2
SRSF2 Full length
Area normalized perimeter change (T_{20}-T_0)
P=0.36
P=0.043
P=0.92
No PP
0.1 μM PP
1 μM PP
3 μM PP
i
Overview
2045
2500
Zebrafish 936
Drosophila 404
Elephant 2014
Mouse 2107
Rabbit 2034
Dog 2094
Human 2089
SON IDR2

Supplementary Figure 14. PP directly targets SON to modulate nuclear speckle LLPS dynamics. (**a**) Western blots of SON with siRNA-mediated knockdown and SON OE. (**b**) CETSA of ATF4 with 3μM PP. Both representative blot and quantification from independent replicates are shown (n=2 for DMSO and n=3 for PP). (**c**) Computational prediction of IDR in mouse SRSF2 (SC35) protein. (**d**) Diagram illustrating the constructs for droplet formation assay (**e**) Representative images of droplet formation assay with different concentrations of recombinant protein at 125mM NaCl. (**f**) Representative images of droplet formation assay with different salt concentrations with 20μM recombinant proteins. (**g, h**) Representative images of droplet formation assay with different recombinant proteins (**g**) and quantification (**h**) of area-normalized perimeter changes in the time span of 20 minutes with 50mM NaCl (n=3). (**i**) Alignment of protein sequences of SON orthologs in seven different species. SON IDR2 is located within the most conserved region (highlighted by light yellow). Data: Mean ± S.E.M. Statistical tests used: Two-way ANOVA for b and one-way ANOVA for h.

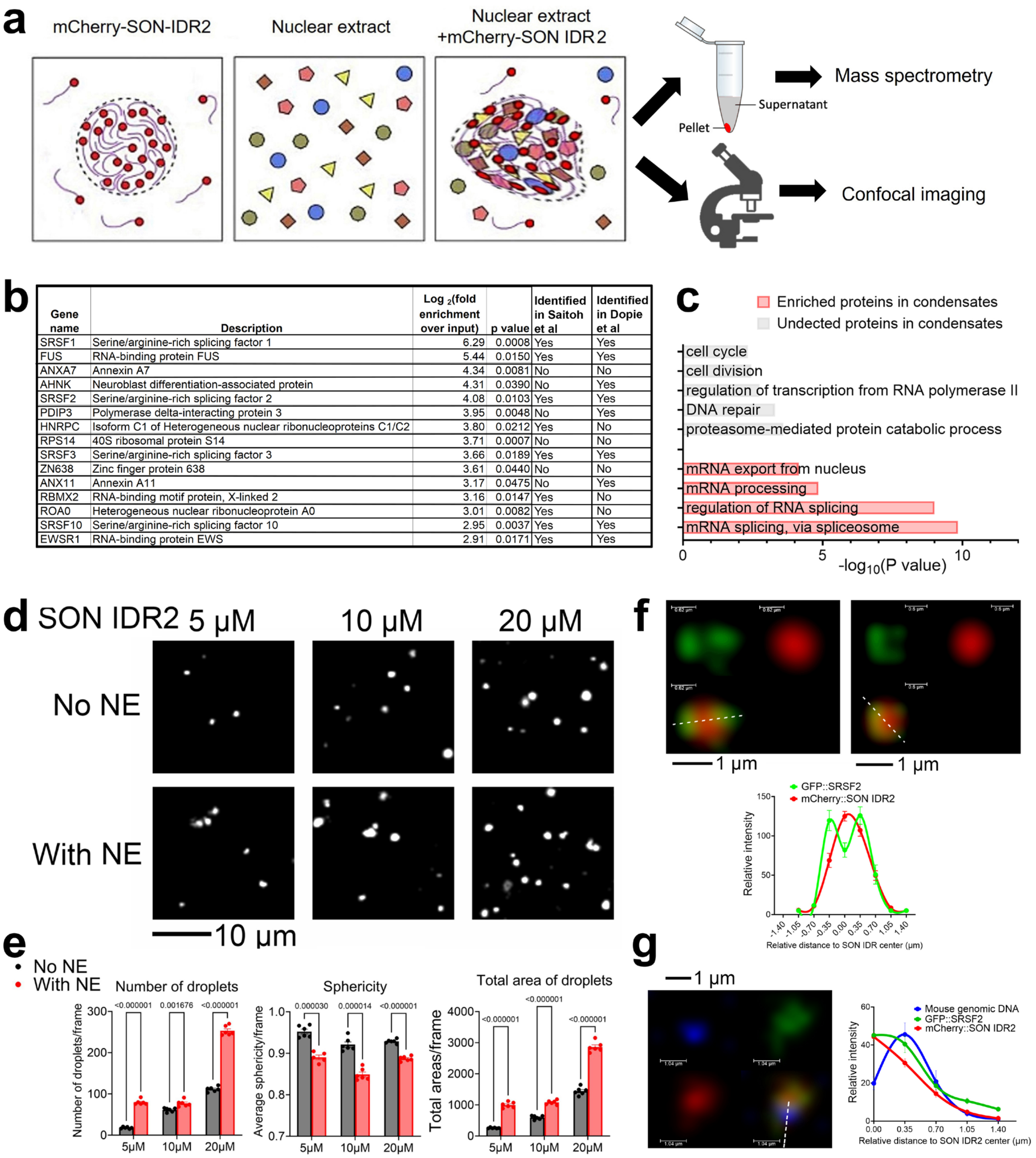

Gene name	Description	Log $_2$(fold enrichment over input)	p value	Identified in Saitoh et al	Identified in Dopie et al
SRSF1	Serine/arginine-rich splicing factor 1	6.29	0.0008	Yes	Yes
FUS	RNA-binding protein FUS	5.44	0.0150	Yes	Yes
ANXA7	Annexin A7	4.34	0.0081	No	No
AHNK	Neuroblast differentiation-associated protein	4.31	0.0390	No	Yes
SRSF2	Serine/arginine-rich splicing factor 2	4.08	0.0103	Yes	Yes
PDIP3	Polymerase delta-interacting protein 3	3.95	0.0048	No	Yes
HNRPC	Isoform C1 of Heterogeneous nuclear ribonucleoproteins C1/C2	3.80	0.0212	Yes	No
RPS14	40S ribosomal protein S14	3.71	0.0007	No	No
SRSF3	Serine/arginine-rich splicing factor 3	3.66	0.0189	Yes	Yes
ZN638	Zinc finger protein 638	3.61	0.0440	No	No
ANX11	Annexin A11	3.17	0.0475	No	Yes
RBMX2	RNA-binding motif protein, X-linked 2	3.16	0.0147	Yes	No
ROA0	Heterogeneous nuclear ribonucleoprotein A0	3.01	0.0082	Yes	No
SRSF10	Serine/arginine-rich splicing factor 10	2.95	0.0037	Yes	Yes
EWSR1	RNA-binding protein EWS	2.91	0.0171	Yes	Yes

Supplementary Figure 15. PP modulates nuclear speckle LLPS dynamics in a cell-free system. (**a**) Diagram showing NE-supplemented SON IDR2 condensates are expected to compartmentalize splicing factors and exhibit less spherical morphology. (**b**) NE-supplemented SON IDR2 condensates are spun down and subject to mass spectrometry. Top 15 proteins mostly enriched in SON IDR2-compartmentzlied condensates with p value<0.05, and the status of whether these proteins have been identified in nuclear speckles in cells in two datasets [52, 53] (**c**) GO of top enriched biological pathways of proteins depleted or enriched in SON IDR2-compartmentzlied condensates. (**d, e**) Representative images of droplet formation assay with increasing concentration of SON IDR2 with or without NE supplementation (**e**) and quantification (**e**) of the number, sphericity and total areas of droplets (n=6). (**f**) Representative images and quantification of spatial distribution of mCherry::SON IDR2 and GFP::SRSF2. (**g**) Representative images and quantification of spatial distribution of mCherry::SON IDR2, GFP::SRSF2 and mouse genomic DNA. Data: Mean ± S.E.M. Statistical tests used: unpaired one-tailed Student's t-test for e.

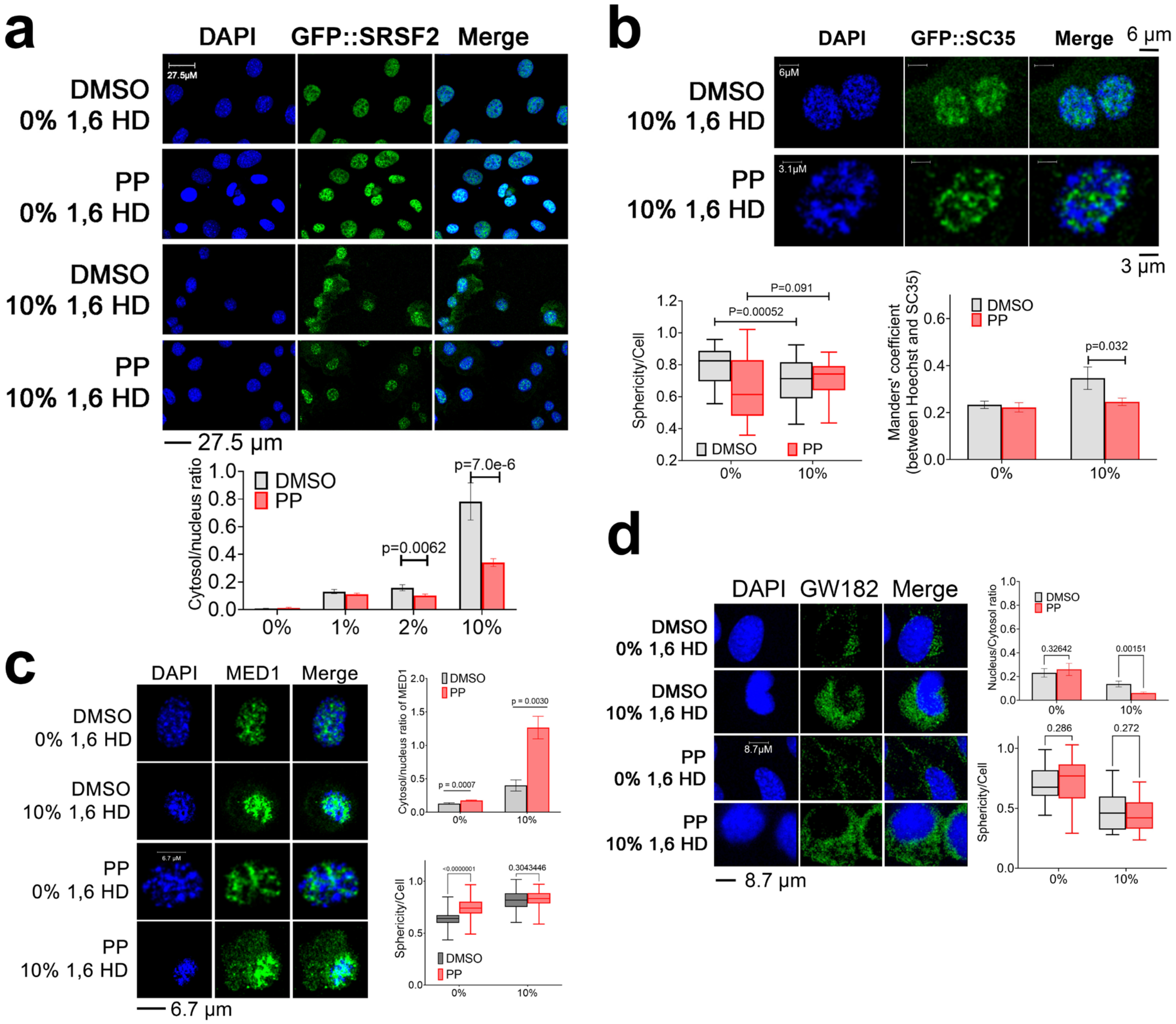

Supplementary Figure 16. PP alters the sensitivity of different condensates to 1,6 hexanediol. (**a**) 1,6 hexanediol sensitivity assay with representative images and quantification (n=20~95) of the ratio of cytosol over nuclear intensity of GFP::SRSF2 signal. (**b**) 1,6 hexanediol sensitivity assay with representative images and quantification of sphericity (n=24~50) of GFP::SRSF2 signal and Manders' coefficient (n=10~14) of signals of GFP and Hoechst. (**c**) 1,6 hexanediol sensitivity assay with representative images and quantification of ratio of cytosol to nuclear MED1 signal (n=19~29) and sphericity of MED1 signal (n=31~75). (**d**) 1,6 hexanediol sensitivity assay with representative images and quantification of ratio of cytosol to nuclear GW182 signal (n=16~54) and sphericity (n=19~97) of GW182 signal. Data: Mean ± S.E.M. Statistical tests used: unpaired one-tailed Student's t-test for all data.

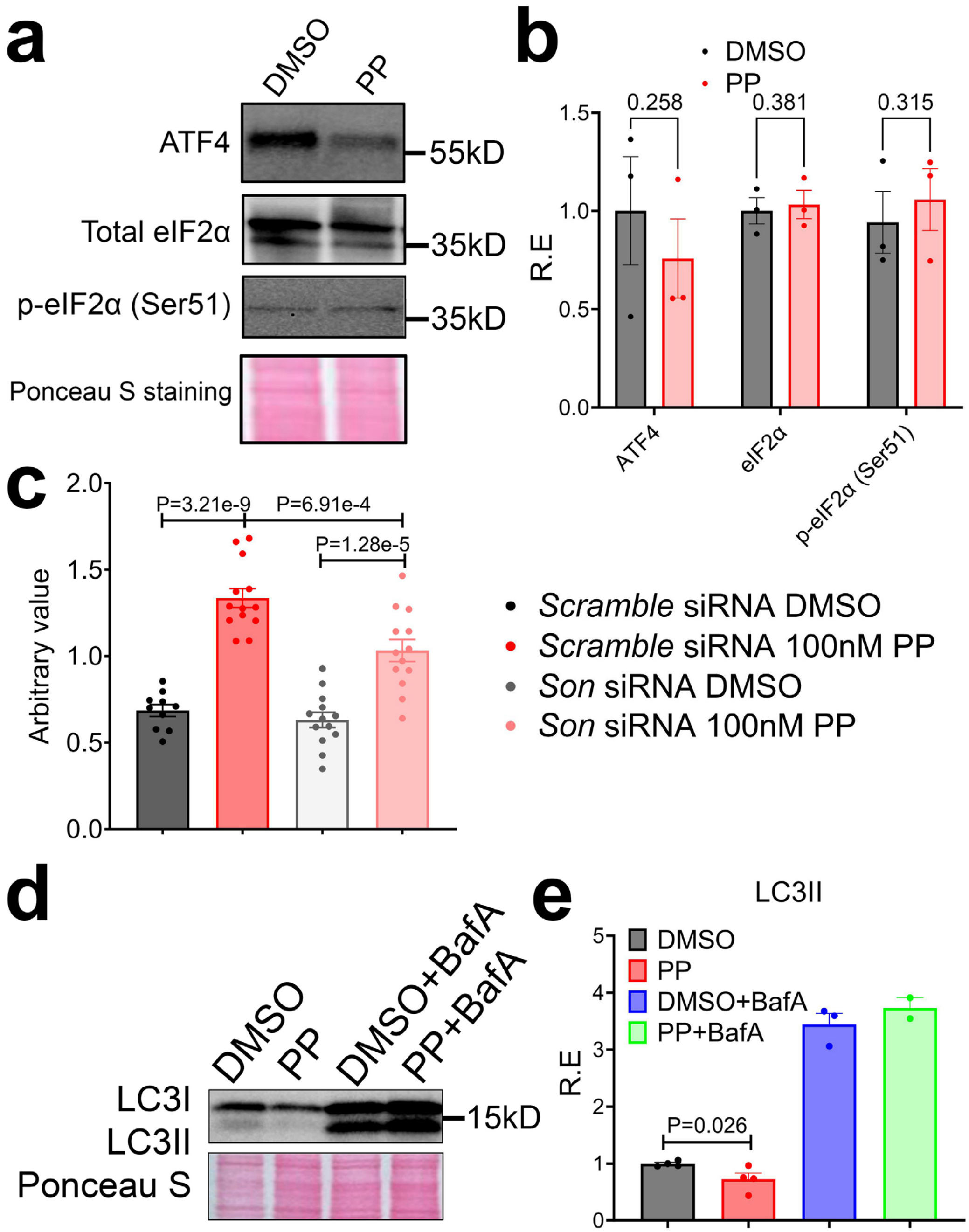

Supplementary Figure 17. Nanomolar concentration of PP promotes UPS and ALP without inducing cellular stress. (**a, b**) MEFs were treated with DMSO or 100nM PP for 24 hours. Representative western blot (**a**) and quantification (**b**) of different proteins (n=3). (**c**) MEFs were transiently transfected with scrambled or Son siRNA for 24 hours before treated with DMSO or 100nM PP for another 24 hours. 20S proteasome activity assay was then performed (n=10~13). (**d, e**) MEFs were treated with vehicle control or 1μM PP for ~22 hours and then co-treated with or without Baf A (100nM for 22 hours) (n=2~4). Representative western blot image (**d**) and quantification (**e**) of LC3II and LC3II/LC3I ratio. Data: Mean ± S.E.M. Statistical tests used: unpaired one-tailed Student's t-test for all data.

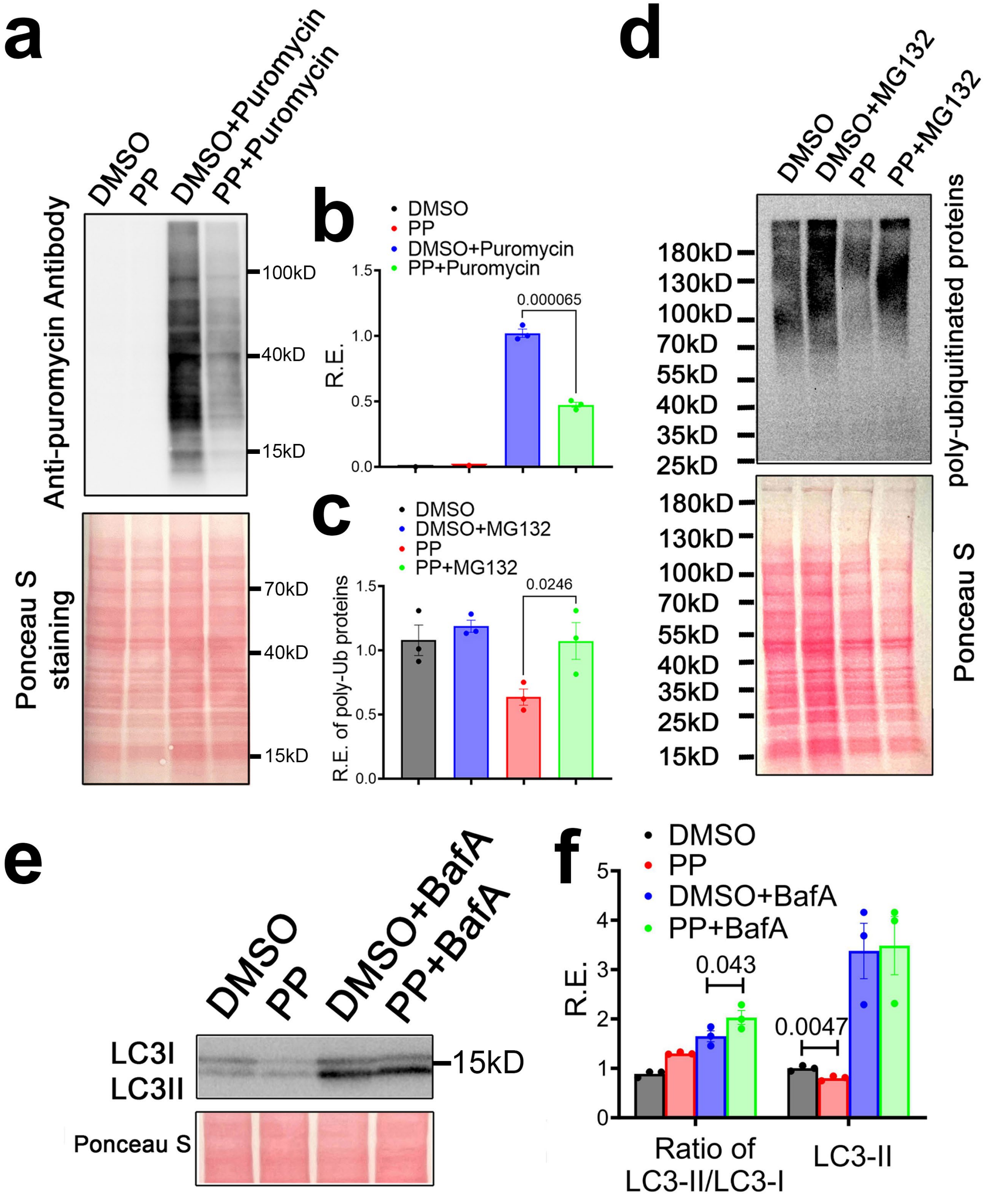

Supplementary Figure 18. Micromolar PP promotes autophagy and UPS activity and represses translation. MEFs were treated with vehicle control or 1µM PP for ~24 hours (22 hours for **e** and **f**) and then co-treated with or without puromycin (10 µg/mL for 30 minutes), MG132 (10µM for 110 minutes) or Baf A (100nM for 22 hours) (n=3 for all samples). Western blot and quantification of puromycin-incorporated proteins (**a, b**), poly-ubiquitinated protein (**c, d**) and LC3II and LC3II/LC3I ratio (**e, f**). Data: Mean ± S.E.M. Statistical tests used: unpaired one-tailed Student's t-test for all data.

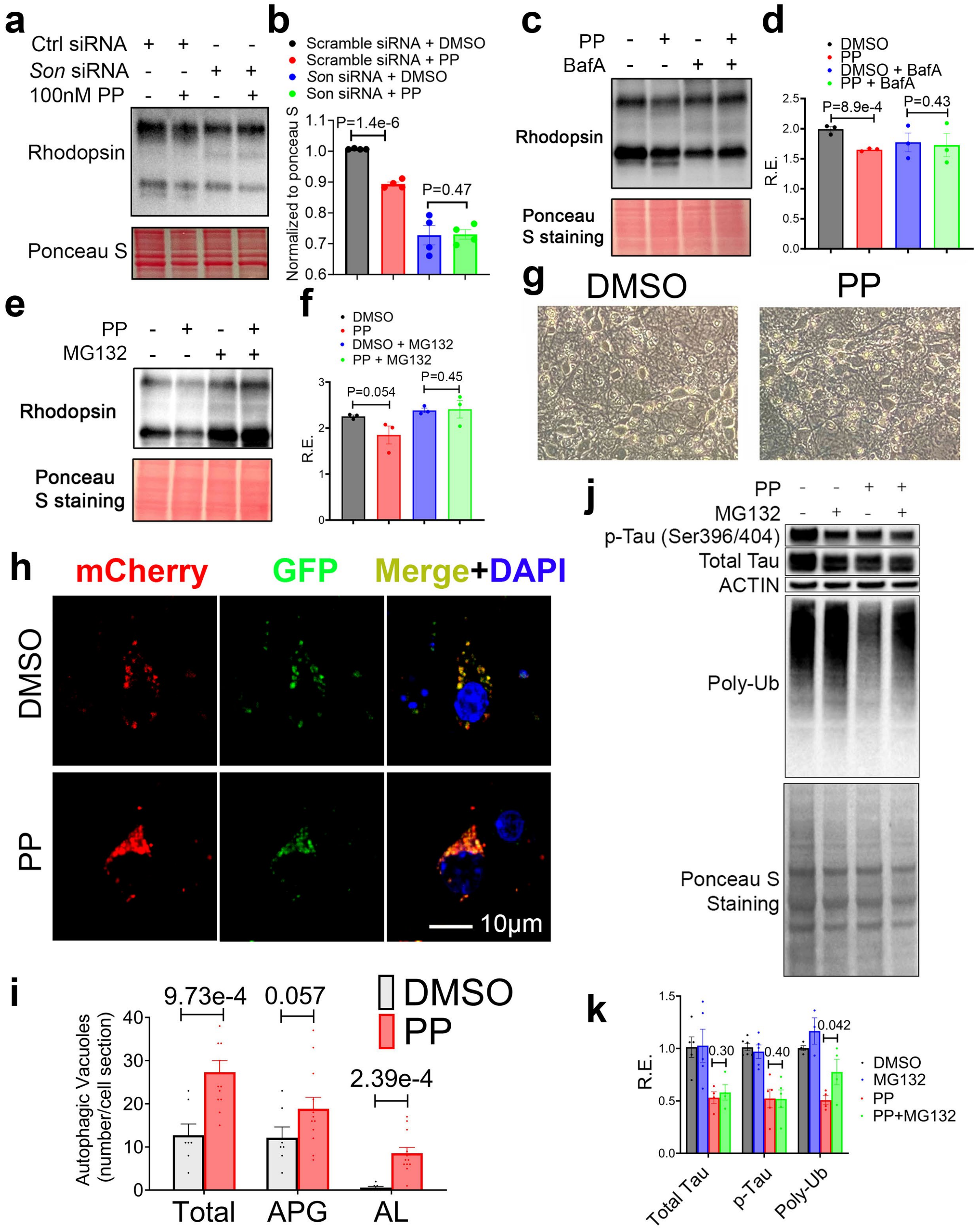

Supplementary Figure 19. Pyrvinium pamoate reduces pathological Tau and Rhodopsin level by boosting autophagy and UPS activity. (**a, b**) NIH3T3 RHO^{P23H} cells were transfected with scrambled or *Son* siRNA for 24 hours before treated with DMSO or 0.1μM PP for another 24 hours. Western blot (**a**) and quantification (**b**) of RHO^{P23H} level (n=4). (**c, d**) NIH3T3 RHO^{P23H} cells were treated with 0.1μM PP and co-treated with or without BafA (100nM) for 24 hours. Western blot (**c**) and quantification (**d**) of RHO^{P23H} level (n=3). (**e, f**) NIH3T3 RHO^{P23H} cells were co-treated with or without MG132 (10μM for 120 minutes). Western blot (**e**) and quantification (**f**) of RHO^{P23H} level (n=3). (**g**) Representative images of primary mouse neurons treated with DMSO or 0.5 μM PP for 24 hours. (**h, i**) Representative images showing an increase of the number of mCherry positive puncta in primary neurons cultured in the presence of 0.1μM PP for 12 hours, with zoomed in images of regions marked with white rectangles (**h**). Quantification of the number of total vacuoles, autophagosome and autolysosomes (n=7~12) (**i**). (**j, k**) Tau P301S-expressing primary neurons were co-treated with vehicle or 0.1μM PP in the presence or absence of MG132 (10μM) for 12 hours and western blot (**j**) and quantification (**k**) of different proteins (n=3~5). All data mean ± S.E.M. Statistical tests used: unpaired one-tailed Student's t-test for all data.

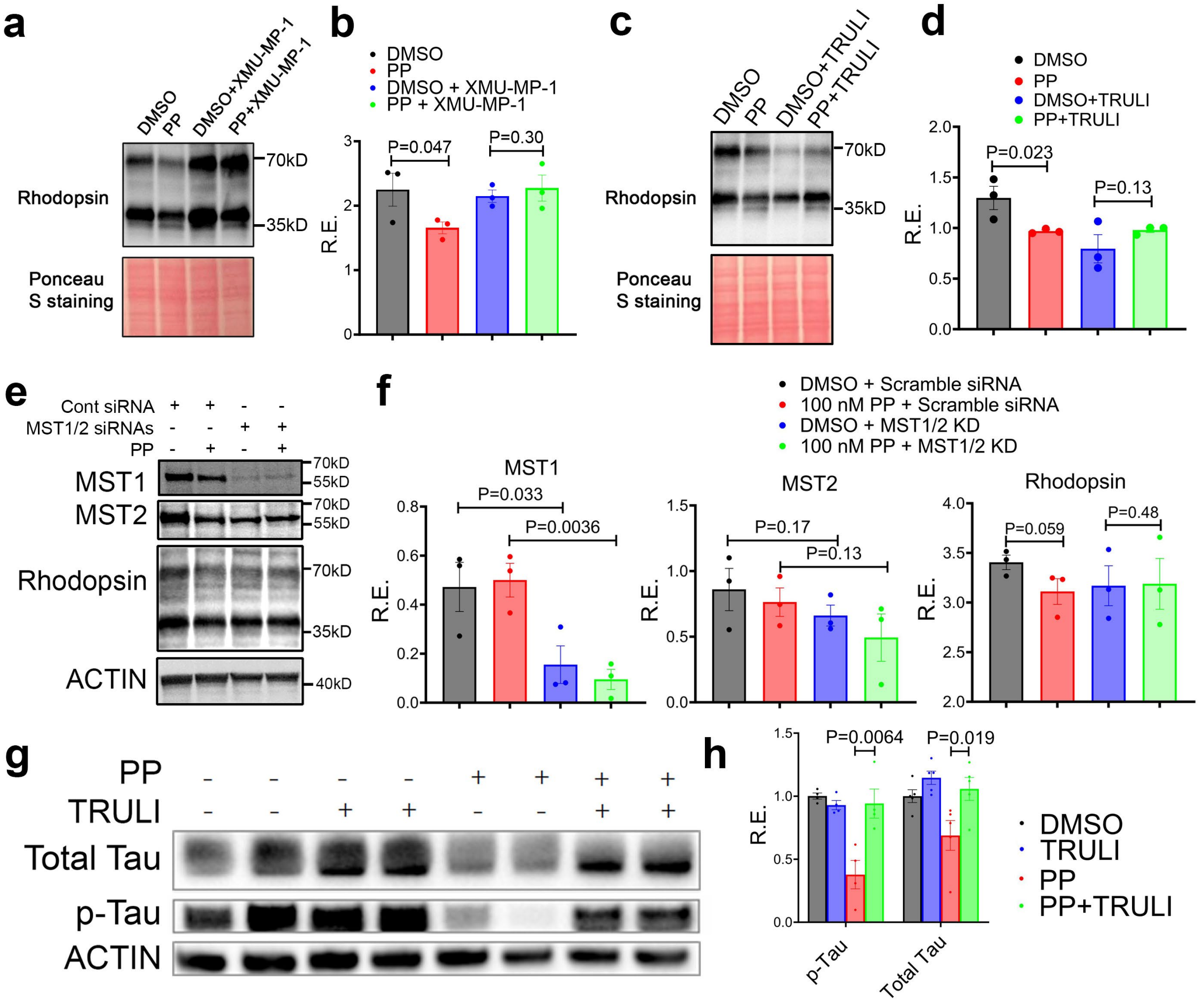

Supplementary Figure 20. Pyrvinium pamoate reduces pathological Rhodopsin level in a manner that depends on reduced YAP1 activity. (**a**, **b**) NIH3T3 RHO^{P23H} cells were treated with 0.1μM PP for 24 hours and co-treated with or without XMU-MP-1 (1μM). Western blot (**a**) and quantification (**b**) of RHO^{P23H} level (n=3). (**c, d**) NIH3T3 RHO^{P23H} cells were treated with 0.1μM PP for 24 hours and co-treated with or without TRULI (1μM). Western blot (**c**) and quantification (**d**) of RHO^{P23H} level (n=3). (**e, f**) NIH3T3 RHO^{P23H} cells were transiently transfected with scrambled or Mst1/Mst2 siRNAs for 24 hours and then treated with DMSO or 0.1μM PP for another 24 hours. Western blot (**e**) and quantification (**f**) of MST1/2 and RHO^{P23H} level (n=3). (**g, h**) Tau P301S-expressing primary neurons were co-treated with vehicle or 0.1μM PP in the presence or absence of YAP1 activator TRULI (10μM) for 12 hours and western blot (**g**) and quantification (**h**) of different proteins (n=4). All data: mean ± S.E.M. Statistical tests used: unpaired one-tailed Student's t-test for all data.

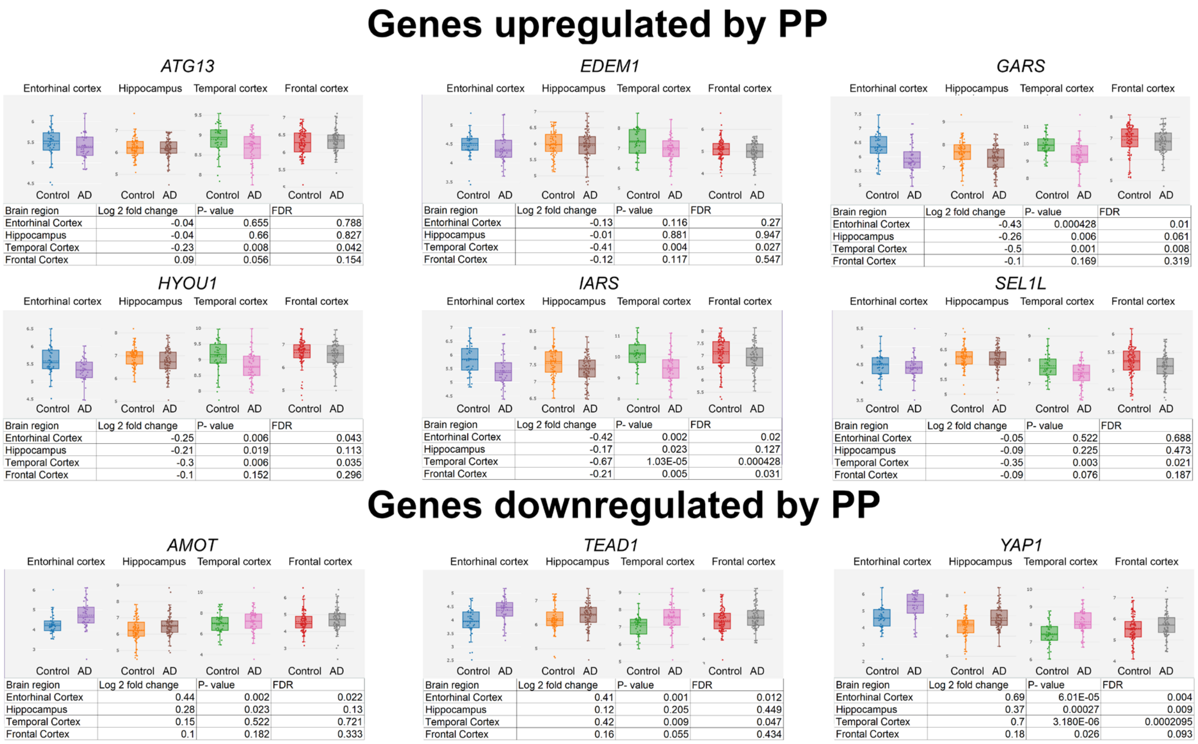

ATG13

Brain region	Log 2 fold change	P- value	FDR
Entorhinal Cortex	-0.04	0.655	0.788
Hippocampus	-0.04	0.66	0.827
Temporal Cortex	-0.23	0.008	0.042
Frontal Cortex	0.09	0.056	0.154

EDEM1

Brain region	Log 2 fold change	P- value	FDR
Entorhinal Cortex	-0.13	0.116	0.27
Hippocampus	-0.01	0.881	0.947
Temporal Cortex	-0.41	0.004	0.027
Frontal Cortex	-0.12	0.117	0.547

GARS

Brain region	Log 2 fold change	P- value	FDR
Entorhinal Cortex	-0.43	0.000428	0.01
Hippocampus	-0.26	0.006	0.061
Temporal Cortex	-0.5	0.001	0.008
Frontal Cortex	-0.1	0.169	0.319

HYOU1

Brain region	Log 2 fold change	P- value	FDR
Entorhinal Cortex	-0.25	0.006	0.043
Hippocampus	-0.21	0.019	0.113
Temporal Cortex	-0.3	0.006	0.035
Frontal Cortex	-0.1	0.152	0.296

IARS

Brain region	Log 2 fold change	P- value	FDR
Entorhinal Cortex	-0.42	0.002	0.02
Hippocampus	-0.17	0.023	0.127
Temporal Cortex	-0.67	1.03E-05	0.000428
Frontal Cortex	-0.21	0.005	0.031

SEL1L

Brain region	Log 2 fold change	P- value	FDR
Entorhinal Cortex	-0.05	0.522	0.688
Hippocampus	-0.09	0.225	0.473
Temporal Cortex	-0.35	0.003	0.021
Frontal Cortex	-0.09	0.076	0.187

AMOT

Brain region	Log 2 fold change	P- value	FDR
Entorhinal Cortex	0.44	0.002	0.022
Hippocampus	0.28	0.023	0.13
Temporal Cortex	0.15	0.522	0.721
Frontal Cortex	0.1	0.182	0.333

TEAD1

Brain region	Log 2 fold change	P- value	FDR
Entorhinal Cortex	0.41	0.001	0.012
Hippocampus	0.12	0.205	0.449
Temporal Cortex	0.42	0.009	0.047
Frontal Cortex	0.16	0.055	0.434

YAP1

Brain region	Log 2 fold change	P- value	FDR
Entorhinal Cortex	0.69	6.01E-05	0.004
Hippocampus	0.37	0.00027	0.009
Temporal Cortex	0.7	3.180E-06	0.0002095
Frontal Cortex	0.18	0.026	0.093

Supplementary Figure 21. Gene signatures in human AD subjects are opposite from those regulated by PP revealed by bulk RNA-Seq. Relative gene expressions in different brain regions of human AD subjects normalized to control subjects as reported in [87].

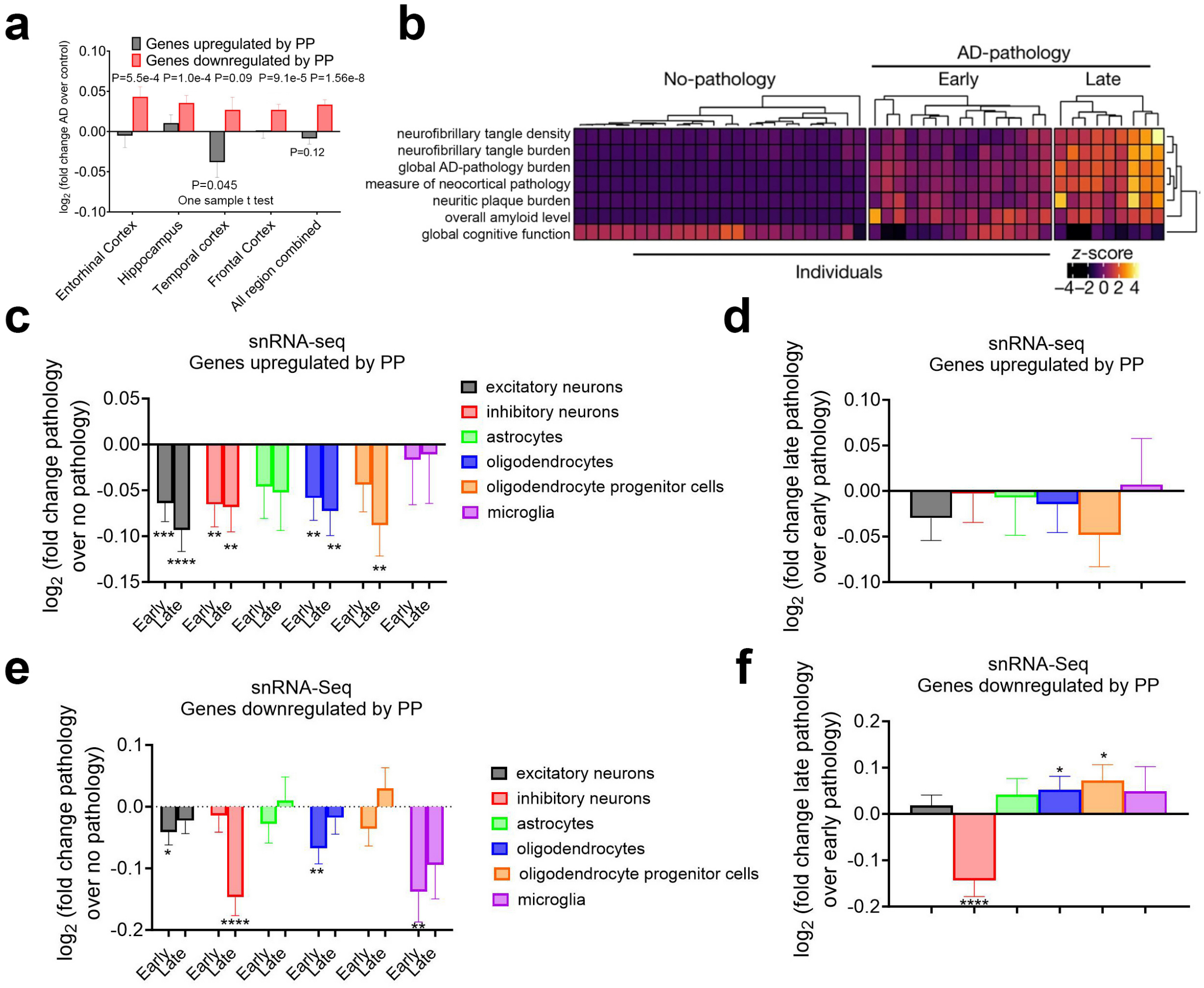

Supplementary Figure 22. Gene signatures in late-stage human AD subjects with severe tauopathy are opposite from those regulated by PP. (**a**) Log $_2$ transformed values of fold change of gene expression of different individual or combined brain regions of AD versus control human subjects for top genes that were either upregulated or downregulated by PP (with a $\log_2$ fold change > 1.5) in MEFs. (**b**) Phenotypic clustering of 48 individuals (columns) using seven clinicopathological variables as reported and adapted from [88]. (**c-f**) Log $_2$ transformed values of fold change of mean gene expression of different cell types of early or late AD versus no pathology human subjects for top genes that were either upregulated (**c**) or downregulated by PP in MEFs (**e**). Log 2 transformed values of fold change of mean gene expression of different cell types of late AD versus early AD human subjects for top genes that were either upregulated (**d**) or downregulated by PP in MEFs (**f**). Data: Mean ± S.E.M. Statistical tests used: unpaired one-tailed Student's t-test for a. One sample t-test (one-tailed). * p<0.05, ** p<0.01, *** p<0.001, **** p<0.0001 for c-f.

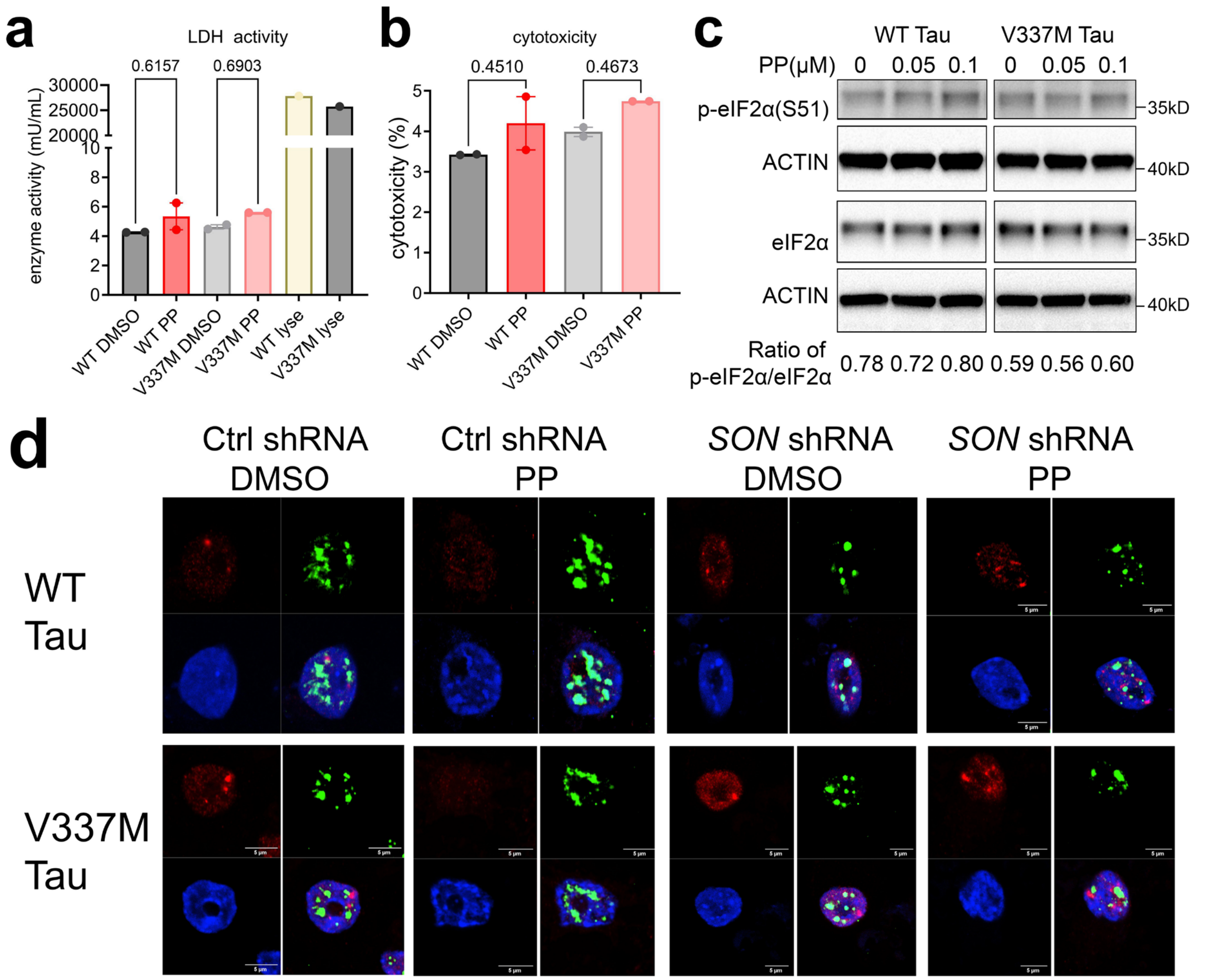

Supplementary Figure. 23. Nanomolar PP rejuvenates nuclear speckles and alleviates tau burden in human iPSC-neurons expressing mutant Tau in a SON-dependent manner without causing cellular stress. (**a-b**) WT and V337M Tau-expressing iPSC neurons were treated with 500 nM PP for 24 hours and LDH release assay were performed. LDH enzyme activity (**a**) and normalized cytotoxicity (**b**) were shown. (**c**) WT and V337M Tau-expressing iPSC neurons were treated with increasing concentration of PP for 12 hours and western blot of eIF2α and p-eIF2α were performed. The ratio of p-eIF2α to total eIF2α were calculated. (**d**) Wild-type and V337M Tau-expressing iPSC-neurons were infected with scrambled shRNA or SON shRNA-encoding lentivirus and treated with DMSO or PP (100nM) for 12 hours, and IF against nuclear speckle (Ab11826 against SRRM2), p-Tau (Ser422) and chromatin (DAPI) were performed.

Supplemental Movie legends:

Movie S1. Time lapse imaging of droplet formation with 20μm SON IDR1 in 125mM NaCl.

Movie S2. Time lapse imaging of droplet formation with 20μm SON IDR2 in 125mM NaCl.

Movie S3. Time lapse imaging of droplet formation with 20μm SRSF2 in 125mM NaCl.

Movie S4. Time lapse imaging of droplet formation with 10μm SON IDR2 supplemented with 0.6mg/ml GFP::SRSF2 MEF NE.

Supplemental Table legends:

Table S1. FPKM normalization of RNA-seq of SON OE and KD cells in the absence or presence of Tunicamycin in MEFs.

Table S2. TPM normalization of RNA-seq of different chemical treatments in MEFs.